From Structure to Function: Roles of System Level Excitation/Inhibition Balance on Spatio-Temporal Pattern Formation in Neuronal Networks

by

Jiaxing Wu

A dissertation submitted in partial fulfillment
of the requirements for the degree of
Doctor of Philosophy
(Applied Physics)
in The University of Michigan
2019

Doctoral Committee:

Professor Victoria Booth, Co-Chair
Professor Michal R. Zochowski, Co-Chair
Associate Professor Sara J. Aton
Professor Cagliyan Kurdak
Assistant Professor Qiong Yang

The most beautiful emotion we can experience is the mystical. It is the power of all true art and science.

- Albert Einstein

Figure 0.1: Figure from: 4 Psychology Degree Facts and Myths to Know Before Enrolling. November 1, 2018.

Jiaxing Wu

jxwu@umich.edu

ORCID id: 0000-0003-1966-4328

ACKNOWLEDGEMENTS

When I was an undergraduate student, I had heard about how challenging it is to fulfill a Ph.D. degree. After being conflicted for a while, I decided to apply for the Ph.D. program, which turned out to be one of the most correct and significant decisions I have made in my life. The last five years have been the most wonderful adventure of my life, where I have not only learned so much in both science and life, but now also know much more about who I truly am. The reason for all of these to happen is that I was so lucky to have many fantastic people around me.

First, I would like to thank my two advisors, Michal Zochowski and Victoria Booth, for making the challenging research a fun and fulfilling process, and teaching me how to be a thoughtful scientist and how to work with people. Even when the 1h weekly meetings often extended to 4h straight in one afternoon, you were always so patient to listen to my explanation of my results, discuss the details thoroughly, and never shut down my ideas. I learned to capture the big picture as well as cautiously understand the details in scientific research. Thank you Victoria for fixing tons of language problems in my writing and still not yelling at me. Thank you Michal for not declining me to join the lab, even after I tried to solve Hodgkin-Huxley equation analytically at the very beginning, so that I had the chance to start my research life in this super fun research field, using physics to study the brain. I have never thought I could joke around with my advisor like a friend, which is part of the highlight of my Ph.D. life. In addition, thank you both for giving me full freedom to choose my career path and satisfy my curiosity of working in industry.

Also, I would like to thank professor Sara Aton, with whom I have worked closely during my first two years, for doing so many awesome experiments and giving me the chance to actually see the process where a memory is formed in a real brain by looking at my analysis results. I still remember how excited I felt the first time you helped me to understand this process. And you are always encouraging and considerate, really pleasant to work with. To the other two committee members, professor Cagliyan Kurdak and Qiong Yang, thanks for being my committee and spending time to advise me.

I am super grateful to the Applied Physics Program for giving me the great offer to have me here, and providing me with so much mental and financial support. Thank you Dr. Cagliyan Kurdak, Cynthia McNabb, Keith Arthur, Lauren Segall, who are always smiling and have put lots of efforts to make the program feel like a warm family. Especially during my first year when I was so confused about the US and graduate school, I talked with Dr. Kurdak many times about choosing the lab and finally figured out my research interest. Also many thanks to professor Duncan Steel and Bing Zhou for all your advice for making decisions on my career path.

Also thanks a lot to my lab mates Dan Maruyama, James Roach, Quinton Skilling, Maral Budak, Bola Eniwaye, Yihao Yang, Daniel McCusker, and Jack Lin, who have made the lab a super friendly, relaxing and pleasant work environment. To the three of them who had the longest overlap with my time, James, Quinton and Maral, thanks for so much fun time during the conferences all over the world and great conversations on confusion and reflection about research.

I would have never made it without all the sweet, nice, and supportive friends I have known from various groups. To friends from Applied Physics, Physics, as well as other Ph.D. programs, Sunan Cui, Jia Guo, Lise Wei, Ketian Yu, Chengyu Dai, Jiachen Huang, Zhen Xu, Lu Chen, Trevor Bailey, Qiaoyuan Dong, Xiao Zhang, Wenbo Shen, Ruikun Luo, Changjiang Liu, Hongyang Zhou, Joyce Lee, thank you

for experiencing this fun Ph.D. adventure together with me and discussing so many questions in depth. To friends from Thus Spoke Ann Arbor drama club, Xuecong Xu, Xinglin Wang, Fangwei Zhao, Xiaoqi Hu, Qinni Jiang, Tianshi Xie, Yate Ji, Jiongsheng Cai, Yuwen Zhang, I feel so lucky to know all of you, who are always energetic, thoughtful, and genuine. Thanks for bringing so much fun and beautiful experience with art in my life. The friends that also came from the University of Science and Technology of China (USTC), Yuan Yang, Yao Zhao, Zhilin Yue, Rong Xu, Hongze Cheng, Jinqi Shen, Zhengyu Zhang, Wen Guo, Tonghui Ming, Yina Geng, Zida Li, I cannot express more thankfulness for always being there and supportive whenever I was in difficult situations, like my brothers and sisters. And thanks to the friends that I know from the trips, parties, and activities, Yun Liu, Ya Cai, Yingyi Song, Bingjie Li, Wei Guo, Shengtao Wang, Tianpei Xie, Jiahua Gu, you have made my Ph.D. life much more diverse and left me lots of precious memories through beautiful photos, fun dancing, creative cooking, badminton etc. And thank you to many more dear friends that I did not list here. Mr. Matthew Dempsey, I don't know how to express how lucky I feel when thinking about the trajectory of our lives crossing during my last year of Ph.D. Thank you so much for listening to all my stress and concerns so patiently and making me happy whenever I'm upset. Thanks for always being peaceful, calm, kind and supportive.

Finally, to my parents, who are the most significant people in my life and love me the most, I don't know where I would be without you. Being apart on opposite sides of the earth is definitely super hard for you, you have never expressed any negative feelings in front of me, but have always supported me to pursue my dreams. Thanks a million for providing the warmest and safest place in the world for me. I love you, Mom and Dad!

In all, I can't express enough gratitude to all these brilliant people. You guys are the best! Thanks for not only helping me know better who I am over past five years,

but also helping me to create a better version of myself.

TABLE OF CONTENTS

LIST OF FIGURES

ABSTRACT

The brain consists of complex interacting networks of excitatory and inhibitory neurons. The spatio-temporal dynamical patterns in these neural networks are believed to underlie all cognitive functions such as perception, memory formation etc. Therefore, insights into the mechanisms of the generation of various network level spatio-temporal dynamics in the context of underlying structural and functional connectivity is essential for understanding how the brain works. These mechanisms themselves depend on global variables characterizing network state, such as relative levels of excitation and inhibition. Here, I combine computational modeling and statistical analysis to investigate changes in neuronal activity patterns and identify the network and cellular mechanisms responsible for those dynamical patterns as a function of changing excitatory/inhibitory (E/I) levels. First, I extend a statistical metric developed in our laboratory, referred to as average minimal distance (AMD), to rapidly quantify the functional connectivity in the network. The metric is able to capture both co-occurrence and causality relationships, providing a more significant correlation value than traditional methods in a much more efficient manner. Combined with a measure of functional network stability (FuNS) which reliably captures the global stability of the functional patterns, I use this AMD-FuNS framework to analyze large-scale *in vivo* datasets during memory consolidation over extended time periods. Next, I turn to investigate the universal mechanisms underlying emergence of various functional connectivity patterns as E/I levels are varied in networks com-

posed of excitatory and inhibitory neural populations. I identify multiple E/I balance regimes where E/I balance is similar but network dynamics are heterogeneous. Each balance regime is regulated by the competing interactions between population firing rate and evolving magnitude of postsynaptic potentials at different synaptic coupling levels. I investigate these patterns E/for networks composed of neurons having different membrane excitability types and find that emerging dynamics and their underlying mechanisms depend critically on neuronal excitability types and network connectivity regimes. Taken together, the theoretical framework presented here provides a mechanistic understanding for the emergence of functional dynamical patterns due to the properties of E/I balance in neural network.

CHAPTER I

Introduction

The brain controls all of our behaviours and mental processes in daily life, including motion, learning, and emotional states. As the most sophisticated organ in our body, its mechanism of carrying out complicated computations and forming cognition still remains an open question. Over decades of active studies, brain research has become more and more interdisciplinary across psychology, physiology, biology, mathematics, physics, and also computer science. Each field studies the brain from different perspectives, and different temporal and spatial scales depending on the specific techniques. On one hand, significant work has given a clear description of the properties and mechanisms of each individual nerve unit, i.e. neuron. On the other hand, experiments at a much larger scale involving hundreds of thousands of neurons shed light on the functions of each brain region. Additionally, some neuronal pathways of information flow have been identified with the help of clinical observations and advances in imaging techniques such as functional Magnetic Resonance Imaging (fMRI). However, despite the abundant knowledge on each unit and large scale neuronal regions, an important part remains unclear: How does a network of interconnected neurons generate consciousness, or intelligence? Given that each neuron itself is not conscious and works generally in a similar way, this question boils down to how a neural circuit at the scale of hundreds or thousands of neurons generates

cognitive functions through the way neurons interact. This work is aimed to give insights on the mechanism of complex dynamics in neural circuits.

1.1 Neurons - the computing units of the nervous system

Neurons are the signaling units in nervous systems. The human brain is composed of about a hundred billion neurons, each of which is connected with thousands of other neurons. The ability of neurons to communicate with each other at a precise time scale is mainly due to two important features: 1) The asymmetric anatomy of neurons guarantees the signal propagates in a unidirectional fashion from the dendrites to the axon; 2) Electrical signals are transmitted via the changes of membrane potentials when neurons are excited electrically or chemically. More than 100 types of neurons have been identified containing different types of proteins, membrane constituents, etc. However, neurons share a lot of common structural features and the mechanism for producing signals within and between cells.

Although there are many different types of neurons, they typically receive signals from several short dendrites, which branch out towards other nerve cells, and integrate the signals in the metabolic center called the soma. The neuron's output signal is then transmitted on a single axon with a length ranging from 0.1mm to 2m, and arrives at the presynaptic terminals, where the signal is sent to the downstream neurons.

1.1.1 Generation of action potentials

Neurons communicate via action potentials. Action potentials are generated by the intricate electrochemical balance across neuron's membranes. Namely, neuron cells maintain the unequal electrical potentials on the two sides of the plasma membrane by regulating the concentration of charged ions, mainly Na^+ and K^+. When the cell is at rest, the concentration of Na^+ stays low and the concentration of K^+ stays high inside the cells by the Na^+-K^+ pumps. The resting membrane potential is

kept around -65mV. Membrane potentials are mediated by the ion channels, a class of proteins in the cell membranes. Ion channels are selective to the type of ions, allowing only specific ion types to permeate when open. In this way, the signals are able to be regulated by activating different ion channels. Another important property is that the opening and closing of ion channels are gated by the membrane potential. A temporal change in membrane potential causes the sequential opening of different ion channels, thus introducing the flux of charged ions across the cell membrane which further changes the voltage across the membrane. Increase and decrease in membrane potential is referred to as depolarization and hyperpolarization, respectively. In the 1950s, Alan Hodgkin and Andrew Huxley quantified the gating mechanisms of ion channels during the action potentials using voltage clamp experiments, where the membrane voltage can be maintained constant. When the membrane potential increases to a threshold where Na^+ channels rapidly activate, a large positive inward current causes an accelerated depolarization in membrane potential, due to Na^+ ions flowing into the cell, which is called action potential. The depolarization is followed by the inactivation of Na^+ channels and the activation of K^+ channels, which repolarize the membrane potential by inducing an outward current, caused by K^+ ions flowing out of the cell. Once an action potential is generated, it can be conducted without attenuation along the axon and propagated to other neurons. An action potential is also called a "spike", and when generating an action potential, the neuron is said to "fire".

The capacitance and resistance properties of the membrane can be abstracted to an equivalent electrical circuit Figure 1.2. The opening and closing of the ion channels are simulated by the change in conductance of the corresponding ion type. The concentration gradient of each ion type gives rise to a chemical driving force, represented as a battery in each branch. This equivalent circuit provides an intuitive interpretation of the computation for each current component separately.

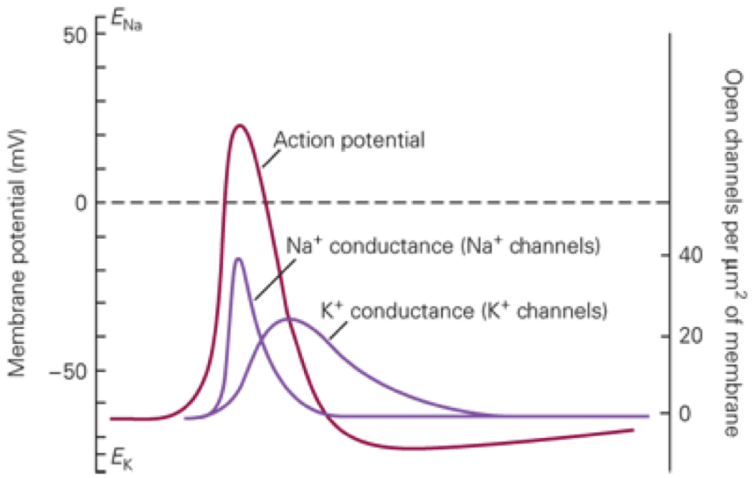

Figure 1.1: The sequential opening of voltage-gated Na+ and K+ channels generates the action potential. The shape of the action potential and the underlying conductance changes can be calculated from the properties of the voltage-gated Na+ and K+ channels. Figure from (*Kandel et al.*, 2012).

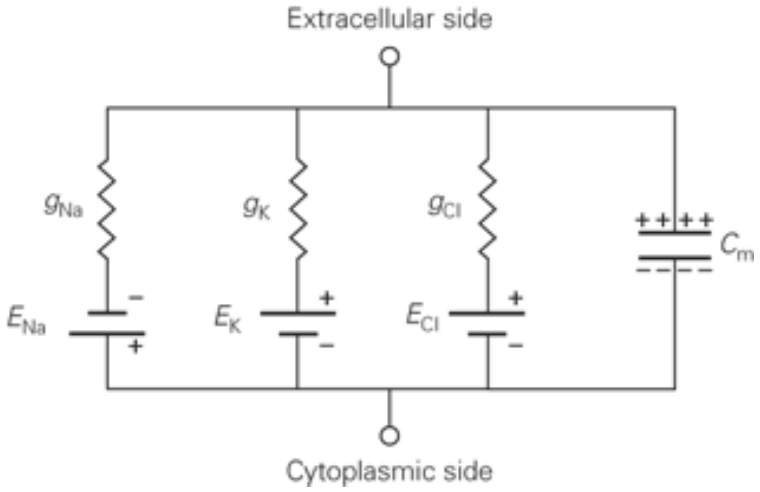

Figure 1.2: The equivalent circuit of the membrane. Figure from (*Kandel et al.*, 2012).

1.1.2 Synaptic transmission

Neurons communicate with each other through synapses. When an action potential arrives at the axon terminals of a presynaptic neuron, chemical substances are released, or electrical signals are sent in some cases, onto the dendrites of the postsynaptic neurons. The axon of the presynaptic neuron splits into branches, each of which forms multiple expansions called synaptic boutons. The chemical substances, neurotransmitters, are released from synaptic boutons and open up the receptor channels on the postsynaptic membrane. The postsynaptic membrane gets depolarized and an excitatory postsynaptic potential (EPSP) is generated. Postsynaptic potential (PSP) can vary significantly in magnitude. A single PSP generated from a motor neuron to a muscle fiber can reach about 70mV, which is often large enough to trigger an action potential. However, one single EPSP is only about 1mV in the central nervous system. Therefore, generating an action potential usually requires the integration of multiple synaptic stimuli. The EPSP is produced by an inward current when the receptor channels are open. This postsynaptic current can be calculated as

$$I_{EPSP} = g_{EPSP} \times (V_m - E_{EPSP}), \tag{1.1}$$

where $\mathrm{E_{EPSP}}$ is the *reversal potential* which acts as the chemical battery due to the concentration gradients and drives the ions through the receptor channels, and g_{EPSP} is the conductance of the receptor channels. With the membrane getting more depolarized, the driving force becomes smaller, resulting in a smaller inward postsynaptic current (PSC). When V_m is equal to the reversal potential, net current flowing through the membrane is zero. When V_m is more positive than the reversal potential, the direction of the current reverses and an outward current hyperpolarizes the membrane. This is for excitatory synaptic currents through AMPA and NMDA receptors. Different from the voltage-gated channels, the receptor channels are not selective for ion

types due to the significantly larger diameter of the pores, and Na^+ and K^+ share the common channels. Therefore, the permeability of Na^+ and K^+ through receptor channels are roughly equal. At E_{EPSP}, the influx of Na^+ cancels out the efflux of K^+, resulting in that E_{EPSP} is around 0mV, as measured in voltage-clamp experiments.

Another important difference between the synapses in the central nervous system and the synapses between motor neurons and muscle fibers is that the synaptic signals can be either *excitatory* or *inhibitory*. The excitatory synapses are similar for both cases and depolarize the postsynaptic membrane, while the inhibitory synapses hyperpolarize the postsynaptic neuron instead, making it harder to fire an action potential. Also, the neurotransmitters released onto the neurons in central nervous system are much more diverse, which alter the activities of the target neurons in various ways. The effect of excitatory or inhibitory PSP depends on the activation of the channels on postsynaptic membrane by the neurotransmitters, where most neurotransmitters produce a single type of signal, either excitatory or inhibitory. The major excitatory neurotransmitter in the brain is the amino acid I-glutamate, and the glutamate-gated receptor channels permeate Na^+ and K^+ when open. Some major glutamate receptors include AMPA, kainate, and NMDA. One major type of inhibitory amino acid neurotransmitter, GABA, functions on either $GABA_A$ receptor, which is a channel for Cl^- ions, or $GABA_B$ receptor, which opens K^+ channels, thus generating an outward hyperpolarizing current. This current can have a shunting or subtractive effect on depolarizing synaptic current. Inhibitory synapses are critical to avoid excessive excitation and coordinate the excitatory neural activity. The majority population of the cerebral cortex is glutamatergic excitatory neurons, which are connected locally in a reciprocal way as well as to other distant brain areas such as the thalamus (*Somogyi et al.*, 1998). The recurrent excitatory connections can easily cause an explosive runaway activity. GABAergic inhibitory neurons, although they only make up approximately 20% of the population, provide a negative feedback and mediate

the stability of the network dynamics (*Sugino et al.*, 2005).

In central nervous system, the net effect of the diverse inputs from hundreds or thousands of presynaptic neurons are coordinated and integrated. The decision on firing an action potential or not is made at the trigger zone, which is located at the initial segment of the axon. This process is called neuronal integration. Whether an action potential will be generated is affected by multiple temporal and spatial factors.

1.2 Neural network and cell assembly

1.2.1 From cellular level to circuit level

The knowledge of the computing mechanisms of individual neurons and synapses has greatly promoted the understanding of the brain at cellular levels. However, it is not sufficient to explain how a collection of neurons generates a neural function together, or how the activities of multiple neuron sets are integrated for complex cognitive processing, such as a perception that combines visual, auditory, olfactory systems all together. An influential idea of "cell assembly", proposed by Donald Hebb (*Hebb*, 1949), argued that the neurons are wired together and act as a functional group in the nervous system, and that the synaptic connections can be shaped by the neural activity tailored for a specific cognitive process, which is known as synaptic plasticity. What are the advantages of network computation in the brain dynamics? An important characteristic is its robustness under anatomical damage. For example, an IQ of 160 was registered by a person after the removal of prefrontal lobe (*Hebb*, 1939). This may be explained by the assemblies distributing over a wide region over the brain and allowing the recruitment of new cells, thus maintaining the dynamics without requiring the exactly the same physical structure. The theory was also confirmed by other experiments involving the interaction between the environment and brain activity by manipulating the environmental or sensory stimulation. One experiment

showed that rats exposed to a rich perceptual environment were more intelligent after a period of time than those with a plain environment (*Milner*, 1993; *Rabinovitch and Rosvold*, 1951). The same results were obtained on Scottish terriers (*Thompson and Heron*, 1954). Additionally, as indicated by another experiment, human subjects had a harder and harder time solving problems or maintaining coherent thoughts after experiencing perceptual isolation for a long time (*Heron*, 1957; *Milner*, 1993).

By focusing less on the specific cellular properties of neurons, and more on the emergent properties from the interactions between the units of the network, neural network researchers apply some simplifications on the complex biological properties of real neurons and synapses in mathematical models. Dated back in 1943, the simplest neuron model was proposed by Warren McCulloch and Walter Pitts, where each neuron takes multiple inputs, computes conjunction or disjunction, and has binary output, with 1 representing "active" and 0 representing "inactive" state (*McCulloch and Pitts*, 1943). The different values of synaptic strengths are better modeled in the linear-threshold (LT) neuron proposed later by taking the weighted sum of the inputs from connected neurons (*Scholl*, 1956; *Hopfield*, 1982). An important advance was made by Frank Rosenblatt in the 1950s to model the visual perception, where the information flows in one direction, and the weights between each unit, called "perceptron", are revised during the learning process (*Rosenblatt*, 1958), which simulated synaptic plasticity. This "feed-forward" model provided basis to understand the brain through networks that are relatively easier to analyze (*Scott*, 2002). It also aroused great interest in the engineering field and is widely applied in artificial intelligence research and applications nowadays such as computer vision, natural language processing etc., about 60 years after it was first proposed.

However, the power of the feed-forward networks to help with our understanding of brain dynamics is limited due to its simpler dynamics than the real brain networks, which do contain a vast number of synaptic loops (*Kandel et al.*, 2012). In 1938, Rafael

Lorente de No postulated that the synaptic loops are the basic circuits of the nervous system, and are responsible for generating and maintaining the persistent neural activity over a long period of time, rather than a "stimulus-response" relationship (*Lorente De No*, 1938), while the feed-forward networks normally display the latter. Associative memory networks are the major model class that contain loops, composed of a group of synaptically-connected excitatory and/or inhibitory neurons. Central to the cell assembly theory, short term or long term memories are formed in the process of the interactions between neural activity and synaptic strengths, and the networks are able to maintain persistent activity patterns over an extended time period, even though the initial stimulation disappears. Instead of layered structure as in the feed forward networks, brain networks are considered as a large web-like network (*Varela et al.*, 2001). The network takes form of adjacency matrix composed of synaptic strengths between each neuron pair, where each neuron is modeled in a non-linear way (*Anderson*, 1988). This combination of network theory and non-linear dynamics is also the method adopted in the work shown in the following chapters.

1.2.2 Structural connectivity in neural networks

How are neurons connected in the brain? As mentioned above, neural networks in the brain display complicated structures like a web containing many recurrent loops, rather than a simple layered structure. Over the past decade, researchers have actively explored the realistic anatomical description of various brain regions as well as the role of the network topology in the computational abilities of the network (*Boccaletti et al.*, 2006). The detection of the complete anatomical structure is challenging due to a couple of reasons. One direct drawback is that synaptic plasticity results in the structural connectivity changing over time, thus making the notion of "connectivity" controversial (*Destexhe and Marder*, 2004). In addition, it has been found that different tracing techniques to detect anatomical connections in experiments may report

connectivity densities that differ by two orders of magnitude for the same connection (*Scannell et al.*, 2000), making it even more complicated. Moreover, research has been largely constrained by the limited size of the available databases (*Boccaletti et al.*, 2006). Even if a technique to detect the structural connections reliably is available, there are about 10^{15} synapses in the human brain, which would be impossible to fully identify.

Despite the difficulties, significant progress on determining connectivity at various spatial scales has been made. A full connectivity map of a much simpler and more compact neural system in C. elegans was identified, which only comprises a complement of 302 neurons (*White et al.*, 1986). The connectional organizations at the scale of large networks in some segregated brain regions of some mammalian species, such as the hippocampus (*Burns and Young*, 2000), the cerebral cortex (*Stephan et al.*, 2001), the cortical-cortical system (*Felleman and Essen*, 1991) and the cortical-thalamic system (*Scannell*, 1999), were analyzed and some corresponding prototype networks have been provided (*Stephan et al.*, 2001; *Bota et al.*, 2003). At a smaller level, more detailed anatomical structures were analyzed in cortical areas. The hierarchical structure analysis in primate visual cortices shed light on the directional patterns of the connections in the cortical layers, i.e. connections in ascending, descending or lateral directions (*Felleman and Essen*, 1991). Furthermore, the correlations or similarities between the local connectivity patterns of different cortical areas were also computed (*Kötter and Stephan*, 2003). However, the exact structure or topology in these regions still remains unknown.

Taking advantage of network theory, some theoretical work has provided better knowledge on the quantitative characteristics of brain networks. Some evidence shows that the brain is composed of some globally-interconnected neural clusters, each of which forms a dense and recurrent local circuit (*Varela et al.*, 2001). Results from other experiments identified feed forward loops or bi-parallel patterns in some of the

local connections (*Sporns and Kötter*, 2004). The connectivity patterns of neurons in the same cluster demonstrate higher similarity than those from different clusters (*Shepard*, 1980). One plausible mechanism of the inter-area cortical connectivity was proposed to relate the connection strength between the brain areas with the number of common neighbors they share (*Young*, 1992). Furthermore, the connectivity patterns of various cortical areas were suggested to be unique and referred to as the "connectional fingerprint" of the area (*Passingham et al.*, 2002). These characteristics of the brain organization were thought to follow rules that optimize the communication efficiency as well as minimize the cost of the interconnections (*Cherniak et al.*, 2004; *Chklovskii and Koulakov*, 2004).

1.2.3 Computational network models

The random network and the small-world network are two major types of network topology, which are widely used in computational modeling and capture the characteristics of the structural complexity in actual brain networks. Random networks, first proposed by Erdös and Rényi, are straightforward and the most well studied graph model. One of the simplest ways to generate a random network is that the number of nodes N and the connectivity probability p (or the total number of edges m) are given, and each possible directional edge between pairs of nodes is added with probability p. This model is often used to simulate relatively small local circuits, with the connection density controlled by p. A small-world network is characterized by a small value of average shortest path length L and a large value of clustering coefficient C (*Watts and Strogatz*, 1998). These characteristics contribute to efficient information communication and have been observed in many biological systems, as well as social and technological networks (*Watts*, 2003; *Newman*, 2001a,b). The average shortest path length L is calculated as the mean value of the shortest path length between all the node pairs, thus quantifying the typical separation distance between

two nodes in the network (*Boccaletti et al.*, 2006). The clustering coefficient C takes a value between 0 and 1, with 1 indicating that the nodes connecting to a common node also connect with each other and 0 indicating no closed loops composed of 3 nodes (*Newman*, 2010). Small-world networks can be generated by the Watts and Strogatz (WS) algorithm, where nodes are only connected to their nearest neighbors at first and then each edge is rewired at some probability, called the *rewiring parameter* (*Watts and Strogatz*, 1998).

1.3 Network dynamics and activity patterns

1.3.1 Functional connectivity

Action potential firing of neurons across a neural network generates complex spatio-temporal activity patterns. We often quantify these patterns in term of *functional connectivity*. Different from the anatomical connectivity of neural networks, functional connectivity measures the temporal correlation between neuronal activities and identifies the functional interactions between neurons or neuronal assemblies (*Aertsen et al.*, 1989; *Friston et al.*, 1993). At the circuit level, functional connectivity is traditionally calculated by the statistical correlation or causality relationship between the activity trains of the neuron pairs. While at the macroscopic level, the functional relationship between different brain regions during some specific cognitive tasks are analyzed based on electrophysiological recordings from electroencephalographic (EEG), magnetoencephalographic (MEG) or imaging techniques such as fMRI, which usually reflect the collective activity of the neuronal populations (*Boccaletti et al.*, 2006). Functional connectivity was proposed to act as a basic mechanism in the large-scale integration problem, where distributed neuronal populations are integrated in a unified functional process at different spatial and temporal scales. (*Schnitzler and Gross*, 2005).

Structural connectivity and functional connectivity are closely related, however, their exact relationship is still not fully understood.(*Petersen and Sporns*, 2015). Some evidence showed that the specific structural organization patterns in vision reflect a functional role (*Jouve*, 1998). Also, the hierarchical organization of the anatomical connectivity supports both the local neuronal functions and the global integration (*Park and Friston*, 2013). Functional connectivity has also been widely used recently to infer underlying anatomical structure (*Zaytsev et al.*, 2015; *Cestnik and Rosenblum*, 2017; *Poli et al.*, 2016). On the other hand, analysis on experimental results from MRI recordings indicated that two brain regions that are clearly linked by white fiber tracts demonstrate high functional connectivity, but this does not hold inversely, indicating that the brain regions connected functionally may be mediated by distant grey matter regions instead of being physically connected with each other (*Koch et al.*, 2002). Although the accurate relationship between the two types of connectivity remains unknown, the convergence of studies on the two connectivity patterns are promising to benefit understanding of the cognitive mechanism (*Sporns et al.*, 2004; *Petersen and Sporns*, 2015).

Lots of work using network theory to identify the patterns in functional connectivity has also been done. Some patterns demonstrated small-world characteristics from MEG recordings on healthy subjects (*Stam*, 2004), while others report scale-free properties based on fMRI data (*Eguíluz et al.*, 2005). In addition, a rich-club organization was discovered in large-scale human brain data (*Senden et al.*, 2014), which has been proposed to facilitate the long-term memory by allowing for an increasing number of unique activity patterns (*Nigam et al.*, 2016). However, research on functional connectivity shares some common challenges with anatomical connectivity, such as the limitation of the few datasets available, the effect from the resolution of the experimental setup, and the fluctuation of the connections over time (*Boccaletti et al.*, 2006). The major drawback is that the quantification of functional connectiv-

ity highly depends on the specific statistical methods used. Over the past decades, a number of statistical metrics have been discussed and compared extensively (*Bastos and Schoffelen*, 2016; *De Vico Fallani et al.*, 2014). Multiple distinct methods were summarized (*Wang et al.*, 2014). These methods can be first classified into two divisions: non-directed, where only co-occurrence and correlation of the activity events are measured, and directed, where the causal relationship is estimated based on the timestamps of the events (*Bastos and Schoffelen*, 2016). Methods in each division can be further differentiated depending on whether they are model-based or not. Moreover, some of the measurements that apply to time domain can also apply to, or have the corresponding variance for, the frequency domain. Some of these methods (for example, coherence, Granger causality or Pearson correlation coefficient) are established on a rigorous statistical theoretical system, while many others are not, such as Phase Lock Value (PLV). More problems about the interpretation of the functional connectivity metrics were also discussed (*Bastos and Schoffelen*, 2016). In addition, the majority of the methods involve intense computation in terms of time and computing resources. Due to the intrinsic properties of the statistical metrics, a careful assumption on the statistical distributions of the data might be necessary when choosing the optimal method.

Further investigation and development on the appropriate metrics to quantify functional connectivity is critical. In Chapter II, the work on a novel technique is introduced, which captures the non-linear relationship of the neuronal activities in an efficient computational manner, and can be applied in both bidirectional and unidirectional ways. It is capable of solving the problem of fluctuating connectivity over time by being designed to apply to datasets on an extended time scale. We present results of using this new method to *in vivo* data.

1.3.2 Neural oscillation and network synchronization

One prevalent characteristic of functional connectivity is the emergence of synchrony. Synchrony refers to behavior where a cell assembly or assembly populations interact with each other and finally fire together (*Fell and Axmacher*, 2011). Synchrony can emerge as a single burst of activity or as repeating rhythmic bursts or coherent oscillations that happen at different spatio-temporal scales. Synchrony is thought to support the "binding" problem. The "binding" problem refers to the phenomenon that each visual feature of one object is stored and processed in a separate brain region, but all the features are combined to a unified representation for the object, avoiding incorrect combinations when more than one object is presented simultaneously. This combination action is argued to realize via synchronizing the activities of neurons that are activated by the same object (*von der Malsburg*, 1999). A general advantageous function of the oscillatory or synchronous firing is to simultaneously recruit neuronal populations both locally and globally in an energy-efficient way, allowing for large-scale synchronous interaction across distant areas (*Buzsáki*, 2004a).

1.3.2.1 Definition and experimental evidence

Neural oscillations have been studied intensively over the last decades, since they were first discovered in 1929 (*Buzsáki*, 2006). Rhythmic activities can happen at multiple temporal and spatial scales. For example, local field potential (LFP) is the summed activity of hundreds or thousands of locally-connected neurons while EEG and MEG involve millions of neurons across brain regions at a macroscopic level. A complete classification of oscillatory brain activity observed in different frequency bands is displayed in Figure 1.3. In this classification, each band detected in the same brain region is thought to associate with different functions, giving a linearly-distributed mean frequency at the natural log scale (*Kopell et al.*, 2000; *Buzsáki*,

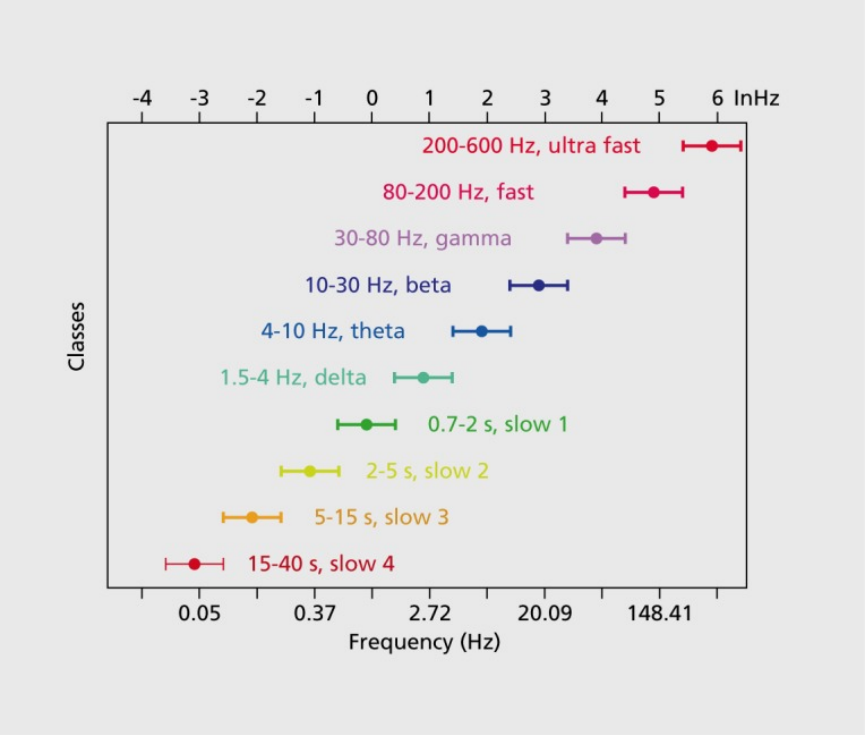

Figure 1.3: A system of oscillation bands. Figure from *Buzsáki* (2004a)

2004a).

Oscillatory and synchronous patterns can emerge at various scales and have been identified in a number of anatomical locations. The "local synchrony" at a microscopic level usually means a group of neurons clustered together tend that get in to the same resonant mode, at a spatial scale less than 2mm (*Gray*, 1999). At a macroscopic level, synchrony involves distant locations, for example, locations across hemispheres that are separated by greater than 1cm in space and about 8-10ms in transmission time (*Girard et al.*, 2001), or locations connected by cortical-cortical or thalamocortical fibers in physiology (*Llinás et al.*, 1998). At the intermediate scale, mesoscale synchronization concerns hundreds or thousands of neurons at the timescale of milliseconds, which is normally measured by multi-unit spikes or LFPs (*Bressler and Kelso*, 2001; *Varela et al.*, 2001).

Therefore, there are different approaches for detecting synchrony: 1) Spike-spike: temporal coherence between spike trains from a pair of neurons, which can be quan-

tified in various statistical metrics defined to capture different firing patterns, such as synchrony index (*Golomb and Rinzel*, 1994) or mean phase coherence (*Mormann et al.*, 2000); 2) Spike-field coherence: when the action potentials tend to fire at the same phase relative to oscillatory activity occurring in the local network; 3) Field-field: the correlation between oscillatory activity in two brain regions, including phase-phase coupling or phase-amplitude coupling within the same frequency band or across different bands (*Fell and Axmacher*, 2011).

1.3.3 Functional roles of oscillations and synchronization

Both oscillatory activities and synchronous firings have been found to support a wide variety of functions at the circuit and cognitive level, such as encoding information precisely, shaping synaptic plasticity, binding neuron populations for integration, facilitating short-term and long-term memory as well as memory consolidation, etc. (*Varela et al.*, 2001; *Engel et al.*, 2001; *Buzsáki*, 2004a; *Kahana*, 2006; *Buzsáki and Watson*, 2012; *Ognjanovski et al.*, 2017; *Durkin et al.*, 2017; *Ognjanovski et al.*, 2018; *Puentes-Mestril et al.*, 2019). Synchronization has been proposed to support neural communication, for example, binding functions to combine distributed features into the same object, which was hypothesized as a fundamental mechanism of effective communication between structures refered to as *communication-through-coherence* (CTC) (*Fries*, 2005). Spike-field coherence between lateral geniculate nucleus (LGN) neurons and primary visual cortex (V1) oscillations are found to be enhanced significantly following a novel visual stimulus, and oscillations during non-rapid eye movement (NREM) have been shown to be essential for information transfer and synaptic plasticity between two regions in mice (*Durkin et al.*, 2017). In experiments with contextual fear conditioning (CFC), successful memory consolidation is associated with augmented network oscillations at delta, theta, and ripple (150-250Hz) bands as well as increased network firing coherence in the hippocampus (*Ognjanovski*

et al., 2017).

Oscillations and synchronization in the theta band and the gamma band are studied extensively in particular. For example, in one experiment called "yellow cab", where the subjects gradually learned to find the shortest path between two random sites through repeated trials in a virtual town, an increase in the power of the theta band was detected during locomotion, orienting and conditioning(*Caplan et al.*, 2003). Oscillatory activities at theta power across a wide range of cortices from invasive recording of epileptic patients increased a lot when the patients were moving in comparison to when they sitting still (*Caplan et al.*, 2003). Similar results from intracranial electroencephalographic (iEEG) were observed in both the hippocampus and the neocortex (*Ekstrom et al.*, 2005). Another major function where the theta band is found to be crucial is memory tasks. Theta power also increases significantly in human scalp EEG and MEG recordings during verbal memory tasks (*Raghavachari et al.*, 2001; *Jensen and Tesche*, 2002). During both memory encoding and retrieval in a verbal working memory experiment, theta power in cortical and hippocampal regions is found to reset just after the consonant stimuli, which arrive at random phases to the ongoing oscillation (*Rizzuto et al.*, 2003), and the coherence of the theta rhythms has been shown to enhance (*Sederberg et al.*, 2003; *Weiss and Rappelsberger*, 2000; *Klimesch et al.*, 2005).

Gamma oscillations are highly associated with attentional processing and object recognition (*Gruber*, 2004), as well as the memory capacitance of working memory tasks (*Howard*, 2003). In processes requiring precise timing such as efficient communication across brain regions, gamma phase synchronization was demonstrated to support information propagation in both a top-down and a bottom-up manner (*Engel et al.*, 2001; *Fries et al.*, 2001; *Jacobs et al.*, 2007; *Womelsdorf et al.*, 2007). Synaptic integration normally needs to happen at the scale of milliseconds (*Daoudal*, 2003), which is around the time period of gamma oscillations. For this reason, phase

synchronization in the gamma band allows for efficient information communication between anatomical locations (*Fell and Axmacher*, 2011). Another mechanism proposed for this function of gamma phase synchronization is that the depolarization part of each gamma cycle (called up states) increases the probability of neural membrane potentials passing the threshold and thus firing, resulting in action potentials that fire at one region during up states most likely arriving at the other region also during up states, and thus triggering action potentials effectively (*Womelsdorf et al.*, 2007). Moreover, gamma oscillations are thought to support synaptic plasticity. When postsynaptic neuron fires persistently later than presynaptic neuron by less than 20ms, the synapse between them is strengthened (*Caporale and Dan*, 2008), referred to as long term potentiation (LTP). Therefore, the time window provided by the most depolarizing quarter of gamma oscillations facilitates the phase synchronization between presynaptic and post synaptic neurons, thus promoting LTP (*Axmacher et al.*, 2006).

Besides the functions of each individual band, cross-frequency coupling between the synchronized oscillations in different bands is also widely observed and shown to play significant roles. For example, theta-gamma coupling is thought to facilitate the interaction between working memory and long-term memory by providing a better timing precision with the combination of two frequencies compared with just fast gamma oscillations (*Fell and Axmacher*, 2011). Another recently proposed framework states that the phase-locking between gamma oscillations and alpha oscillations serves to organize spatial distributed information (*Jensen et al.*, 2014). Fast inhibition in the gamma band segments each neuronal representation and inhibitory alpha oscillation activate the representations sequentially on a longer time scale, thus prioritizing the neuronal processing for downstream regions. In cross-modal processing, phase-phase coupling between the low frequency band in auditory and olfactory cortices, as well as the coupling between low frequency phase and high frequency amplitude are observed only when the auditory and olfactory cues are matched successfully, which indicates

the fundamental role of the cross-frequency synchronization (*Zhou et al.*, 2019).

1.3.3.1 Generation mechanisms

The generation mechanisms of neural oscillatory activity or synchronization, which are not fully understood yet, can be classified into two categories. One is the resonance-based mechanism, in which the collective oscillatory activity is driven by the natural firing frequency of neurons, while the other mechanism is inhibition-based, which is more driven by recurrent synaptic connections at the network level.

Resonance in neural networks means that the response of the membrane voltage is maximized when the frequency of the oscillatory input matches the intrinsic or natural frequency of the neuron or the network. Neurons that display such sensitivity to external input frequency are "resonators". Resonant behaviors in response to sub-threshold input were observed in various brain regions, including neocortical neurons (*Hutcheon et al.*, 1996), hippocampus CA1 (*Leung and Yu*, 1998), the olfactory amygdala (*Sanhueza and Bacigalupo*, 2005) and thalamic neurons (*Puil et al.*, 1994). A network composed of neurons with the same intrinsic frequency are easily synchronized under external input. Furthermore, instead of an unchanged value, the natural frequency of neurons can actually be shifted based on the depolarization level of the input (*Hu et al.*, 2002; *Wang*, 2010; *Yan et al.*, 2012), allowing for more flexibility in the interactions between the network and external driving cross a broader range of frequencies as well as more complex pattern formations (*Lau and Zochowski*, 2011) and functional processes, such as memory retrieval (*Roach et al.*, 2018). For example, this property provides a mechanism to amplify weak signals between different cortical regions which are weakly-connected, thus contributing to a reliable method for the propagation of synchronous activities and generating coherent oscillations (*Hahn et al.*, 2014). Also, a highly synchronous activity, called bursting, is proposed to serve as a mechanism for selective communication via frequency preference, where a

bursting activity at a specific frequency is more likely to activate neurons having the same resonance frequency, compared with other neurons which do not. (*Izhikevich et al.*, 2003).

In the other category of mechanisms, network oscillations are believed to be generated from rhythmic inhibitory volleys(*Buzsáki and Watson*, 2012). The fact that the neurons receiving IPSPs are more synchronized than those receiving EPSPs (*Lytton and Sejnowski*, 1991) leads to the assumption that $GABA_A$ receptor–mediated inhibition plays a central role in the generation of gamma oscillations (*Buzsáki and Wang*, 2012). The most well-understood and observed inhibitory neuron type is parvalbumin positive (PV+) interneurons, of which the roles in gamma generation have been supported by extensive experimental findings (*Buzsáki et al.*, 1983; *Whittington et al.*, 1995; *Csicsvari et al.*, 2003; *Mann et al.*, 2005; *Hájos and Paulsen*, 2009; *Hasenstaub et al.*, 2005). The roles of other interneurons, such as CCK interneurons, and hippocampal CA1 bistratified neurons, are understood less and proposed to be responsible for slower oscillations and to contribute to cross-frequency coupling via the interaction with PV interneurons (*Pike et al.*, 2000; *Gloveli et al.*, 2004). Two popular models proposed for gamma oscillation generation are I-I or interneuron gamma (ING), and E-I or pyramidal-interneuron gamma (PING). I-I model or ING mechanism only involves inhibitory neurons (*Wang and Rinzel*, 1992; *Whittington et al.*, 1995), and even though the driving to the network is stochastic, inhibitory cells fire intrinsically and are able to synchronize amongst themselves by gating the timing of their firing. The synchronous inhibitory signal can then synchronize downstream populations of neurons. (*Brunel*, 2000; *Ardid et al.*, 2010).

In the E-I model or PING mechanism, the oscillation is generated from the cyclic alternation between excitation and the following inhibition by some delay (*Wilson and Cowan*, 1972; *Brunel and Wang*, 2003; *Geisler et al.*, 2005). This time delay actually reflects the prominent features of the gamma oscillation (*Csicsvari et al.*,

2003; *Mann et al.*, 2005; *Hájos and Paulsen*, 2009). In this model, the oscillation or synchronous firing is driven by the excitatory (E) to inhibitory (I) connections, which is supported by the fact that the gamma power decreases when the E-I connections are weakened (*Fuchs et al.*, 2007). When the E cells get more depolarized and fire at a higher rate, the firing rate of I cells will also increase due to more excitatory current received, which will in turn decrease the firing rate of E cells. However, increased firing rate of I cells will result in the decrease of E cells firing rate, then causing the firing rate of I cells to decrease. These dynamics contribute to the robustness of the oscillation against changes in depolarization (*Tiesinga and Sejnowski*, 2009). In PING, the relative relationship or the balance of excitation and inhibition may be important. For example, a specific ratio between excitatory and inhibitory firing rate needs to be conserved for the emergence of synchronous oscillations (*Buia and Tiesinga*, 2006).

Both ING and PING models are supported by experimental findings. The specific relationship between the two models in reality is still under debate, with some evidence showing that the two cooperate with each other in the brain (*Buzsáki and Wang*, 2012). Recently, rhythmical activation of interneurons via optogenetic techniques has been found to enhance coherent oscillations in hippocampus CA1 and to be able to rescue memory formation which is impaired by sleep deprivation (*Ognjanovski et al.*, 2018). Silencing interneurons results in disruption of neuronal oscillations, which further affects neural plasticity (*Durkin et al.*, 2017) and memory performance (*Ognjanovski et al.*, 2017). However, in this process of artificial stimulation of inhibitory neurons, the relative relationship between excitation and inhibition may also be altered, of which the effects need to be discussed more carefully.

In the modeling work shown in the following chapters, the two mechanisms for synchrony, resonance-based and inhibition-based, can coexist in a network, allowing the network to transition between them depending on levels of excitation and

inhibition in the network.

1.4 Excitatory and Inhibitory Balance

The concept of excitatory/inhibitory balance (E/I balance) in neural networks was first brought up in 1996 as the approximate equality of excitatory and inhibitory inputs into neurons connected in a sparse but strong way, in order to explain the generation of irregular firing patterns and chaotic dynamics (*van Vreeswijk and Sompolinsky*, 1996). Soon after, this hypothesis was further supported by computational work (*Troyer and Miller*, 1997; *van Vreeswijk and Sompolinsky*, 1998). Ever since then, this concept of 'balanced excitation and inhibition' has aroused extensive interest in both theoretical and experimental research. The original meaning of E/I balance is referred to as loose balance in later research. Definitions of different types of balance have been developed, such as tight balance and precise balance, where excitation and inhibition are temporally related. E/I balance has been argued to play a significant role in many cognitive functions.

1.4.1 Experimental evidence

Excitation and inhibition have been observed to be closely related both at functional and synaptic levels in a wide variety of brain regions during different brain activities by a large body of experimental work. Measurements of the correlation between excitation and inhibition in experiments can be classified into two major categories based on the experimental conditions: the sensory response under external stimuli and the maintenance of spontaneous neural activity. In the first class, the response of excitatory conductances and inhibitory conductances are similar when stimulated, such as responses to frequency or tone stimuli measured in the auditory cortex (*Wehr and Zador*, 2003; *Zhang et al.*, 2003; *Zhou et al.*, 2014), to orientation stimulus and spatial frequency in the visual cortex (*Tan et al.*, 2013; *Liu et al.*, 2009),

to odor stimulus in the olfactory cortex (*Poo and Isaacson*, 2009), and to direction in the barrel cortex (*Wilent and Contreras*, 2005). Results were collected in different layers within each cortical area and in awake/anesthetized states, either *in vitro* or *in vivo* (*Wilent and Contreras*, 2005; *Poo and Isaacson*, 2009; *Okun and Lampl*, 2008; *Murphy and Miller*, 2009; *Wehr and Zador*, 2003), indicating that this co-tuning relationship between excitation and inhibition exists universally in the brain. Taking a more detailed look into these results, some of them reported a relatively loose correlation where only the strengths of excitation and inhibition co-vary and inhibitory GABAergic synapses have a broader tuning than excitatory ones (*Zhou et al.*, 2014), while others showed more strict correlation. For example, some results demonstrate identical or even indistinguishable profiles for excitatory and inhibitory types of conductances as well as a consistent temporal delay between the onsets, where the excitation arrives first and gets quenched by the inhibition on a scale of milliseconds (*Wehr and Zador*, 2003). Both types of correlation, with or without the temporal relationship, were observed in all the cortical areas mentioned above. More interestingly, in the same experiment, the general type of correlation was found in the tuning for orientation stimulus while the detailed type was found in spatial frequency stimulus (*Cardin et al.*, 2007). Besides the tuning curve, the postsynaptic potential traces generated by the excitatory and inhibitory inputs were observed to correlate closely in timing as well as strength, in both spontaneous activity as well as under excitatory and inhibitory somatosensory stimulation (*Okun and Lampl*, 2008). Furthermore, the excitatory postsynaptic current (EPSC) and inhibitory postsynaptic current (IPSC) recorded using voltage clamp exhibit the same amplitudes on a cycle-by-cycle basis during gamma oscillations (*Atallah and Scanziani*, 2009).

Conversely, disruption of this balance may cause many neurophysiological pathologies (*Tatti et al.*, 2017). Some possible causes of the imbalance may be impaired connectivity in circuits by altered plasticity (*Patel et al.*, 2015), changes in homeo-

static plasticity (*Whitt et al.*, 2014), improper regulation of neurotransmitter release (*Takada et al.*, 2015) or improper expression of receptors (*Catts et al.*, 2016; *Tong et al.*, 2015). For example, experimental studies on epilepsy have reported disinhibition that is potentially caused by disregulation of excitatory input to inhibitory neurons (*Zhou et al.*, 2009). This similar decrease of inhibition caused by the lack of expression of inhibitory receptors was also observed in schizophrenia (*Kehrer*, 2008), and hyperactive cortical circuits were identified due to an increase in excitatory neurons in a disease with autistic cognitive developmental problems (*Tervonen et al.*, 2009).

1.4.2 Theoretical work and hypotheses

These experiments have strongly supported that correlation and interaction between excitation and inhibition exists universally in the brain. However, each individual experiment actually focused on different variables and had different definitions in the study of the balance. So what is this "balance" exactly? And to what extent are excitation and inhibition actually balanced, given that various correlations were observed? Moreover, how is the balance even generated and maintained in the brain? Some hypotheses on different types of E/I balance were proposed based on these questions, which still remain open.

The first type is *global balance* or *loose balance*, which is basically the same as the original definition, meaning that excitatory and inhibitory signaling in the network approximately cancel each other over a relatively long period of time, leaving a random walk of the neuronal membrane potential and thus generating irregular spiking (*Denève and Machens*, 2016), as in the observations of those tuning curves generally matching each other but with no close temporal correlation (*Kerlin et al.*, 2010; *Wu et al.*, 2008). The next type with a relatively closer correlation is called *detailed balance* which means excitatory and inhibitory input relevant to a specific

signaling pathway can cancel each other when multiple signals exist, which actually leaves the target neurons unresponsive (*Vogels and Abbott*, 2009). A further stringent category called *tight balance* was proposed to address the problem of inefficient coding ofrandom spiking firing and occurs when inhibition tracks excitation closely with small time delays. The combination of detailed balance and tight balance gives *precise balance*, which requires both fine tuning as well as the temporal relationship (*Hennequin et al.*, 2017).

Mechanistic understanding of the functional roles of E/I balance has also been actively explored, with multiple hypotheses proposed. One proposal is the gating mechanism of precise balance, which is thought to improve the timing precision during information processing where the neuron has a narrow window to fire during the short delay of inhibition relative to excitation (*Hennequin et al.*, 2017). A recent *in vitro* study actually shows an almost identical ratio between excitation and inhibition displaying precise balance and demonstrating a relationship between the time delay and the synaptic strength (*Bhatia et al.*, 2019).

Another popular model called Balance Amplification was proposed to explain selective amplification, indicating that the neural circuits selectively amplify some firing patterns to enhance the signal-to-noise ratio under external stimuli. This model indicates that when a steady balance pattern is established by a given input, the imbalance between the firing rate of excitatory and inhibitory populations (referred to as "difference patterns") can drive and amplify the balance pattern (referred to as "sum patterns") via strong recurrent connections (*Murphy and Miller*, 2009). This amplification process has been demonstrated to address the two major problems of the traditional model, Hebbian amplification, which are slowness in responses and instability of dynamics caused by small structural perturbations (*Murphy and Miller*, 2009; *Hennequin et al.*, 2017). This mechanism has achieved great success in explaining activity in the visual cortex of cats (*Murphy and Miller*, 2009) and in the macaque

cortex, where it is found that the signal propagates effectively across cortical areas via balance amplification (*Joglekar et al.*, 2018).

A third model is the *inhibition-stabilized* network where strong negative feedback from inhibition stabilizes activity of an excitatory network, thus constraining the activity from "running away" (*Kandel et al.*, 2012). This is supported by evidence in the zebrafish homolog of the olfactory cortex, where both tight balance and detailed balance were observed at the same time (*Rupprecht and Friedrich*, 2018). A novel mechanism was proposed to model decision making, where two excitatory circuits representing two choices are mediated by a common inhibitory circuit. When the biased or unbiased input comes, the system has to fall in one of the bistable states dependent on the relative interaction of the inhibitory circuit with the two excitatory ones (*Wang*, 2008).

1.5 Outline

The work presented in this dissertation aims to provide a theoretical framework to understand the mechanisms and the functional roles of heterogeneous E/I balance states using computational modeling and statistical analysis. First, a method to infer functional connectivity and network stability is extended in Chapter II, together with the analysis of *in vivo* datasets using this method. Observed functional dynamics regulated by the inhibitory neurons, demonstrated in the analysis results, inspired the modeling work in Chapter III to systematically study the interaction between excitatory and inhibitory neural populations. Based on the multiple identified mechanisms for obtaining E/I balance in those results, Chapter IV focuses on the dynamical effects on network firing patterns under external oscillations when the system sits at different E/I balance states.

As mentioned above, a reliable and efficient statistical metric to measure functional connectivity in large scale neurological recordings is essential. In Chapter II, I

develop an analytical framework which makes use of the Average Minimal Distance (AMD) between spike trains to quantify the functional connectivity between neuron pairs, and further makes use of Functional Network Stability (FuNS) to measure whether the functional patterns stay invariant over extended time period. In collaboration with my lab mates and the Aton lab, this method is tested on surrogate data, computational modeling as well as *in vivo* recordings from mouse hippocampus and visual cortex. Compared with traditional techniques such as cross-correlation, AMD and FuNS display a more robust and significant performance with a computation time up to 4 fold less, and with fewer hyper-parameters. The analysis data indicates that oscillatory driving to the inhibitory parvalbumin positive (PV+) interneurons stabilize the functional patterns, which actually improves memory consolidation.

We subsequently used AMD-FuNS to measure the functional patterns in different brain regions such as the hippocampus, primary visual cortex and lateral geniculate nucleus (these results are not part of this dissertation, see *Ognjanovski et al.* (2017); *Durkin et al.* (2017); *Roach et al.* (2018)). We then set out to explore what mechanisms are underlying the experimentally observed patterning. To probe the detailed mechanisms of E/I balance in terms of the network and cellular properties, in Chapter III, I build a computational network composed of excitatory and inhibitory Hodgkin-Huxley neurons of type 1 excitability and systematically vary the synaptic strength. Most previous computational work was done with simplified neural models such as the integrate-and-fire model, which does not capture all the biological realism of the neurons. Although different types of balance have been observed and classified, as listed above, the network environment required by each type is unknown. The model results give a complete characterization of the trajectory of the changes in E/I ratio with various levels of network coupling strength. This trajectory provides a theoretical basis to understand the transition of the network from a more general balance to a more precise balance with the increase of synaptic strength. In addition, three

balance regimes with different mechanisms and firing coherence emerge. The mechanisms generating these three balance regimes differ from each other based on the competitive dynamics between the firing rate and depolarization driving force, where the former dominates in a relatively loose balance at weak coupling while the latter contributes to the second regime at medium coupling. Moreover, by manipulating the network topology, I find that global inhibition has a stronger effect than global excitation, which is able to keep the system trapped in an inhibition-dominant regime even at high excitatory synaptic strength.

Continuing this line of work, I study how the network dynamics change at different E/I balance states when interacting with an external oscillation in Chapter IV. Here I use a neuron model with type 2 excitability, which displays a stronger resonance property in response to rhythmic input and propensity to synchronize. Model results show two synchronization regimes at different E/I levels. External oscillation at the natural frequency of the neurons synchronizes the network and stabilizes the inter-bursting intervals in a first regime when the synaptic strength is weak. At higher synaptic strengths, the system transits into a second regime when spontaneous oscillations emerge and the effect of external oscillations disappear. In this regime, the intrinsic interaction between excitatory and inhibitory currents accounts for synchronization on a cycle-by-cycle basis. In the first regime, clear ordered spiking patterns appear in the resonant oscillation, which may lead to the prediction that the oscillation enhances the information encoding process only when the system is at the appropriate balance states.

CHAPTER II

Functional Network Stability and Average Minimal Distance – A framework to Rapidly Assess Dynamics of Functional Network Representations

This work was done in collaboration with my lab mates and the experimental data is from Aton Lab. I did the work presented in Results section 2.3.1 and 2.3.3.

2.1 Introduction

New multisite recording techniques have generated a wealth of data on neuronal activity patterns in various brain modalities (*Buzsáki*, 2004b; *Lichtman et al.*, 2008; *Luo et al.*, 2008; *Chorev et al.*, 2009). An unresolved question is how, using such data sets, one can correctly identify large-scale network dynamics from populations of neurons which either may, or may not, include neurons involved in a particular cognitive process of interest. This is due in part to the fact that even high-density recordings sample only a sparse subset of the neural system responsible for the modality in question. It is also complicated by the inherent separation of temporal scales over which neural vs. behavioral measurements occur.

In response to this question, multiple linear and non-linear techniques have been developed over the years to assess functional connectivity between neurons, and to possibly infer from it structural connectivity (see for example: (*Friston et al.*, 2013; *Bastos and Schoffelen*, 2016; *Cimenser et al.*, 2011; *Cestnik and Rosenblum*, 2017; *Zaytsev et al.*, 2015; *Poli et al.*, 2016; *Shen et al.*, 2015; *Wang et al.*, 2014)). More recent approaches utilize network theory to establish links between recorded data and the underlying connectivity (see for example: (*Newman*, 2004, 2006, 2010; *Ponten et al.*, 2010; *Rubinov and Sporns*, 2010; *Sporns et al.*, 2000; *De Vico Fallani et al.*, 2014; *Supekar et al.*, 2008; *Boccaletti et al.*, 2006; *Stafford et al.*, 2014; *Petersen and Sporns*, 2015; *Misic and Sporns*, 2016; *Park and Friston*, 2013; *Bassett et al.*, 2010; *Feldt et al.*, 2009; *Gu et al.*, 2015; *Medaglia et al.*, 2017; *Davison et al.*, 2015; *Hermundstad et al.*, 2011; *Bassett et al.*, 2011; *Shimono and Beggs*, 2015; *Nigam et al.*, 2016; *Nakhnikian et al.*, 2014; *Pajevic and Plenz*, 2009)). The idea is that, by estimating networks based on functional interactions, one can potentially gain insight into global dynamics, which reflect the general property of the whole network, instead of a specific subset of neurons. While all these approaches can provide insightful information, they share some the same problems. These methods are often limited by under-sampling (and potentially unrepresentative sampling) of neuronal recordings, and are not optimized for monitoring changes in network structure across extended time periods (i.e., those associated with behaviors of interest, such as memory formation).

Here we propose a novel technique that rapidly estimates functional connectivity between recorded neurons. Then, rather than characterizing details of the recovered network, the metric measures changes in the network dynamical stability over time. The technique is based on an estimation of Average Minimal Distance (AMD) between spike trains of recorded neurons, a metric which has previously been compared to other clustering algorithms (*Feldt et al.*, 2009). Here, we expand on this work and

show that the analytic estimation of AMD for the null case, when the two cells are independent, allows for rapid estimation of the significance of pairwise connections between the spike trains, without need for time-expensive bootstrapping. Further, Functional Network Stability (FuNS) is introduced and is monitored over timescales relevant for behavior. We show that FuNS measures global change in network dynamics in response to localized changes within the network. This, in part, alleviates the problem of sparse sampling so prevalent in neuroscience.

Below, the statistical underpinnings of AMD and FuNS are detailed. We compare AMD and cross-correlation (CC) on both surrogate data and model simulation data. Model results show the applicability of AMD and FuNS on excitatory-only networks, as well as on mixed networks of excitatory and inhibitory neurons poised near a balance between excitation and inhibition, a regime thought to be a universal dynamical state achieved by brain networks, resulting in enhanced information processing properties (*Froemke*, 2015; *Barral and Reyes*, 2016; *Poil et al.*, 2012; *Berg et al.*, 2007; *Rubin et al.*, 2017). We end by analyzing experimental data recorded from the mouse hippocampus during contextual fear memory formation. Our results indicate that AMD yields results comparable to that of the gold-standard CC, but, importantly, it is orders of magnitude faster and reports statistically significant increases in FuNS due to behavioral-based network topological changes compared to CC FuNS.

2.2 Methods

2.2.1 Statistical Methods

2.2.1.1 Average minimal distance (AMD) and its significance estimation

Pairwise functional connectivity is estimated using average minimal distance (AMD) (*Feldt et al.*, 2009) (Figure 2.1) separating the relative spike times between neurons. AMD is calculated as follows: given the full spike trains $\{ S_1, S_2, \ldots, S_n \}$

Abbreviation	Full Name
AMD	Average Minimal Distance
CA1	Cornu Ammonis 1
CC	Cross-correlation
CFC	Contextual Fear Conditioning
E/I	Excitatory/Inhibitory Ratio
FC	Functional Connectivity
FCM	Functional Connectivity Matrix
FSM	Functional Stability Matrix
FuNS	Functional Network Stability
IAF	Integrate and fire
ISI	Interspike interval

Table 2.1: List of Common Abbreviations

for n neurons within a network, the pairwise functional relationship, FC_{ij}, of the i^{th} and j^{th} neurons is evaluated by comparing the average temporal closeness of spike trains S_i and S_j to the expected sampling distance of train S_j (Figure 2.1a). That is, $AMD_{ij} = \frac{1}{N_i}\sum_k \Delta t_k^i$, where N_i is the number of events in S_i and Δt_k^i is the temporal distance between an event k in S_i to the nearest event in S_j. With AMD measured, the functional connectivity (FC) is calculated as $FC_{ij} = \sqrt{N_i} * \frac{(AMD_{ij} - \mu_j)}{\sigma_j}$, which is expressed in terms of probabilistic significance of connectivity between pair ij. The mean and standard deviation, μ_j and σ_j, of the expected sampling distance, assuming that the spike trains are independent, can be calculated from either: 1) boot-strapping (i.e. randomizing the spike trains multiple times and reassessing the AMD for the null hypothesis being statistically independent of the two spike trains), or 2) numerical estimation of expected values given the distribution of inter-spike intervals (ISIs) on S_j. Hereafter, the analytical method is referred to as "fast AMD" and the bootstrapping method as "bootstrapped AMD" . For a system with n neurons, the functional connectivity value between each pair of spike trains is calculated, generating an n-by-n Functional Connectivity Matrix (FCM).

In the fast AMD approach, the maximal distance between an input spike and any spike in the spike train to be analyzed is $\frac{ISI_i}{2}$. Then, the expected mean distance

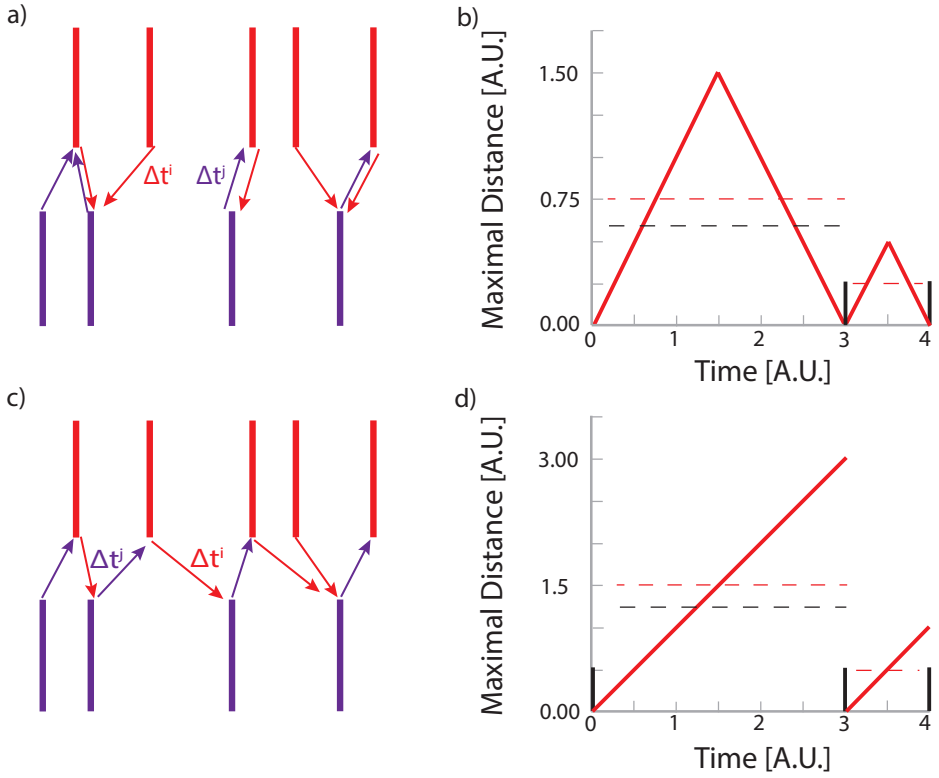

Figure 2.1: Calculation of AMD and analytical significance. The average minimal distance algorithm calculates shortest temporal length between spikes emitted by a neuron to the closest spikes in a reference neuron, looking in either both temporal directions (a), or in a single temporal direction (b), e.g. forward in time. The maximal possible distance between spikes is either half the interspike interval (c) or the full interspike interval (d), when looking in either both temporal directions or a single temporal direction, respectively. The measurements require a collective average timing sequence to be below one quarter (bidirectional) or one half the interspike interval (unidirectional) in order to be considered significant.

between spikes in the independent spike trains is $\mu_i = \frac{ISI_i}{4}$, where ISI_i is the corresponding interspike interval of spike train i (Figure 2.1b). Calculating the first and second raw moments from the maximal distance then yields $\mu_1^L = \frac{1}{4}L$ and $\mu_2^L = \frac{1}{12}L^2$ for a specific ISI with length L. Taking into account the probability of observing an ISI with length L over the recording interval T, $p(L) = \frac{L}{T}$, the first and second moment for sampling the whole spike train randomly are then $\mu_1 = \sum_L \frac{L}{T}\mu_1^L = \frac{1}{4T}\sum_L L^2$ and $\mu_2 = \sum_L \frac{L}{T}\mu_2^L = \frac{1}{12T}\sum_L L^3$, respectively. The expected mean and standard deviation of a random spike train are then calculated as $\mu = \mu_1$ and $\sigma = \sqrt{\mu_2 - \mu_1^2}$.

2.2.1.2 Unidirectional AMD for causality detection

The bidirectional AMD described above (i.e. the temporal distance between spikes of two different neurons, measured in either direction) can be extended to be unidirectional to identify causality between the two spike trains. In this scenario, the temporal distance is measured only forward in time and the mean delay time expected within the null hypothesis (i.e. independence of both spike trains) is only set to $\mu_i = \frac{ISI_i}{2}$, assuming a maximal temporal distance equal to the ISI (Figure 2.1c and 1d). The calculation of first and second moment change accordingly to $\mu_1 = \frac{1}{2T}\sum_L L^2$ and $\mu_2 = \frac{1}{3T}\sum_L L^3$; the mean and standard are then calculated in the same manner as above.

2.2.1.3 Functional Stability Matrices (FSMs) and functional network stability (FuNS)

The fast AMD metric offers critical advantage over the bootstrapped AMD method, as well as over the standard CC method, for quantifying functional connectivity measured over behaviorally-relevant timescales (i.e., hours to days). It allows rapid analysis of functional connectivity that can then be used to link neuronal activity with behavior. The speed of the fast AMD metric is utilized to introduce Functional net-

work stability (FuNS) as a way of measuring the dynamics of functional connectivity over time. Namely, we want to assess the stability of functional connectivity between the neurons within the network rather than to characterize the detailed network connectivity, which, again, is usually based on extremely sub-sampled systems. The remainder of this section is focused on characterizing the stability metric. Later, we show that changes in stability provide information about gross structural changes in the network.

Calculating the stability of network-wide functional connectivity patterns across time requires a division of the data sets into at least two time-windows; the remaining theoretical discussion assumes two time-windows for simplicity. The functional connectivity matrices are denoted as F^A and F^B where A and B represent the first and second time windows, respectively. The functional stability between these data sets is then calculated using cosine similarity, $C_{A,B} = cos\theta_{AB} = \frac{<F^A,F^B>}{\sqrt{<F^A,F^A>*<F^B,F^B>}}$, with an absolute value of 1 denoting no change (maximum similarity) and 0 indicating great change (no similarity; orthogonality) between the time intervals (Figure 2.2a). Functional stability can thus be calculated in a pairwise manner across all time bins for a given recording in order to generate what we call a functional stability matrix (FSM; Figure 2.2b, see also Figure 2.8), or only on directly-adjacent time windows (Figure 2.2a), to generate a single measure of stability: $FuNS = \frac{1}{T}\sum_{t=0}^{T-1} C_{t,t+1}$.

FuNS can also be used to determine the effect behavior has on neural network dynamics. In this scenario, stability is calculated before and after the presence of a synaptic heterogeneity (see Methods 2.2), $FuNS_{A,B}$ and $FuNS_{C,D}$, respectively. The significance of stability increase over many simulations is then given as a Z-score: $Z_s = (\mu_{C,D} - \mu_{A,B})\left(\frac{\sigma^2_{A,B}}{N} + \frac{\sigma^2_{C,D}}{N}\right)^{-\frac{1}{2}}$ with values greater than 2 indicating a significant increase in stability due to behavioral effects and values less than -2 indicating a significant decrease in stability. Here, μ and σ represent the mean and standard deviation of functional network stability, respectively, taken over many

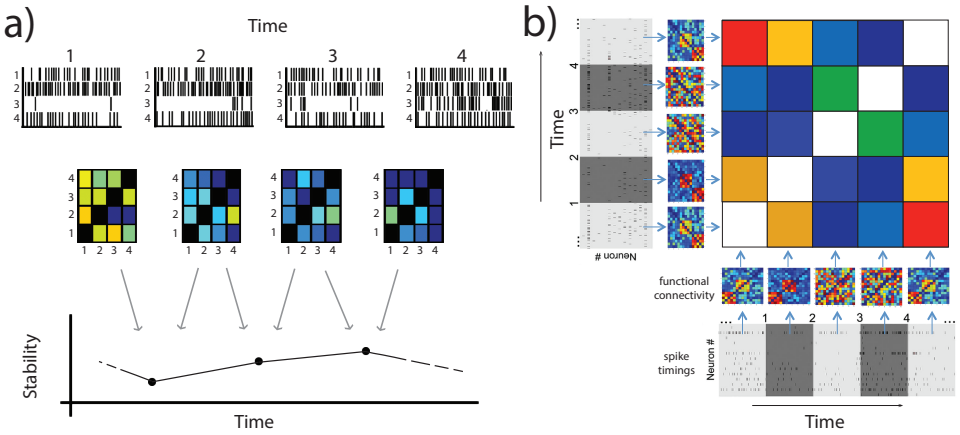

Figure 2.2: Calculation of Functional Network Stability and Construction of Functional Stability Matrices. a) Given the spike time series of neurons (top), the functional connectivity matrices (FCMs) are calculated over each interval (center), whereupon FuNS is calculated by measuring the mean cosine similarity between each consecutive time interval (bottom). b) Alternatively, similarity can be calculated in a pairwise manner across all time intervals to yield the functional stability matrix (FSM).

simulations or recordings.

2.2.2 Computer simulations

2.2.2.1 Simulations of integrate and fire networks

Neural activity is simulated using leaky integrate-and-fire model neurons with dynamics given by $V = -\alpha V + \sum_j \omega_{ij} X_j + I_\varrho$. The summation represents the total input from recently fired (within $\sim$ 20ms) pre-synaptic neurons with connectivity strength ω_{ij} and input dynamics given by the double exponential $X_j = exp\left(-\left(t - t_j^{spk}\right)/3.0\right) - exp\left(-\left(t - t_j^{spk}\right)/0.3\right)$, where t_j^{spk} represents the timing of the last pre-synaptic spike. In addition to synaptic input, each neuron receives noisy input $I_\varrho = 0.15 + 10H\left(\varrho - p\right)$, where H is the Heaviside step function, $\varrho = 10^{-5}$, and $p \in \{[0,1]\}$ is real-valued, random variable generated at every integration step from a uniform distribution.

Networks are formed using 1000 excitatory neurons arranged on a ring network.

Connection densities range from 1.5% to 4.5% of the network population and connection weights range from $\omega = 0.02$ to $\omega = 0.045$ unless stated otherwise. The networks are initially connected locally and subsequently rewired with probability p_r. This parameter is varied from zero to unity, changing network topology from completely local connections to completely random. Each simulation is completed using the Euler integration method.

Additional network are simulated using a mixed population of excitatory/inhibitory cells. In this scenario, connections are completely local ($p_r = 0$), have a connection density of 2% , and synaptic weights are pulled from a uniform distribution $\omega_{ji} \in \{[0, 0.2]\}$. These networks follow the same dynamics as the excitatory only networks, except that 225 inhibitory neurons are added to the existing networks, evenly spaced among the excitatory cells, with inhibitory output connectivity strength $\omega^*_{ji} = -\beta\omega_{ji}$. The variable β is used to investigate network dynamics when excitation or inhibition dominate. We calculate the ratio of excitation to inhibition, E/I, as the ratio between total excitatory to inhibitory synaptic input, averaged over all neurons not in the heterogeneity. Balance between excitation and inhibition (E/I $\sim$ 1) occurs at $\beta = 3.0$.

2.2.2.2 Introduction of synaptic heterogeneities and their long-range dynamical effects

Sensory input causes topological changes in anatomical network structure through both the strengthening and weakening of synapses (*Feldman*, 2012; *Song et al.*, 2000) as well as through the introduction of new synapses (*Ghiani et al.*, 2007) and depletion of unused synapses (*Vanderhaeghen and Cheng*, 2010). Here, we focus solely on the strengthening of synaptic coupling for simplicity. The effect of synaptic strengthening is mimicked by introducing a discrete heterogeneity in network connectivity, i.e. a small, localized region spanning 10% of the network, with increased synaptic

connectivity between nodes. To simplify comparing networks with and without these synaptic heterogeneities, the underlying pairwise connectivity and synaptic strengths are conserved. To analyze the potential long-range effects of such a heterogeneity, we calculate the mean synaptic distance to the heterogeneity for each neuron not in the heterogeneity. The mean synaptic distance here is the average number of steps that need to be taken from neurons in the heterogeneity to any other neuron in the network, along synaptic connections. The calculation of the distance is adopted from *Newman* (2010). In the simplest way, the synaptic distance between every neuron can be measured by calculating A^N, where A is the adjacency matrix and the power N is the number of synaptic steps necessary to reach every other neuron. With each successive multiplication of A, new non-zeros entries appear, representing new long-range (i.e. not directly connected), multi-unit synaptic connections. The synaptic distance d is the number of multiplications of A with itself, necessary to give rise to the new long-range connection. With the full synaptic distance matrix populated, the mean synaptic distance to the heterogeneity is calculated by averaging over all heterogeneity distances calculated for a given neuron. The mean synaptic distance to heterogeneity, and indeed between any two neurons, changes based on the size and connectivity density of the network. We thus normalize the distance to heterogeneity with a value of 1 representing neurons farthest from the heterogeneity, incorporating the entire network, and a value of 0 representing the minimum degree of separation from the heterogeneity (i.e. within the heterogeneity). It should be noted that by definition of d, the shortest distance to heterogeneity would be for a neuron not in the heterogeneity but connected to every other neuron within the heterogeneity, attaining a normalized value of $= \frac{1}{N}$.

2.2.3 Experimental design

2.2.3.1 Recordings from mouse CA1 before and after contextual fear conditioning (CFC)

To test the effects of memory formation on network dynamics in vivo, C57BL/6J mice (age 1-4 months) were implanted with custom-built driveable headstages (see *Ognjanovski et al.* (2014, 2017) with bundles of stereotrodes targeting hippocampal area CA1. Following postoperative recovery, mice were handled daily while gradually lowering stereotrodes into the pyramidal cell layer of CA1 to obtain stable recordings. A 24-h baseline recording of neuronal and LFP activity was initiated at CT0, after which mice underwent a single-trial CFC as described previously. Contextual fear memory was assessed 24 h after CFC, using previously-described methods.

2.3 Results

2.3.1 Comparing AMD and CC in surrogate data

2.3.1.1 Comparison of bootstrapped AMD, fast AMD, and CC for rapid estimation of functional connectivity.

We first compare the bootstrapped and fast AMD metrics for different distributions of ISIs (Figure 2.3): Gaussian, Poisson, uniform, and exponential. To measure the performance of the metrics, a single spike train following any one of these distributions is generated and cloned, with clones receiving a bidirectional jitter of their spike times equal to the jitter width depicted on the x axis (Figure 2.3). The jitter from every spike is drawn from the same distribution as the original spike train, of which the standard deviation serves as the jitter width. For all cases, the mean ISI is arbitrarily chosen to be 33ms (this ISI gives a 30Hz signal, representative of awake brain oscillations). Figure 2.3 depicts the mean z-score and its standard devi-

ation, calculated as a function of the jitter width for the two approaches. In all four instances, the two AMD methods perform nearly identically.

Next, we compare the performance of fast AMD to CC, using the same distributions as above, i.e. Gaussian, Poisson, etc., with jittering (Figure 2.4). To calculate CC between two spike trains, the two spike trains are convolved with a Gaussian having one of three different widths, σ= 1ms, 5ms, or 33ms. Both metrics are calculated for 0 temporal shift between the spike trains. Importantly, we note that AMD does not have any free parameters and, at the same time, better captures finer characteristics for Poisson spike distributions compared to CC with any Gaussian convolution width.

Critically, the fast AMD approach provides a rapid estimation of the significance of pairwise functional connectivity. Figure 2.5 shows the computing times of fast AMD, bootstrapped AMD, and CC with zero time-shift and bootstrapping for spike trains having various numbers of spikes and network sizes. The reduction of the computing time for fast AMD is very significant (up to 10000 times faster) which may be crucial for multiscale data analysis.

2.3.1.2 Comparison of bidirectional and unidirectional AMD performance

Next, the performance of unidirectional fast AMD and bidirectional fast AMD on surrogate data sets is compared (Figure 2.6). A set of 5 spike trains are generated such that they are: 1) coincident (but not causal) with respect to each other, or 2) are causal, with FCMs calculated in each scenario. First, one spike train is generated from a Gaussian distribution. In the case of coincidence, the "master" spike train is copied and each spike is subsequently jittered following the same distribution. This process is repeated, with subsequent spike trains copying the previously jittered spike train. In the case of causality, copied spike trains retain the same interspike intervals as the original master copy, but are delayed slightly in time. Figure 2.6 depicts

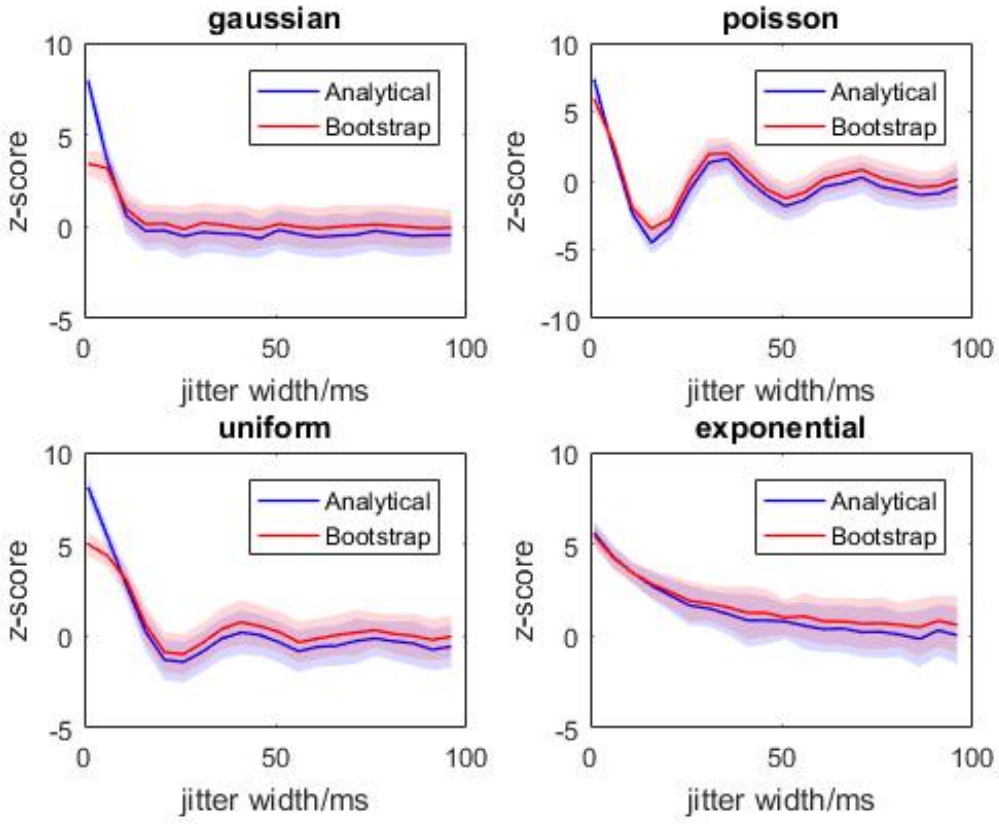

Figure 2.3: Comparison of bootstrapped and fast AMD metrics for rapid estimation of functional connectivity (FC). Two identical spike trains were artificially generated using various distributions of inter-spike intervals: a) Gaussian, b) Poisson, c) uniform, and d) exponential; the second spike train was jittered using the same type of statistical distribution, with various jitter widths (x-axis) to progressively de-correlate the spike trains. Each set of spiking data represents a 1s long recording (the time length is arbitrary, however all values are scaled to length) and contains 30 spikes. The analytical value of pairwise functional connectivity (FC_{21}) is calculated using the method described in the text (Methods 1.1). For all the distributions, AMD detects the significant functional connectivity when jitter width is small. The average value at which FC loses significance is a quarter of mean ISI, 8ms. For a Poisson distribution (b), due to the fact that the mean value and standard deviation are controlled by the same parameter, when the jitter width equals around 17ms, the mean value of jitter is also around 17ms, and the maximal value of the AMD and therefore FC has the most negative value. The same reasoning applies when the jitter width is around 33ms. The significance from bootstrapping was obtained by shuffling the ISIs of the second train 100 times. As before, the Z-score of the AMD values represents the FC. The results agree with the analytical values.

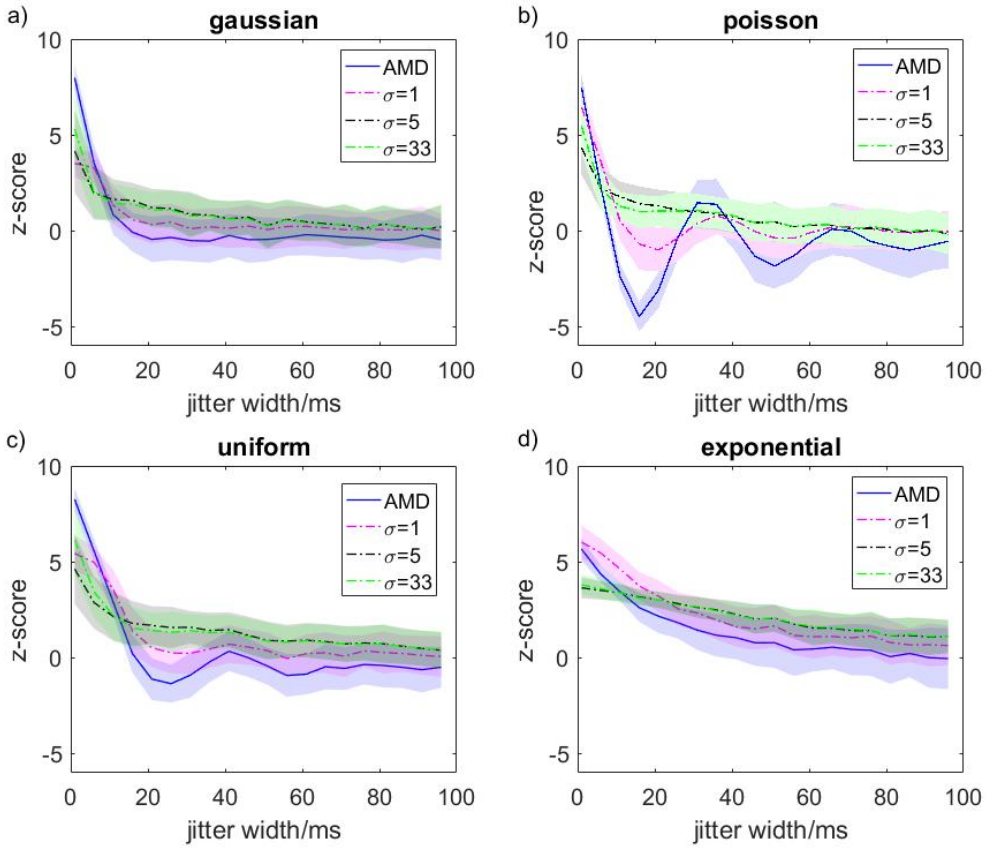

Figure 2.4: Comparison between fast AMD and CC. We compared the traditional cross-correlation (CC) method to fast AMD using a) Gaussian, b) Poisson, c) uniform, and d) exponential distributions, as in Figure 2.3. For the CC calculation, spike trains are convolved with a Gaussian waveform having a standard deviation σ as a free parameter. We used sigma $\sigma = 1$ms, 5ms and 33ms respectively. As before, the Z-score of CC was based on bootstrapping. AMD and CC results are equivalent for $\sigma = 1$ms. For larger σ, CC cannot capture the specific features of ISIs distributions, but behaves generally in a similar manner as AMD for increasing jitter width.

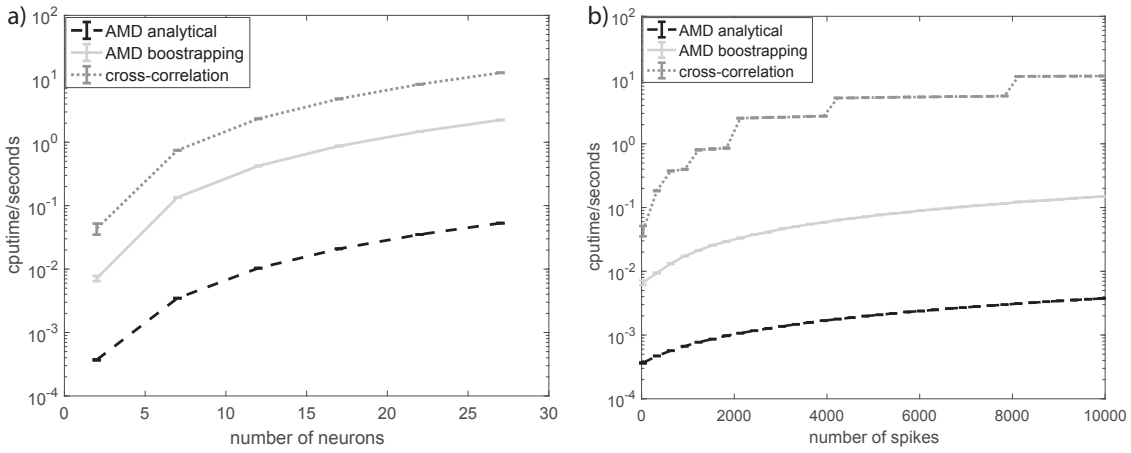

Figure 2.5: Comparison of computation speeds obtained for fast AMD, bootstrapped AMD, and bootstrapped CC. We measured the calculation time (recorded by CPU time from MATLAB) for three methods: CC, bootstrapped AMD and fast AMD. a) Calculation time for increasing the number of cells in the system. B) Calculation time for increasing the number of spikes in a two-cell system. Fast AMD is more than 20 times faster than bootstrapped AMD, and 200 times faster than CC calculation. For two-cell systems with different number of spikes (b), the advantage of fast AMD is more significant for larger spike trains, up to four orders of magnitude less than CC when the number of spikes is 10000. The sharp increases in CC computation time is most likely related to the memory allocation of the computer. The results for fast and bootstrapped AMD were averaged over 200 realizations, whereas 10 realizations were used for CC. The reported results are based on shuffling the ISIs 100 times for CC and bootstrapped AMD calculations.

the result of bidirectional AMD (Figure 2.6a) and unidirectional AMD (Figure 2.6b) estimation for coincident spike trains. As expected, bidirectional AMD reports highly significant temporal relations between the two trains whereas the unidirectional AMD estimation reports lack of causality (i.e., the significance is lower that one standard deviation). Figure 2.6c and d depict similar calculations for causally related spike trains. Here both measures report high temporal coincidence, however unidirectional AMD provides additional information about causal relationships.

2.3.1.3 Functional stability between functional connectivity matrices (FCMs)

We sought to determine how functional stability between FCMs can capture the similarity between different functional connectivity patterns in the network. Changing functional connectivity patterns are constructed by jittering five copies of a master spike train. For increasing jitter amplitude, all spike trains become increasingly de-correlated, resulting in different functional connectivity patterns. The FCM is first calculated using the fast AMD metric for the five spike trains. Then, the stability between FCMs for different realizations of the spike trains having various jitter width is determined (Methods 1.3). Figure 2.7 shows the functional stability as a function of jitter of the compared spike trains. For small jitter, the FCMs yield stability values close to one, indicating high similarity between the FCMs. On the other hand, when a small jitter FCM is compared to a high jitter FCM, similarity rapidly declines to negative values. This is due to switching from a well-defined network structure to a random one. Finally, when two largely random states are compared (i.e. both FCMs have high jitter and are de-correlated) the stability value hovers around 0.2. Taken together, these results indicate that functional stability reasonably quantifies the similarity between functional connectivity in the network.

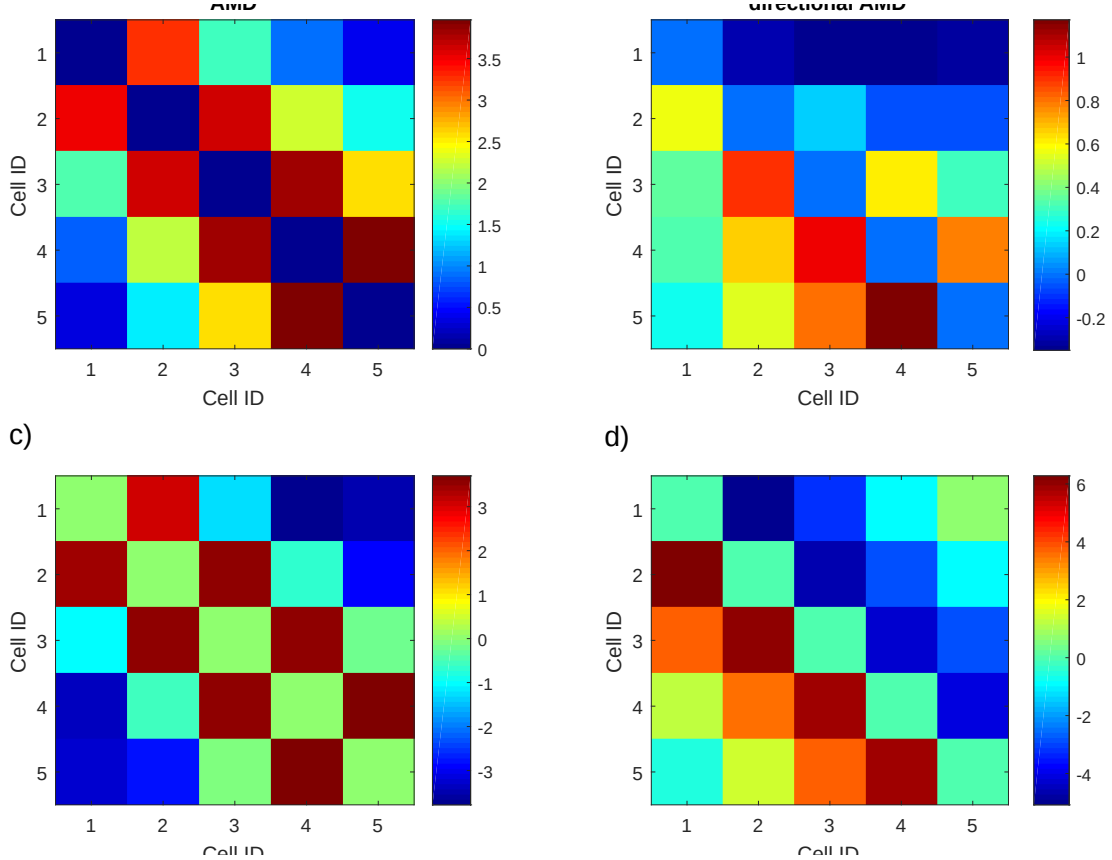

Figure 2.6: Bidirectional AMD and unidirectional AMD FCMs. An example of functional connectivity matrices (FCMs) calculated using two AMD methods for coincidence (a, b; bidirectional time lags taken into account) and causality (c, d; unidirectional time-lags taken into account) of functional connectivity (FC) patterns. Color represents the significance of fast AMD. In the case of coincidence, the FCM calculated by bidirectional AMD is almost symmetric and captures the functionally connected neurons (a), but unidirectional AMD does not (b); conversely in the causality case, the anti-symmetric FC matrix given by unidirectional AMD indicates the causal relationship (d), while bidirectional AMD does not differentiate from the coincidence case (c). The results were averaged over 100 realizations.

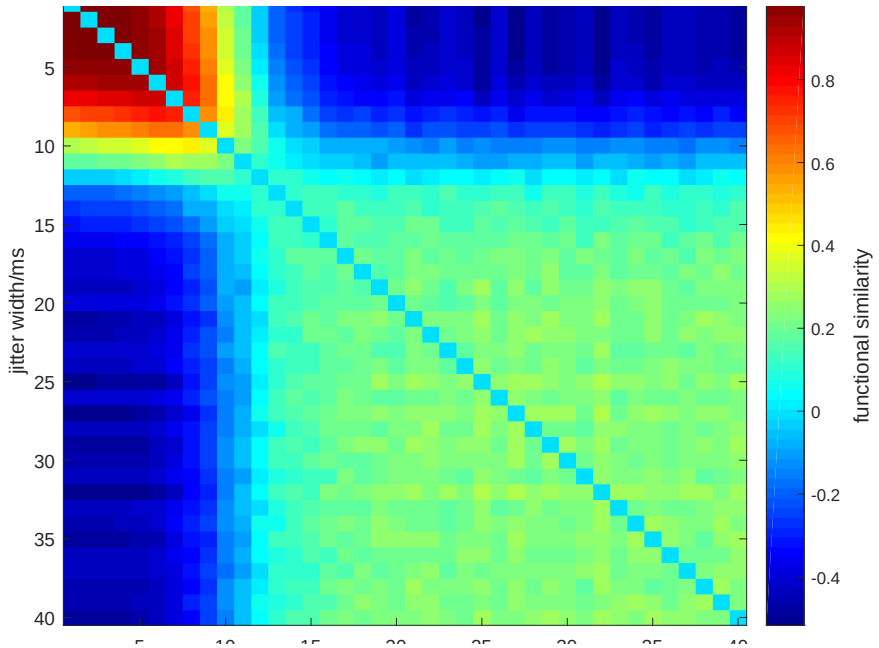

Figure 2.7: Similarity between FC patterns. A five-cell system is simulated, where the other four spike trains were jittered from the master train with same jitter width. Each train contains 30 spikes and time recording is set arbitrarily to 1 second. After calculating the functional connectivity matrix (FCM) for each jitter width, the similarity between each pair of FCMs is measured. The result is averaged over 100 realizations. Similarity is high when both jitter widths are small as the AMD values are small for both cases. There is a transition to negative values as one of the jitter widths gets significantly larger. For the pair of FCMs, both with high-valued jitter width, FC patterns are relatively random and similarity is low (0.2).

2.3.1.4 Functional Stability Matrix (FSM) and FuNS as a monitor of changes in functional connectivity patterns

Following the data generating procedure used in Figure 2.8, a five cell system is simulated to demonstrate the applicability of the Functional Stability Matrix (FSM) (Figure 2.8) in monitoring changes in dynamical network states over time. A bidirectional jitter with a width of 8ms is applied during the first and last 7 seconds of the spike train, while a bidirectional jitter of width 15ms (Figure 2.8a and c) or unidirectional jitter of width 8ms (Figure 2.8b and d) is applied during the middle 7 seconds. After segmenting the time series into 21 bins of equal size and calculating the 5-by-5 FCMs using the fast AMD algorithm, the FSM is obtained by calculating the functional stability between each pair of FCMs (Figure 2.8a and b). For both cases, significantly positive stability values in region I and III and low values in region IV indicate the temporal relationship between different functional connectivity patterns in the network. Importantly, region V in both cases demonstrates that the functional connectivity returns to the same pattern observed in the first 7s, subsequent to the changes occurring during the 8-14s time window. In the bidirectional case, the network loses stability during the middle 7s in region II (Figure 2.8a), while in unidirectional case region II (Figure 2.8b), due to the corresponding unidirectional shifts, the stability between FCMs attains a high value. Hence, FSM gives effective information to keep track of the similarity in functional connectivity patterns in the network at any time point. Figure 2.8c and d illustrate the functional stability trace over time, with the red line indicating FuNS, i.e. the mean of the stability values (0.4362 for bidirectional and 0.7720 for unidirectional). As expected, the minimum similarity in both cases happens at the point when FC changes, at the end of 7s and 14s, respectively. These results thus give a reliable way to track functional network changes in time, which may be due to cognitive processing, for example.

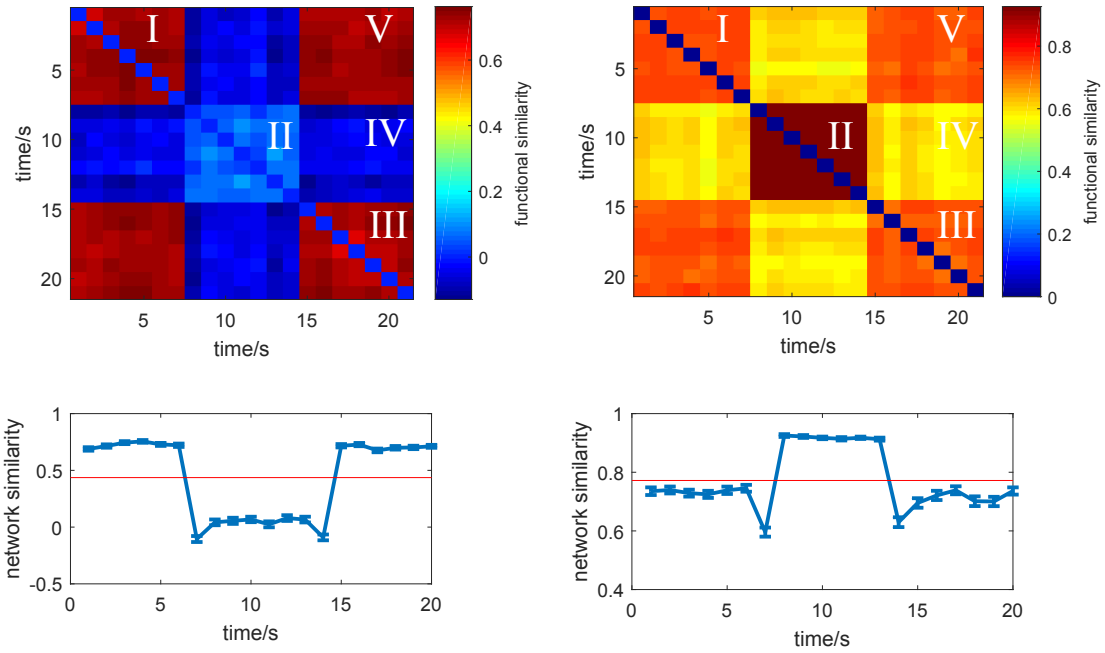

Figure 2.8: Functional Similarity Matrix (FSM) and similarity trace over time. Simulation of temporal changes in spike relationships between five neurons. The spike trains are jittered bidirectionally with a jitter width of 8ms from the master train during the first and last 7 seconds of the spike train. During the middle 7 seconds, jitter was bidirectional with width 15ms (a,c) and unidirectional with width 8ms (b,d), respectively. The spike trains were binned into 21 time windows and a five by five functional connectivity matrix (FCM) was calculated by bidirectional AMD for each window. (a,b) Similarity value between each pair of FCMs. FCMs originating from spike trains having common properties show high similarity (c,d). Similarity trace over time, within which only FCMs in adjacent time windows are compared. Red line indicates the functional network stability (FuNS), the average of the similarity trace values.

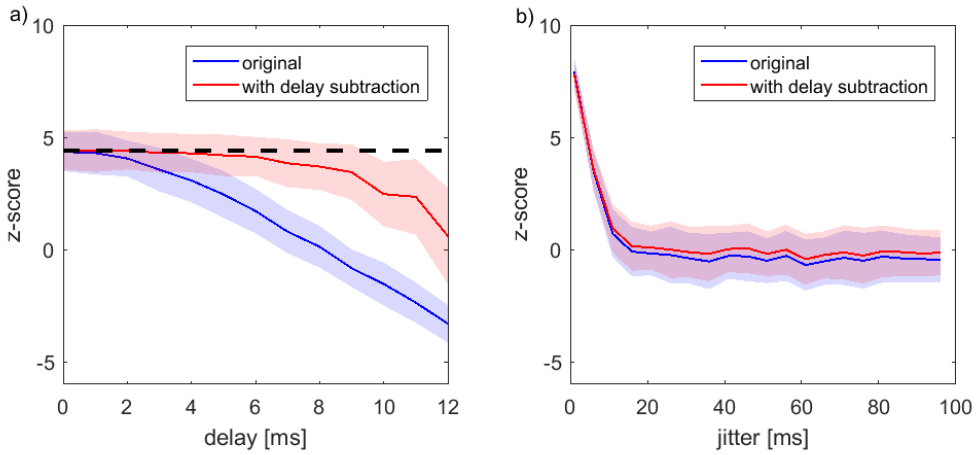

Figure 2.9: Fast AMD can be adjusted to account for time delays. A copy of the original random spike train having Gaussian ISIs is jittered with a jitter width of 5ms and then is shifted by variable time-delay. a) The FC between two trains is estimated by fast AMD (blue trace). Next the second train is shifted back by the amount of delay that is estimated by fast AMD algorithm, and FC is re-calculated (red trace). The black dashed line shows the FC for non-delayed spike times. b) The same analysis is applied to spike trains with no delay, and the FCs show no significant differences. The results were averaged over 100 realizations.

2.3.1.5 Estimation of fast AMD for functional connectivity for mutually delayed spike trains

We tested the performance of fast AMD on spike trains with applied time delay (Figure 2.9). Two random spike trains with Gaussian ISIs are generated with a jitter width of 5ms. Time delay is added to the second train by shifting each spike time by a constant value. In Figure 2.9a, the FC and standard deviation between two trains are estimated by fast AMD for different time delays. Around a delay of 7.5ms, FC is around 0 due to the fact that the second train is shifted to one quarter of the average ISI (33ms). FC values become negative with the increase of the delay time, indicating an anti-correlation between two trains.

Next, fast AMD is utilized to detect the delay and to recover the original, non-delayed z-score. The estimated delay time (DT) from S_i to S_j, as given by fast AMD,

is defined as $DT_{ij} = \frac{1}{N_j} \sum_k \left(t_k^j - {t'_k}^i \right)$, where t_k^j is the temporal value of the k$^{\text{th}}$ spike in S_j and ${t'_k}^i$ refers to the temporal value of the nearest event to t_k^j in S_i. Then, S_j is shifted by $-DT_{12}$ and FC is re-calculated using fast AMD. The red line on Fig 9a depicts the FC values after the shift, and as a function of original delay time. Fast AMD reliably detects the delay and restores FCs back to the level of no delay (indicated by the black dash line). As a comparison, we also calculated the FC with and without subtracting the estimated DT for non-delayed spike trains (Figure 2.9b). There is no significant difference after subtracting DT, indicating that no spurious correlations were introduced for non-delayed spike trains.

To further test performance of the tools on the delayed spike trains, we calculated FuNS for a 5-cell system with jittering and applied variable time-delay (Figure 2.10); with mean delay time in the system denoted on the y-axis. The total recording time duration was 10s. FuNS was calculated from 10 equal length time bins. The top row indicates the system without delay. When the system is strongly connected (i.e., a small jitter width), FuNS is highly robust to delays, reporting nearly identical values as the case without delay. For bigger jitter width, as expected, FuNS is low when the delay time is around one quarter of the average ISI, i.e. when the FC between spike trains loses significance. Thus, even though FC values can be affected by delays, FuNS can still quantify the stability level of the system effectively.

2.3.2 Effects of localized network heterogeneity in model networks

2.3.2.1 Characterizing dynamics and connectivity of integrate-and-fire networks

Using the statistical tools introduced above, we investigate networks of leaky integrate-and-fire neurons for dynamic stability. The focus here is to establish how the new metrics help to elucidate network connectivity structure, as well as potential changes in network dynamics, due to the formation of localized network het-

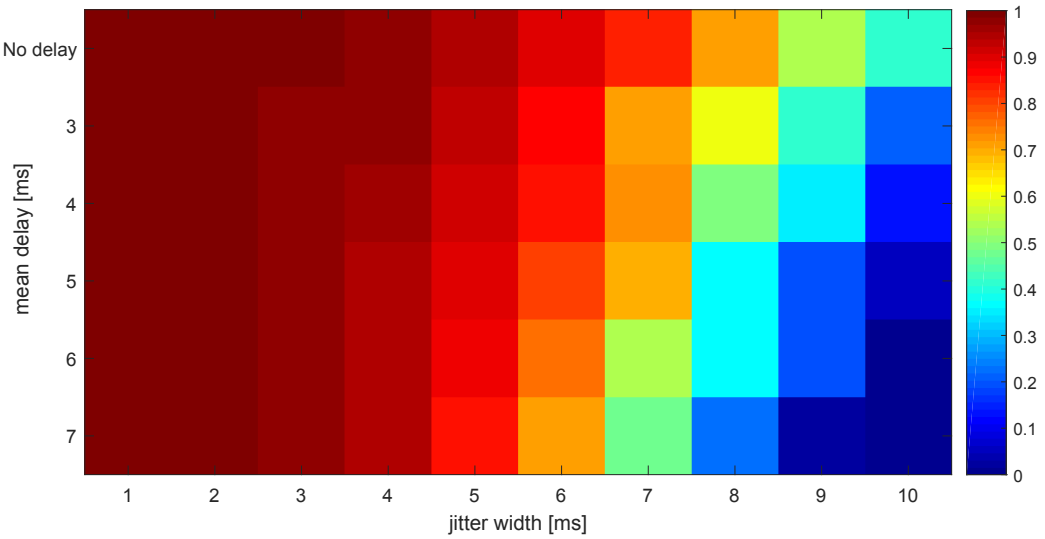

Figure 2.10: Functional Network Stability (FuNS) of the delayed dataset. A 5-cell system is simulated by adding jitter and time delay to spike trains to randomly generate spike train using Gaussian distribution of ISIs. The color scale represents FuNS calculated after binning the data into 10 one-second time windows. A control realization, where no delay is added to the spike trains, is indicated by the top row. The results were averaged over 10 simulations. FuNS gives robust results despite the delay.

erogeneities. As noted previously, these heterogeneities represent the formation of localized cognitive representations (e.g. memories) within the network.

2.3.2.2 Identification of direct structural connections within the network

We first constructed sparsely connected, excitatory only networks to investigate whether, and for what ranges of connectivity parameters, is it possible to statistically separate sets of neurons with direct structural connectivity from those who lack direct connections. This corresponds to adjacency matrix entries of 1 and 0, respectively. We use the bidirectional, fast AMD metric to measure the functional connectivity between pairs of neurons that share direct structural connections and those that do not. The distribution of FC values are then characterized (i.e. their mean and variance are calculated) for the two populations and we subsequently calculate the statistical separation between groups in terms of a Z-score: $Z_s = (\mu_{wc} - \mu_{nc}) \left(\frac{\sigma_{wc}^2}{N} + \frac{\sigma_{nc}^2}{N} \right)^{-\frac{1}{2}}$, where $_{\text{wc}}$, $_{\text{wc}}$ and $_{\text{nc}}$, $_{\text{nc}}$ represent mean and standard deviation of the distributions of functional connectivity values for directly coupled pairs and non-coupled pairs, respectively. Figure 2.11 shows the Z-Score comparison between these two populations (Figure 2.11a). Each colored panel represents the statistical separation of the two populations as a function of network topology for increasing synaptic connectivity. The obtained results indicate that there is a well-defined parameter region where the two populations can be separated with a large degree of accuracy. As expected, weak network connectivity prohibits this separation (Figure 2.11b). Also, the statistical significance is lower in networks deviating from local to random connectivity (Figure 2.11b-f). Importantly, significance between the groups is seen even under very strong connectivity, though eventually the response is saturated and no new network parameter values result in an increase in significance (Figure 2.11e and f).

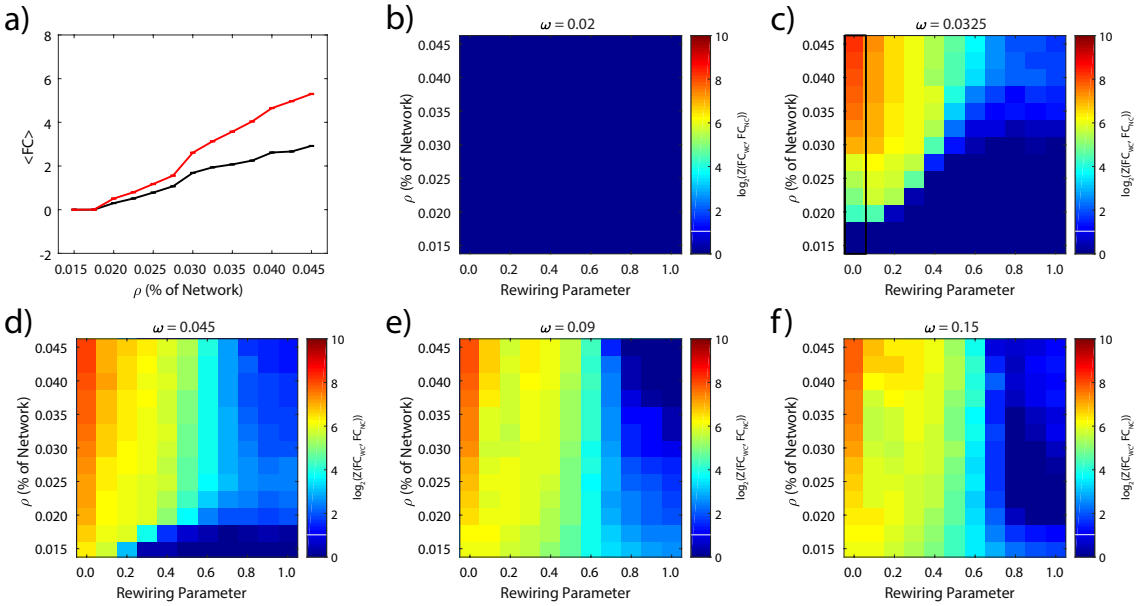

Figure 2.11: Z-Score significance between functional connectivity matrices as a function of network topology. Functional connectivity matrices (FCMs) were parsed based on the existence or non-existence of synaptic connections between neurons and fast AMD results for these two groups were generated. a) Mean grouped-averaged functional connectivity as a function of connectivity density for a connection strength of $\omega = 0.0325$ and rewiring parameter equal to 0 (red traces: directly connected neurons; black traces: unconnected neurons). Error bars represent standard error of the mean. Lack of variation in network structure (i.e. there is no rewiring of local connections) results in uniformly small standard error; the network for each simulation is exactly the same and so responds to random input in nearly the same manner. b-f) Color images indicate the logarithmically scaled significance, with warmer colors indicating a greater significance, with the white bands indicating the level above which the Z-score is significant (consistent with two standard deviations from the mean). As synaptic connectivity strength ω increases from very low values (b) through moderate values (c) to higher values (d), significance increases between the parsed groups over an increasingly large topological parameter region. As ω further increases, more than half of the parameter region has a significant separation between groups (e) but saturates, admitting no additional significant parameters (f). The black box in panel (c) indicates the range of data used to generate panel (a). All results were averaged over five trials.

2.3.2.3 Changes in functional connectivity and stability of the network with introduction of network heterogeneity

It is still not clear how localized changes in network structure (i.e. inclusion of a network heterogeneity) affect network-wide dynamics. To address this, functional connectivity and the subsequent stability of these matrices is measured between the neurons that are not included in the heterogeneity, using the fast AMD method. Simulations are cut into two parts and we subsequently measure both the change in FC as well as FuNS, both given as a function of network topology and connectivity density (Figure 2.12). Figure 2.12a depicts FuNS in the same network before the heterogeneity is introduced (black line) and after its introduction (red line) as a function of the connection rewiring parameter. Significant changes in network stability are observed for localized network topologies with significance decreasing as the topologies become more random. Figure 2.12b depicts changes of network stability upon the introduction of a heterogeneity, as a function of both connectivity density and network topology, and compares it to changes in mean value of FC, averaged over all pairwise indices of the corresponding FCM, for the network (Figure 2.12c). We note that while FuNS changes are quite significant for a wide parameter range (up to Z-score of 64, noting the logarithmic scale), the changes in mean functional connectivity are quite insignificant and provide a less clear picture of how the FCM itself changes. This leads us to conclude that measuring the changes of FuNS is a more tenable indicator of global change in network dynamics in response to introduction of network heterogeneity compared to FC.

2.3.2.4 FuNS as a global measure of structural network changes

We have shown above that FuNS is sensitive to the introduction of a discrete network heterogeneity. Thus, it allows the identification of the existence of structural network changes without the requirement of measuring specific cells that participate

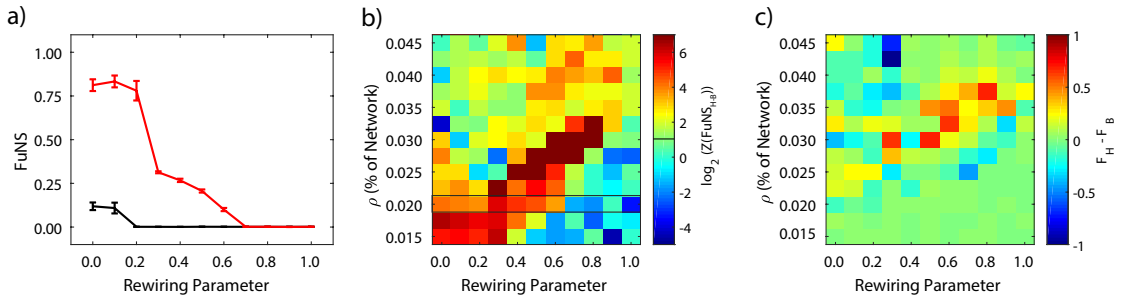

Figure 2.12: Functional Network Stability detects dynamic changes due to synaptic heterogeneities over a large topological parameter region. a) FuNS as a function of connection rewiring parameter for networks before (black trace) and after (red trace) introduction of a synaptic heterogeneity. Synaptic heterogeneities are defined as spatial regions within the network, where connections between neurons only in the region were appointed a greater synaptic connectivity compared to the rest of the network. Error bars indicate the standard error of the mean. b) Z-score of FuNS as a function of connection density ρ and rewiring parameter, scaled using a logarithm of base two. Warmer (cooler) colors denote an increase (loss or no change) in stability due to the introduction of a synaptic heterogeneity. The black bar on the color scale indicates the minimum value needed to be considered significant. The black box in the main panel shows the parameter region used to generate FuNS curves in the left panel. c) Difference in average FC over the entire FCM as a function of ρ and rewiring parameter is less robust than analyzing FuNS. All results shown are for a synaptic coupling strength of A = 0.03, averaged over five trials.

in that change. This is of paramount importance in the situation when the experimental measurement is critically under-sampled and there is no way to identify either the specific neurons participating in the structural network reorganization or the anatomical network structure. To quantify the long-range effects of synaptic heterogeneities, we set out to measure the synaptic distances from network heterogeneity where significant changes in network stability are observed.

Neurons are grouped depending on their mean synaptic distance from heterogeneity (Methods 2.2). Functional connectivity matrices for each group of cells is calculated separately, whereupon we determine the mean change in FuNS within

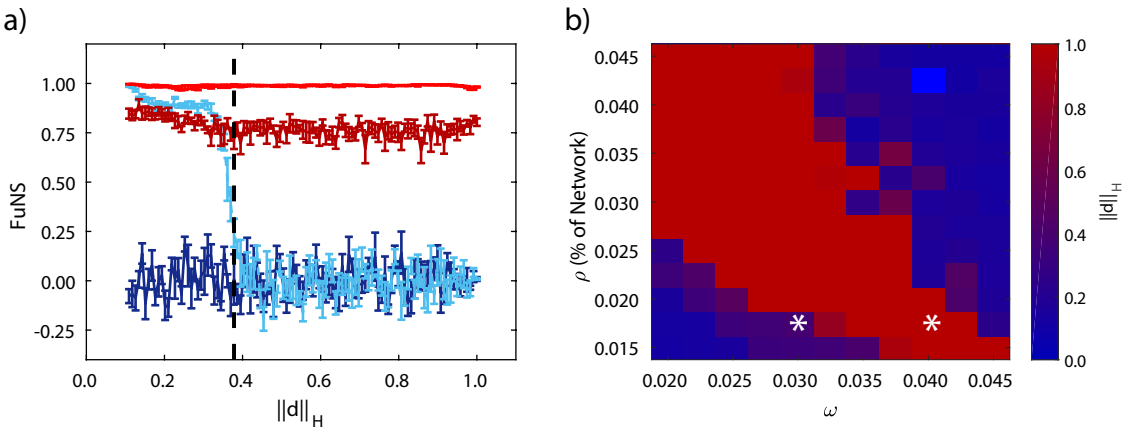

Figure 2.13: Local synaptic heterogeneities globally increase Functional Network Stability (FuNS). a) Example FuNS traces as a function of normalized synaptic distance from the heterogeneity for networks before (darker colors) and after (lighter colors) introduction of a synaptic heterogeneity. Some values of the simulation parameters result in a distance dependent decrease or no change in FuNS Z-scores (blue traces), while others result in consistent, network-wide significance (red traces). The black, dashed line indicates the normalized distance where FuNS loses significance in the example case shown. Error bars indicate standard error of the mean. b) Normalized distance from the heterogeneity where FuNS significance is lost. Values of one indicate that the global network observes an increase in FuNS due to a localized synaptic heterogeneity. All results averaged over five trials.

each group due to introduction of heterogeneity (Figure 2.13). Figure 2.13a shows an example of change in FuNS as a function of mean distance from heterogeneity, normalized by the maximum possible distance to the heterogeneity. Some network parameters results in a persistently significant separation of FuNS at long distances from the heterogeneity, while other parameters result in a rapid decline of FuNS away from the heterogeneity. Thus, the Z-score of FuNS is calculated between networks with and without synaptic heterogeneity at each synaptic distance in order to determine the normalized distance where significance is lost. Figure 2.13b depicts the normalized mean distance from the heterogeneity at which the results become insignificant, as a function of connection density and strength. Here, a value of one corresponds to the situation where we can detect changes in FuNS throughout entire network. We observe that localized heterogeneity has global dynamical effects on the system under a large array of network topologies, giving credence to the notion of dynamical attractors in neural networks.

2.3.2.5 FuNS sensitivity to structural heterogeneity in mixed excitatory and inhibitory networks

Finally, we measure changes in FuNS in response to introduction of network heterogeneity in mixed inhibitory and excitatory networks. Specifically, FuNS is measured as a function of the ratio of total excitation and inhibition generated by neurons in the network (i.e. E/I ratio; Methods 2.1). Generally, we observe that for low values of E/I ratio the reported FuNS is low regardless of the presence of a heterogeneity and, at the same time, a high E/I ratio saturates FuNS in both cases (Figure 2.14). The greatest response of the networks, in terms of stabilizing dynamics in presence of heterogeneity, is near a balance between excitation and inhibition, i.e. E/I 1 (Figure 2.14b). Thus, only near such an E/I balance can the dynamics of the network respond in a distributed manner to the introduction of heterogeneity. This provides another

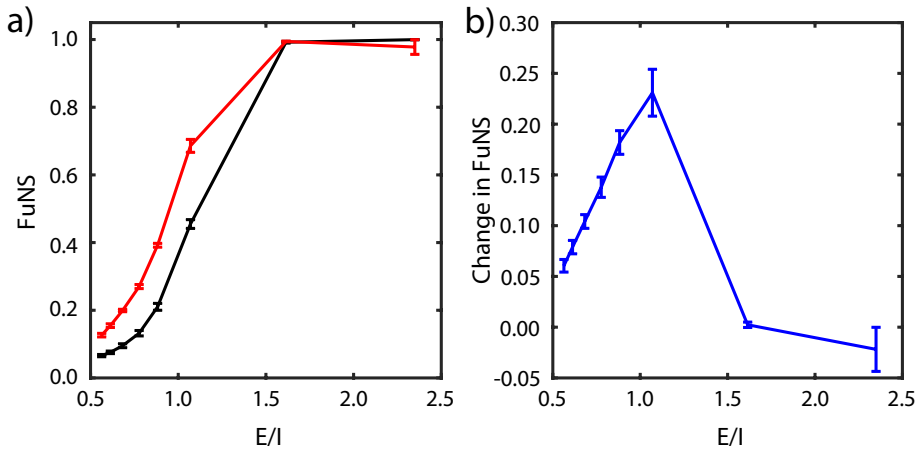

Figure 2.14: Introduction of synaptic heterogeneities maximize increased Functional Network Stability near a balance between excitation and inhibition. a) FuNS as a function of the ratio between excitation and inhibition. Introduction of synaptic heterogeneities (red traces) increases stability over networks missing a synaptic heterogeneity (black traces). b) Difference in FuNS between networks containing and not-containing synaptic heterogeneities. All error bars indicate the standard deviation of the mean, taken over five trials.

piece of evidence that mixed networks near E/I balance increase their dynamic range in response to even localized structural network changes, in agreement with previous studies (*Poil et al.*, 2012; *Gautam et al.*, 2015).

We further compare FCM and FuNS measurements between the fast AMD approach and the CC approach (Figure 2.15) at the point where FuNS observes a maximum increase in Figure 2.14b, i.e. E/I 1. As expected, the FCM analysis for both methods is very similar and, indeed, does not show a significant difference between networks with and without a synaptic heterogeneity (Figures 15a and 15b). However, we observe a significant increase in FuNS for the fast AMD method (Figure 2.15d) but not for the CC method (Figure 2.15c), assuming a non-normalized Gaussian distribution for both. Thus, though the resulting FCMs are similar, FuNS more accurately picks up on discrete changes in functional network topologies generated using AMD compared to cross-correlation.

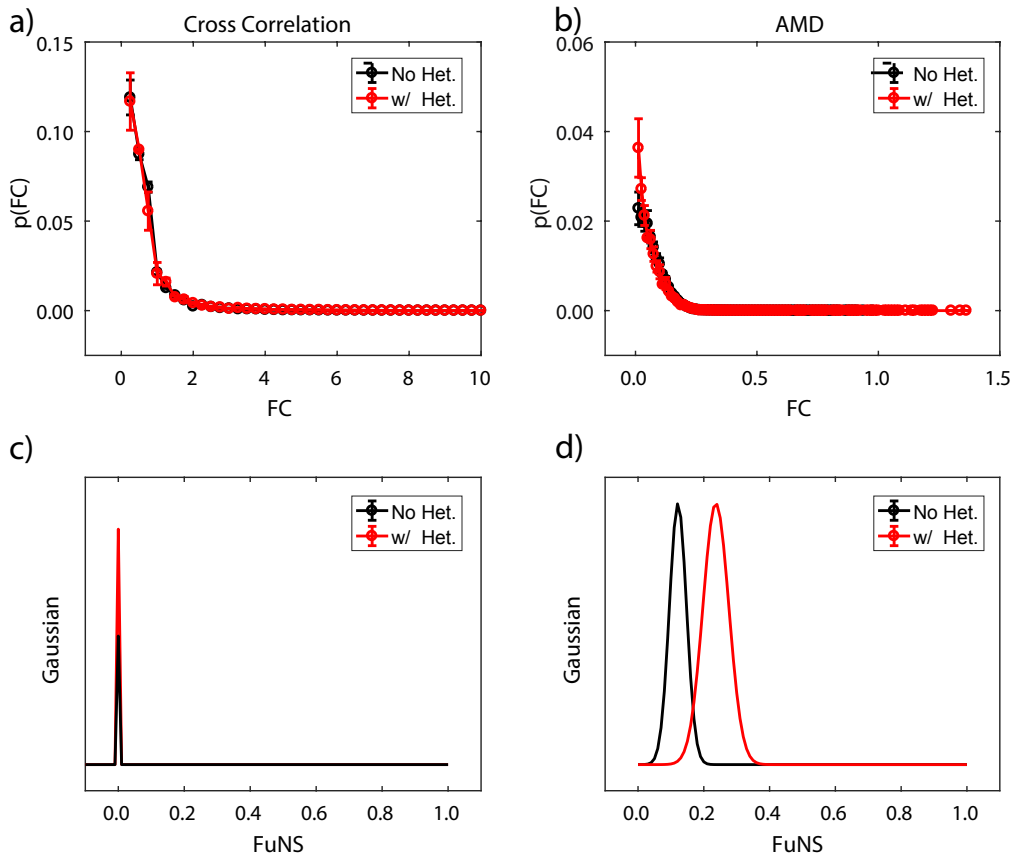

Figure 2.15: Comparing FC and FuNS between AMD and CC near the E/I Balance. The probability of observing a mean FC value was measured for functional structures from both CC (a) and AMD (b) derived methods, only over the excitatory neurons in the mixed networks, before (black) and after (red) adding a network heterogeneity. The distributions were not significantly different, within a 5% confidence interval (K-S test; CC: p = 0.83, AMD: p=0.54). Similarly, non-normalized Gaussian distributions of FuNS were constructed for CC (c) and AMD (d) before (black) and after (red) introduction of a synaptic heterogeneity. Calculating FuNS for AMD yielded significantly different distributions whereas FuNS for CC did not, within a 5% confidence interval (K-S test; CC: p = 0.09, AMD: p = $7\times10+-9$). Error bars represent standard error of the mean, whereas Gaussian widths stem from the standard deviation. Averaged over 5 trials.

2.3.3 FuNS applied to in vivo data

Finally, we wanted to know whether functional connectivity and stability changes could be detected following network reorganization in vivo (Figure 2.16). We hypothesize that synaptic plasticity in hippocampal area CA1 following single-trial contextual fear conditioning (CFC) (*Tronson et al.*, 2009) is a plausible biological model to investigate how rapid structural network changes underlying memory formation affects network dynamics. CA1 network activity is necessary for fear memory consolidation in the hours following CFC (*Daumas et al.*, 2005). For this reason, we recorded the same population of CA1 neurons from C57BL/6J mice over a 24-h baseline and for 24 h following CFC (placement into a novel environmental context, followed 2.5 min later by a 0.75 mA foot shock) to determine how functional network dynamics are affected by de novo memory formation. CFC affects many aspects of CA1 network dynamics; for a detailed description of the obtained results, please refer to *Ognjanovski et al.* (2014, 2017).

The results presented here focus on comparing performance of the metrics (fast AMD and CC, both together with FuNS assessment) for the case when mouse was subjected to successful memory consolidation (success was determined by observing behavioral changes 24 hours after training). First, the 6-hour baseline and 6-hour post stimulation are divided into 1-minute time windows, and FCMs are calculated in each bin, which are further used to calculate FSM. Figure 2.16 shows comparisons of the distribution of functional connectivity values (Figures 16a and 16b) and stability values (Figures 16c and 16d). Comparing with CC, AMD is shown to be more sensitive to capture the change of functional connectivity and stability in the network during memory consolidation. Furthermore, the more significant shift of similarity distribution indicates that stability is a better measurement of the change in global network properties.

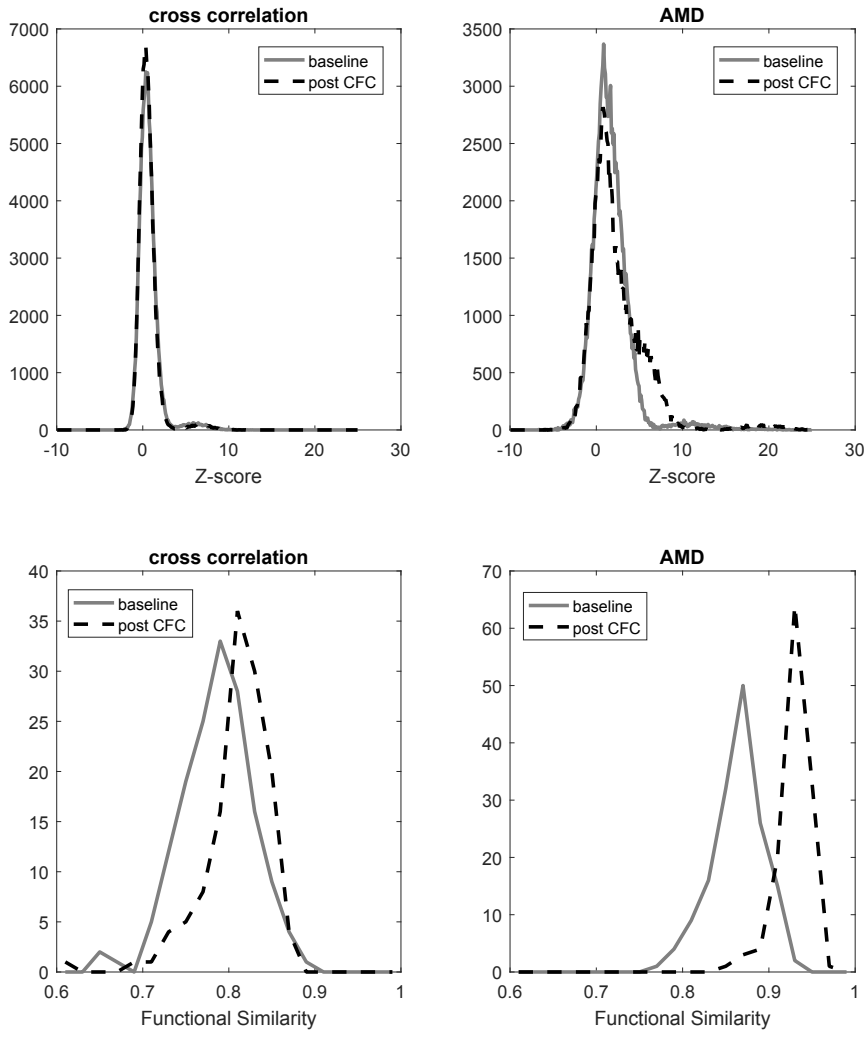

Figure 2.16: Application of AMD and FSM to in vivo mouse data. We extracted spike data from intervals of slow wave sleep across 6-hour recordings for both before (baseline) and after (post stimulation) the contextual fear conditioning. The spike trains were first divided into multiple one-minute bins, then the functional connectivity (FC) pattern for each bin is calculated by bidirectional AMD and CC. We compared the distribution of both FC values (a,b) and stability values (c,d). For FC values, the elements are extracted collectively from all the FCMs. The histogram shows us that AMD is able to capture the functional connectivity changes from baseline to post contextual fear conditioning more sensitively than CC. For stability values, the elements were extracted from the FSMs for baseline and post-stimulation respectively, and calculated as described in Results 1.4. We observe significant shift in stability for both CC and AMD calculation, however, AMD gives a more statistically significant separation between the two distributions.

2.4 Discussion

The advent of new recording techniques allowing for prolonged recordings from an increasing number of neurons in the brain drives the necessity to develop new analysis tools to meaningfully process data. Two underlying issues however need to be overcome. First, there is a severe under-sampling problem: how is it possible to identify universal properties of neuronal dynamics during information processing if the number of recorded cells remain tremendously small in comparison with number of cells participating in the computation? Second, and related to the first question, is how to characterize the data so that the (small) recorded population provides a representative picture of the dynamics of whole modality? Solutions to the latter attempt to bridge the timescales between neuronal activity and behavioral states which they encode, while prolonged recordings on freely behaving mice are now possible, they generate enormous data sets which need to be meaningfully processed in a finite amount of time.

In this paper we have addressed both of these problems - we have introduced a framework, based on the AMD between spikes in individual neurons' recorded spike trains, which allows for rapid assessment of network functional connectivity structure throughout extended time periods. We showed that we can extend the developed metrics so that we can rapidly estimate significance of functional connectivity between neuronal pairs, based on analysis of distribution of ISI intervals of the neurons in question, not only without loss of resolution, but often with improved sensitivity as compared to cross-correlation based methods. At the same time, rapid assessment of significance allows us to speed up functional connectivity reconstruction by a couple of orders of magnitude, primarily due to the fact that we can bypass typical bootstrapping methods without loss of accuracy (Results 1.1-1.5).

Further, we used this fast, AMD-based method to reconstruct instantaneous functional connectivity within the network and subsequently introduced Functional Net-

work Stability (FuNS), a measure that assesses the temporal stability of functional connectivity networks. We showed that FuNS is especially useful in detecting changes in network-wide dynamics due to discrete changes in network structural connectivity, referred to here as synaptic heterogeneities. Namely, we show that localized and relatively small heterogeneities can induce dynamical changes throughout the entire network, as is evidenced by high FuNS in neuronal groups distantly connected to the heterogeneity region (Figure 2.14). This in turn allows for robust detection of such changes experimentally, even in the conditions of severe under-sampling (*Skilling et al.*, 2017; *Ognjanovski et al.*, 2017). These results indicate that while reconstruction of functional connectivity between the recorded neurons may yield ambiguous results as the functional relation of the recorded cells to the computational task is unknown, the changes in the global dynamics of the representations is a more robust measure of local network changes in response to computational tasks. (Results 2.1-2.4) To better exemplify this point, we used both model simulations and in vivo experimental recordings to show that discrete changes to network structure may yield ambiguous results in terms of reconstruction of detailed changes in functional network connectivity, but at the same time show robust stabilization of dynamical network representations (Results 3.1).

Finally, we investigate whether observed stabilization of dynamical network representations can inform us about universal network properties that are underlying the computation. Here, we show that in mixed excitatory-inhibitory networks, the highest sensitivity (in terms of changes in global network representations) to introduction of localized heterogeneity is achieved near a balance between excitation and inhibition (E/I balance; Results 2.5). This result is in line with other existing results which have shown that E/I balance emerges naturally in neural networks (Vreeswijk and Sompolinsky, 1996) and that neurons operating in networks near E/I balance exhibit faster linear responses to stimulation, and greater dynamic range (*van Vreeswijk and*

Sompolinsky, 1996). Recent findings have also shown that E/I balance is required for heightened neuronal selectivity (*Rubin et al.*, 2017).

Altogether, we believe that the introduced framework for rapid calculation of functional network connectivity allows for robust analysis of multiunit recordings. Numerous linear and nonlinear, methods have been developed over the last decade to reconstruct and characterize functional network connectivity. We have earlier compared the performance of functional grouping based on AMD assessment to some of these methods (*Feldt et al.*, 2009). Many of the developed tools require assessment of functional adjacency matrix. We believe that the algorithm proposed here provides a robust alternative for the commonly used cross-correlation method. Further we believe that fast AMD together with evaluation of FuNS helps to overcome two major constraints in neuroscience: undersampling and the difficulty of bridging diverse timescales of neuronal dynamics and cognition. We believe that this framework will be widely applicable to numerous problems in systems neuroscience.

CHAPTER III

Network and Cellular Mechanisms Underlying Heterogeneous Excitatory/Inhibitory Balanced States

3.1 Introduction

Since the first proposal of the idea that excitatory/inhibitory (E/I) balance emerges within brain networks (*van Vreeswijk and Sompolinsky*, 1996), a large body of theoretical and experimental work has focused on clarifying its regulation and possible role in maintaining desired spatio-temporal activity states (*Denève and Machens*, 2016). Co-occurring E/I responses have been observed for many modalities, e.g., in auditory cortex (*Wehr and Zador*, 2003; *D'Amour and RC.*, 2015), visual cortex (*Tan et al.*, 2013; *Liu et al.*, 2009), and olfactory cortex (*Poo and Isaacson*, 2009; *Stettler and Axel*, 2009). Besides activity evoked by stimuli, balanced excitation and inhibition also appears to be present during spontaneous brain activity (*Graupner and AD.*, 2013; *Murphy and Miller*, 2009) and may play a critical role in generating certain brain rhythms (*Atallah and Scanziani*, 2009).

Despite these experimental findings, two important issues remain unresolved: 1) how does E/I balance contribute to regulate spatio-temporal patterning of neuronal microcircuit activity, and 2) what are the underlying mechanisms promoting E/I bal-

ance across brain networks. E/I input to neurons was initially proposed to balance only over long timescales, leading to the notion of loose E/I balance with specific statistics of the firing patterns (*Brunel*, 2000; *van Vreeswijk and Sompolinsky*, 1998; *Rudolph et al.*, 2007; *Salinas and P.*, 2000). This idea was challenged by experimental phenomena, such as efficient coding of irregular spiking, and the correlation of membrane potentials between neurons responding to similar stimuli (*Cohen and A.*, 2011; *Yu and Ferster*, 2010; *Gentet et al.*, 2010), which cannot be explained by loose interactions of E/I cells (*Denève and Machens*, 2016). More recent findings have demonstrated that inhibition can closely track excitation at a millisecond timescale, leaving a brief window of disinhibition for neurons to fire. This "tight balance" has been observed in brain regions such as somatosensory cortex (*Okun and Lampl*, 2008), hippocampus and piriform cortex, as well as in vitro (*Atallah and Scanziani*, 2009) and in computational simulations (*Renart*, 2010). Indeed, this disinhibition is now thought significant in learning and memory (*Letzkus et al.*, 2015). The interaction of recurrent inhibitory and excitatory circuits also regulates the occurrence of cortical up- and down-states (*Shu et al.*, 2003; *Haider et al.*, 2006), and it was shown that different levels of correlation between excitation and inhibition can emerge from the same neuronal circuitry, depending on the specific cortical state - with correlations observed to be lower during anesthesia than during states exhibiting up- and down-state activity (*Tan et al.*, 2013).

One roadblock to understanding the regulation and function of E/I balance is a lack of technical ability to experimentally quantify E/I ratios. It is impossible to simultaneously measure the excitatory and inhibitory post synaptic currents (EPSCs and IPSCs) at every neuron across a network. Several indirect experimental quantifications have been used (*Wehr and Zador*, 2003; *Monier et al.*, 2008; *Xue et al.*, 2014; *Tan et al.*, 2013; *Landau et al.*, 2016) and although each of these captures characteristics of E/I balance in some way, none of them quantifies all of the features

that simultaneously contribute to E/I balance. Further, such metrics can only infer E/I ratio from a selected subset of neurons, which may not accurately represent E/I ratios at the network level.

To investigate E/I balance in a network and its dynamical correlates, we use a computational model composed of biophysical neurons and quantify E/I ratio as the ratio between mean levels of total EPSC and IPSC across the network. By systematically varying parameters, we show that a network can homeostatically regulate E/I ratio over a wide range of E/I levels and reach asymptotic balance states after evolving for a period of time. These balanced states are generated by multiple, heterogeneous cellular and network mechanisms. We particularly analyze the multiple E=I balanced states to show that synaptic conductance levels, average firing rates and average membrane potential levels contribute to the E/I ratio in a distinct manner, thus defining different mechanisms governing E/I balance. These results demonstrate that E/I ratio states are not achieved by varying the excitation (or inhibition) in the network monotonically, but instead can be achieved by different combinations in a non-monotonic way, and result in a diverse range of network dynamics.

3.2 Methods

3.2.1 Neuron Model

3.2.1.1 Modified Hodgkin-Huxley Model

The model networks in these studies consist of biophysical Hodgkin-Huxley-type (*Stiefel et al.*, 2009) single compartment neurons with the following current balance equation for the i-th neuron:

$$C\frac{dV_i}{dt} = -g_{Na}m_{\infty}^{3}\left(V_i\right)h\left(V_i - V_{Na}\right) - g_{Kdr}n^{4}\left(V_i - V_K\right) - g_L\left(V_i - V_L\right) + I_i^{drive} - I_i^{syn} \tag{3.1}$$

Each neuron receives an external applied current, I_i^{drive}, consisting of both a constant sub-threshold current and external noisy stimuli. To simulate neuronal heterogeneity, each cell receives a random subthreshold current chosen from a Gaussian distribution centered around -0.2 $\mu A/cm^2$ with a deviation of 0.1 $\mu A/cm^2$. External noise is modeled by the delivery of brief (0.05ms), square, 30 $\mu A/cm^2$ current pulses, at intervals dictated by a Poisson process (with an average frequency of 40 Hz). The kinetics of neuronal Na^+ conductance are governed by the steady state activation function

$$m_\infty(V) = \left\{1 + exp\left[\frac{-V - 30.0}{9.5}\right]\right\}^{-1} \tag{3.2}$$

and the inactivation gating equation

$$\frac{dh}{dt} = \left(h_\infty(V) - h\right)/\tau_h(V) \tag{3.3a}$$

$$h_\infty(V) = \left\{1 + exp\left[\frac{V + 53.0}{7.0}\right]\right\}^{-1} \tag{3.3b}$$

$$\tau_h(V) = 0.37 + 2.78\left\{1 + exp\left[\frac{V + 40.5}{6.0}\right]\right\}^{-1} \tag{3.3c}$$

Neuronal K^+ conductance is gated by the variable n, which evolves in time according to the equation

$$\frac{dn}{dt} = \left(n_\infty(V) - n\right)/\tau_n(V) \tag{3.4a}$$

$$n_\infty(V) = \left\{1 + exp\left[\frac{-V - 30.0}{10.0}\right]\right\}^{-1} \tag{3.4b}$$

$$\tau_n(V) = 0.37 + 1.85\left\{1 + exp\left[\frac{V + 27.0}{15.0}\right]\right\}^{-1} \tag{3.4c}$$

In addition, the leak conductance is given by g_L=0.02mS/cm^2. Other parameters are set to g_{Na}=24.0 mS/cm^2, g_{Kdr}=3.0 mS/cm^2, V_{Na}=55.0mV, V_K=-90.0mV, and

V_L=-60.0mV. This model exhibits Type 1 dynamics in terms of phase response curves and current-frequency relation (Smeal *et al.*, 2010).

3.2.1.2 Wang-Buzsaki Model

To exclude the possibility that the results are due to the unique properties of the modified Hodigkin-Huxley model we described above, we performed the same simulations with Wang-Buzaki Model (WBM) (*Wang and G.*, 1996), which also exhibits Type 1 excitability. Each neuron is described in the same form of three differential equations as above, with different definitions of some parameters. The master differential equation is:

$$C\frac{dV_i}{dt} = -g_{Na}m_\infty^3\left(V_i\right)h\left(V_i - V_{Na}\right) - g_{Kdr}n^4\left(V_i - V_K\right) - g_L\left(V_i - V_L\right) + I_i^{drive} - I_i^{syn} \tag{3.5}$$

with $m_\infty = \frac{\alpha_m(V)}{\alpha_m(V)+\beta_m(V)}$, with $\alpha_m\left(V\right) = 0.1\frac{V+35}{1-exp\left[-\frac{V+35}{10}\right]}$ and $\beta_m\left(V\right) = 4exp\left[-\frac{u+60}{18}\right]$. The gating equations are:

$$\frac{dh}{dt} = \left(h_\infty\left(V\right) - h\right)/\tau_h\left(V\right) \tag{3.6}$$

with $h_\infty\left(V\right) = \frac{\alpha_h(V)}{\alpha_h(V)+\beta_h(V)}$, $\tau_h\left(V\right) = \frac{0.2}{\alpha_h(V)+\beta_h(V)}$, where $\alpha_h\left(V\right) = 0.07exp\left[\frac{-V-58.0}{20}\right]$, $\beta_h\left(V\right) = \{1 + exp\left[\frac{-V-28}{10}\right]\}^{-1}$ and

$$\frac{dn}{dt} = \left(n_\infty\left(V\right) - n\right)/\tau_n\left(V\right) \tag{3.7}$$

with $n_\infty\left(V\right) = \frac{\alpha_n(V)}{\alpha_n(V)+\beta_n(V)}$, $\tau_n\left(V\right) = \frac{0.2}{\alpha_n(V)+\beta_n(V)}$, where $\alpha_n\left(V\right) = 0.01\frac{V+34}{1-exp\left[-\frac{V+34}{10}\right]}$, $\beta_n\left(V\right) = 0.125exp\left[-\frac{V+44}{80}\right]$. Other parameters are $C = 1\mu F/cm^2$, $I_i^{drive} = 0.145\mu A$, g_{Na}=35.0 mS/cm^2, g_{Kdr}=9.0 mS/cm^2, V_{Na}=55.0mV, V_K=-90.0mV, and V_L=-65.0mV. g_L=0.1mS/cm^2.

3.2.2 Network simulation

Networks contain 500 neurons, 250 with excitatory (E) synapses and 250 with inhibitory (I) synapses. While this ratio is not physiological we found that our results do not depend on it as the ratio of cells is offset by the number of connections originating from the given cell type. For the main results, neurons were randomly connected with connectivity probability 3% .

In separate simulations, when investigating the role of network topology on the evolution of E/I balance, we applied the Watts-Strogatz framework to obtain Small World network connectivity (Watts & Strogatz, 1998) to a two-layer network composed of interconnected 1-D rings of excitatory (E) neurons and inhibitory (I) neurons. For this network configuration, each neuron is initially connected to its 6 nearest neighbors in each layer. Connectivity structure is varied by rewiring each E and I connection to a randomly chosen post-synaptic target neuron with probability given by the rewiring parameter $\mathrm{rp_E}$ and $\mathrm{rp_I}$, respectively. In this way we can easily control the network topology with more local excitation or inhibition depending on specific values of $\mathrm{rp_E}$ and $\mathrm{rp_I}$.

Synaptic current transmitted from neuron j to neuron i at time t is given by

$$I_{ij}^{syn} = wexp\left(-\frac{t-t_j}{\tau}\right)(V_i - E_{syn}) \tag{3.8}$$

where $\mathrm{t_j}$ is the timing of the presynaptic spike in neuron j. The parameter w refers to the synaptic weight, where excitatory ($\mathrm{w_E}$) and inhibitory ($\mathrm{w_I}$) weights are changed separately. The reversal potential $\mathrm{E_{syn}}$ is 0mV for excitatory synaptic current and -75mV for inhibitory synaptic current. Synaptic current decay rate τ is set to be 0.5ms for both synapse types, simulating fast AMPA-like and GABA-A-like synaptic currents. Therefore, the total synaptic current to neuron i at time t is $I_i^{syn} = \sum_{j\in\Gamma_i} I_{ij}^{syn}$, where Γ_i is the set of pre-synaptic neurons to neuron i.

The dynamics of the network is numerically integrated by a fourth-order Runge-Kutta method with a time step 0.05ms. Total simulation time is 3 seconds, and the results shown are averages over 5 simulations.

3.2.3 Mean phase coherence measurement

The firing pattern and synchronization of neuron spike trains generated in the network are quantified by the Mean Phase Coherence (MPC) (Mormann, 2004). For the k-th spike in the spike train generated by neuron j denoted as $t_{j,k}$, its relative phase to the spike train generated by neuron i is given by $\theta_k = 2\pi \left(\frac{t_{j,k} - t_{i,k}}{t_{i,k+1} - t_{i,k}} \right)$, where $t_{i,k}$ is the timestamp of the nearest spike prior to $t_{j,k}$ in spike train i and $t_{i+1,k}$ is the nearest spike following $t_{j,k}$. The phase coherence of spike train j to spike train i is defined as $\sigma_{j,i} = |\frac{1}{N} \sum_{k=1}^{N} e^{i\theta_k}|$, where N is the total number of spikes in train j. This pairwise mean phase coherence takes on values between 0 and 1, with 0 indicating completely random firing, and 1 indicating stable phase locking.

3.2.4 Quantification of E/I ratio

At each time step, the total E and I synaptic current in the network is recorded. The mean E (or I) current is calculated by averaging these values over the whole time of the recording. We quantify the E/I ratio of the network as the ratio of mean E to mean I synaptic current, measured during time period T:

$$\frac{E}{I} = \frac{\int_0^T \sum_i \sum_j \sum_k w_E exp\left[\frac{t_{j,k}-t}{\tau}\right] \left(V_i\left(t\right) - E_{syn}^{E}\right) dt}{\int_0^T \sum_i \sum_j \sum_k w_I exp\left[\frac{t_{j,k}-t}{\tau}\right] \left(V_i\left(t\right) - E_{syn}^{I}\right) dt} \tag{3.9}$$

where k denotes the spike number occurring in the j-th pre-synaptic cell, j sums over all E cells in the numerator and over all I cells in the denominator, and i sums over all cells in the network.

In addition, we quantify the difference of synaptic currents or total current, calcu-

lated by subtracting the mean inhibitory current from the mean excitatory current, as this quantity is more directly connected to neuronal activity. The E=I balanced state is given by E/I ratio equals to 1 and zero total current.

3.2.5 Quantification of tightness of balance

The E/I ratio only quantifies the relative values of the excitatory and inhibitory synaptic currents averaged across the simulation. To further investigate the temporal relationship between the two currents and the tightness of balance, we calculated the cross correlation of the current time traces, computed by

$$I_X(t) = \sum_i \sum_j \sum_k w_X exp\left[\frac{t_{j,k} - t}{\tau}\right] \left(V_i(t) - E_{syn}^X\right) \tag{3.10}$$

where X=E,I and j sums over pre-synaptic neurons of type X and k sums over pre-synaptic spikes occurring before time t. By definition, loose balance corresponds to equal average amounts of excitatory and inhibitory current during a period of time, but without showing significant correlation between the current traces. Tight balance, on the other hand, is characterized by significant temporal correlation where fluctuations in inhibitory current closely follow the fluctuations in excitatory current.

3.3 Results

Here we investigate emergence of global asymptotic balance between excitatory and inhibitory currents in mixed excitatory-inhibitory neural networks. We vary the relative level of excitation and inhibition by changing the structural network parameters (i.e. synaptic weights) or neuronal input levels.

First, we manipulated E/I ratio in a randomly connected network by varying synaptic weights (Figure 3.1a) - for a fixed inhibitory synaptic weight w_I , the excitatory synaptic weight w_E was increased from 0 mS/cm^2 up to about 3 times the value

of w_I . For each value of w_E , we allow network dynamics to evolve to an asymptotic stable state, and then compute E/I ratio and total current (E – I) during a 1.5s time window. The curves in Figure 3.1b track the relationship between E/I ratio values and total current values as w_E was increased. Each data point on the curve represents one asymptotic E/I ratio for a specific value of w_E . As evident in the figure, the E/I ratio does not monotonically increase as w_E is increased, but can switch between excitation-dominant (E/I ratio ¿ 1 and positive total current) or inhibition-dominant (E/I ratio ¡ 1 and negative total current) regimes and cross the E=I balanced state (E/I ratio = 1 and zero total current) multiple times. Furthermore, the same value of E/I ratio can correspond to different values of total current with different network dynamics and firing patterns. The results show that the E/I level of the network cannot be represented comprehensively by either E/I ratio or total current alone, but requires both measures in a 2-D phase space. We demonstrate that this behavior is robust under a broad range of network parameters such as connectivity density (Figure 3.2a), ratio of excitatory cells (Figure 3.2b), network size (Figure 3.2c), and the neuron model (Figure 3.2f), indicating that this pattern of E/I regulation is general and applies to different neural systems. In the following sections, we give detailed characterizations of how network dynamics are governed by firing rates, synaptic weights, and neural membrane potentials, and at the E=I balanced state identify the mechanisms accounting for each balanced state regime by exploring the relationship between each dynamical characteristic and network E/I level. The turning points on the E/I trajectory split the balance states into three different regimes with different governing mechanisms. We study the three regimes by taking the three E=I balance states as examples. Finally, to test the universality of the results, we investigate how different network topologies affect the changes in E/I ratio and the occurrence of multiple balanced states as synaptic weights are varied. The consistency of the results demonstrates that our framework applies to a wide range of networks in a generic

way.

3.3.1 Network E/I trajectory crosses the E=I balanced states up to three times in response to varying synaptic weights

We first investigated how the E/I ratio evolves as a function of excitatory coupling for networks having different levels of overall coupling strength. The trajectory curves in Figure 3.1b show the relationship between E/I ratio and total current values in asymptotic balance states as w_E was increased for 4 different values of w_I ; we adjusted w_E accordingly to obtain the same E/I ratios. For each w_I value, initially, when $w_E = 0$ mS/cm^2, the E/I ratio was 0 and the total current fluctuated near zero. As w_E increased, E/I ratios increased but current differences remained small as the network passed through an E=I asymptotic balanced state. For each value of w_I , the E=I balanced state was reached for different values of w_E. Figure 3.1c shows how total spike numbers in the network (during the 1.5s simulation in the asymptotic balance state) varied with E/I ratio as w_E was systematically increased. When w_E 0 mS/cm^2 (and network activity was driven only by noise), network activity remained low in all networks as they crossed the E=I balanced state for the first time. For networks with weak inhibitory connectivity (blue and red curves), as w_E increased and E/I ratios increased significantly past the E=I balance point, excitatory synaptic current rapidly inundated the networks and increased network firing rates. In the network with weakest inhibition (blue curve), E/I ratio saturated around 5, and the network remained in an excitation-dominant regime (positive E/I ratio). With slightly stronger inhibition (red curve), increasing excitation in the network was able to drive inhibitory currents, so that the E/I ratio and total current trajectory curve decreased back near the E=I balanced state, albeit with higher network firing rates. For networks with stronger inhibitory connectivity (yellow and violet curves), two loops emerge in the trajectory curves: after crossing the E=I balanced state for the

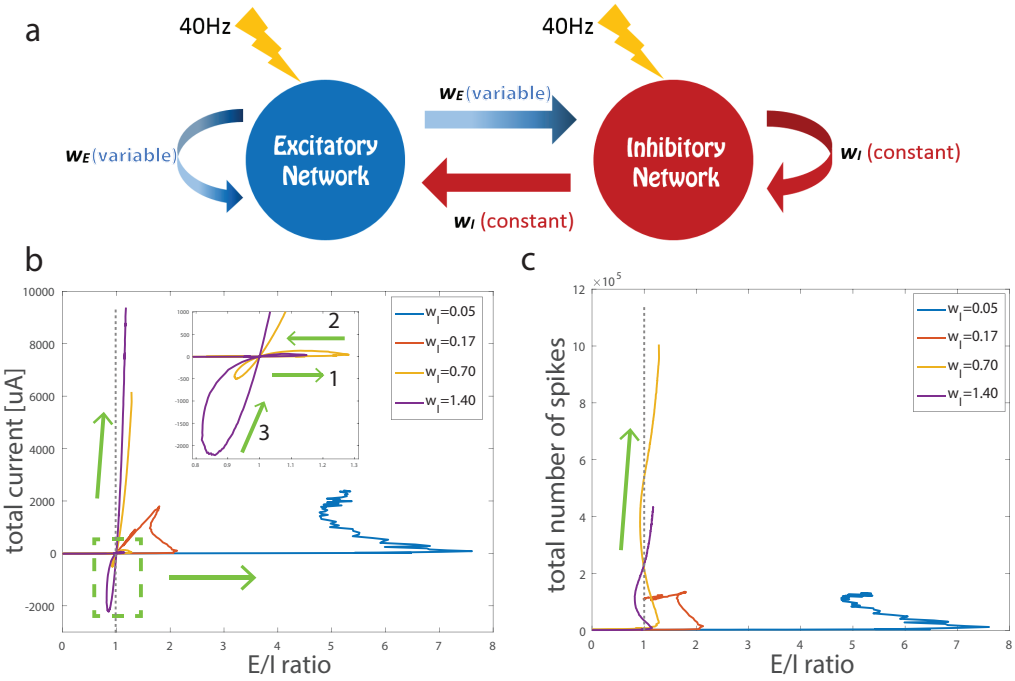

Figure 3.1: Figure 3.1. (a) Schematic of network structure illustrating synaptic interactions from inhibitory cells (red) with fixed synaptic weight w_I and from excitatory cells (blue) with varied synaptic weight w_E. Lightning bolts represent the external noisy stimuli with average frequency 40 Hz applied to each neuron in the network. (b) Relationship between E/I ratio values and E-I current difference (total current) values in asymptotic balance states as excitatory synaptic weight w_E was monotonically increased (arrows show direction of relative change with increasing w_E). Four trajectory curves correspond to 4 values of inhibitory synaptic weight w_I (given in legend in mS/cm^2). Inset in panel b shows a close-up of the asymptotic E=I balanced state (i.e. when E/I ratio is near 1 and total current is near 0) with two trajectories (violet and yellow) that crossed this balanced state 3 times. (c) Trajectory curves of E/I ratio values and network spiking activity values (in Hz computed during the 1.5s simulation in the asymptotic balance state), as excitatory synaptic weight w_E was systematically increased for the 4 values of w_I (arrows show direction of change with increasing w_E). For two trajectories (violet and yellow) although the E/I ratio oscillated above and below 1, spiking rates continued to increase as w_E was increased.

first time (inset, arrow 1), as w_E increased further, the trajectories turned around (arrow 2) and the networks crossed the E=I balanced state for a second time. As w_E continued to increase, the networks entered an inhibition-dominant regime (E/I ratio ¡ 1, negative total current). However, upon further increases in w_E, E/I ratios increased, leading to a third crossing of the E=I balanced state. Network firing rates continued to increase during these subsequent crossings of the E=I balanced state. As shown in Figure 3.1c, the networks generally showed higher spike rates with higher w_E, while the E/I ratio oscillated around 1. For the highest values of w_E, the networks remained in the excitation dominant regime with increasing total current and network firing. The surprising finding that E/I ratio repeatedly returns to 1 as excitatory current increases suggests, somewhat counterintuitively, that higher excitatory coupling may actually result in lower E/I ratio and total current in the network - increasing excitatory current can drive increases in inhibition, leading to non-monotonic changes in E/I ratio. For networks with strong inhibitory connectivity, we observe the formation of two loops in the trajectory curves, one in the excitation-dominant regime (i.e., E/I ratio is greater than one) and one in an inhibition-dominant regime (i.e., E/I ratio is below one). This shows that states exhibiting a particular E/I balance are not unique, but correspond to a set of network states with differential dynamical properties. To validate the generality of the non-monotonic E/I trajectories, we also analyzed networks with different parameters to take into account various possible biological realisms (Figure 3.2). Compared to the trajectory in Figure 3.1b, the qualitative pattern stays the same for all the new parameter combinations, including network size, connectivity density, the excitatory to inhibitory cell number ratio, asymmetry in various connection strengths, and finally different neuronal formalisms. The only additional modification made in these simulations was to adjust the value of w_I accordingly to maintain trajectories in the appropriate range. First, we investigated whether the effect averages out with increased network size, measuring (E/I)

ratio for a network consisting of 2000 neurons (Figure 3.2a). Next, as the sparsity of connectivity of the brain networks can vary from region to region, we simulated the networks with denser connectivity (Figure 3.2c).

As it has been measured that the percentage of excitatory cells in the mammalian cortex is around 80% (*Braitenberg and Schüz*, 1991), we modified the cell ratio accordingly - this case is shown in Figure 3.2b.

In the original simulations (Figure 3.1), we set $w_{EE} = w_{EI} = w_E$, $w_I = w_{IE} = w_I$. As, there is no evidence demonstrating that the excitatory (or inhibitory) synaptic weights are the same for synapses targeting excitatory and inhibitory populations, we applied different values for w_{EE}, w_{EI}, w_{IE}, w_{II} (Figure 3.2d and 2e) and tested cases where w_{EI}¿w_{IE} and w_{EI}¡w_{IE}. Finally, to validate that results are not due to the cellular properties of a specific neuron model, we simulated networks of Wang-Buzaki neurons (*Wang and G.*, 1996) in Figure 3.2f, which also have Type 1 excitability. It is evident that all the E/I trajectories under different parameter values display the same qualitative shape, indicating that the dynamic properties and the mechanisms in our framework are robust and are not constrained by some specific parameters of our models. Therefore, in the following discussion we consider network/cell parameters as described in Figure 3.1b to illustrate results and analyze mechanisms.

3.3.2 Network firing patterns are different in the three E/I balance regimes

We next investigated the differences in network dynamics at the E = I balanced states. As we will show below, the three different balance regimes, separated by the turning points of the two loops of the trajectory curves, are governed by qualitatively distinct mechanisms. To better understand the differences in dynamics between E/I balanced states, we focused on a network with moderate inhibition ($w_I = 0.7$ mS/cm^2, yellow curve in Figure 3.1b, c) that showed three crossings through E/I = 1. We chose the three values of w_E at which the network resides at (or near) the E=I

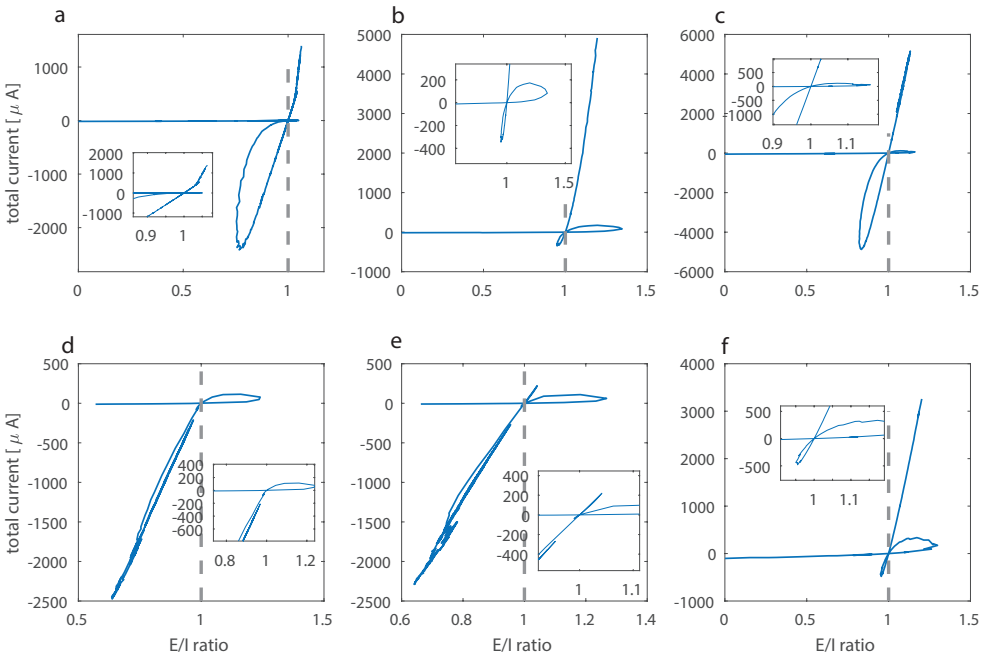

Figure 3.2: Trajectories of E/I ratio and total current values for networks with additional parameter changes addressing aspects of biological realism display the same qualitative behavior. Comparing with Figure 3.1b, the value of one parameter is changed in each panel while other parameters stay the same as original simulation. Inhibitory weight w_I is adjusted accordingly to show the appropriate E/I ratio range. a) random network with increased connectivity density (20% vs 3%, w_I=0.2mS/cm^2); b) 80% excitatory cells and 20% inhibitory cells (w_I=2.8mS/cm^2); c) random network with increased number of neurons (2000 vs 500, w_I=0.2mS/cm^2); d) different values for the four types of synapses, w_{EE} is varied, w_{EI} = 0.35mS/cm^2, w_{IE} = 0.5mS/ cm^2, w_{II} = 0.7 mS/ cm^2; e) same as panel d) but the values for w_{EI} and w_{IE} are reversed: w_{EI} = 0.5mS/ cm^2, w_{IE} = 0.35mS/ cm^2, w_{II} = 0.7 mS/cm^2; f) same network parameters as on Figure 3.1, with Wang-Buzaki neurons.

balance point (Figure 3.3a-c). Figure 3.3 shows network firing raster plots (second row), distributions of pairwise mean phase coherences (MPC, third row), and pairwise relative phases (fourth row) between all synaptically -connected neurons near the three E=I states.

For the first crossing of the E=I balanced state (left column), the system displayed random, sparse firing (Figure 3.3d), driven principally by external noisy stimuli. The MPC distributions almost overlapped (Figure 3.3g) for the four types of synaptically-connected cells (excitatory to excitatory (E-E), excitatory to inhibitory (E-I), inhibitory to excitatory (I-E), inhibitory to inhibitory (I-I)), and reflect no significant phase locking between the cell populations. The distribution of relative phases (Figure 3.3j) for excitatory (E) pre-synaptic cells peaked at low values of phase, while it was at its minimum for inhibitory pre-synaptic cells at these phases. This is intuitive in that E neurons tend to promote firing in post-synaptic cells, leading to small relative phases, while I neurons tend to suppress post-synaptic cell firing, thus inhibiting post-synaptic firing at small phases. These probabilities, however decay quickly (exponentially) to base value.

Network firing activity was greater at the second crossing of the E=I balanced state (Figure 3.3e), but the firing pattern remained largely random. The distributions of pairwise MPCs (Figure 3.3h) started to separate for the different types of synaptic connections between cells. Separation of the E-E and E-I pair groups (blue and red curves) to larger MPC values compared to the I-E and I-I pair groups (yellow and violet curves) means that neurons fired somewhat more coherently when pre-synaptic neurons were excitatory. The differences in the profiles of the pairwise phase distributions (Figure 3.3k) between pairs with E pre-synaptic neurons (blue and red curves) and pairs with I pre-synaptic neurons (yellow and violet curves) was maintained and solidified compared to the first crossing, reflecting the formation of more regular, causal firing patterns.

At the third crossing, network firing activity was high and some degree of synchronization started to emerge (Figure 3.3f). The significant separation in MPC distributions (Figure 3.3i) between pair groups with E pre-synaptic cells (blue and red curves) compared to I pre-synaptic cells (yellow and violet curves) points to higher coherence with E pre-synaptic neurons. Relative phases (Figure 3.3l) when pre-synaptic cells are E shifted towards 0 and 2π, indicating some degree of synchronization in the network. The larger peak in the distribution at 0 compared to 2π reflects a causal relationship in firing without synchronization. The phases for I pre-synaptic neurons, on the other hand, show a similar dip for low phase values as observed near the other balanced states without any significant change for higher phase values.

In summary, a significant separation in the distributions for both pairwise MPC and relative phases for E pre-synaptic cells and I pre-synaptic cells appeared gradually from the first crossing (Figure 3.2g, j) to the third crossing (Figure 3.3i, l), indicating a transition from a sparse and random firing pattern to a more organized and causal firing pattern. While the trend appears at the second crossing, it is more distinct at the third crossing where relative phases are clustered around 0 when pre-synaptic cells are excitatory, indicating causal initiation of post-synaptic firing. The rightward shift in MPC values from the first to the third crossing is further evidence for an increase in the coherence of the firing pattern.

3.3.3 Detailed dynamics at the E=I balanced states: first crossing

Next, to understand the cellular and network mechanisms underlying regulation of network dynamics at E=I balanced states, we separately considered the factors that influence the E/I ratio on both the cellular and network level. Here, conceptually, we can consider total synaptic current as consisting of the product of three factors: 1) the number of synaptic events (which is dictated by the overall firing activity of E or I cells), 2) the strength of synaptic events (governed by synaptic weight

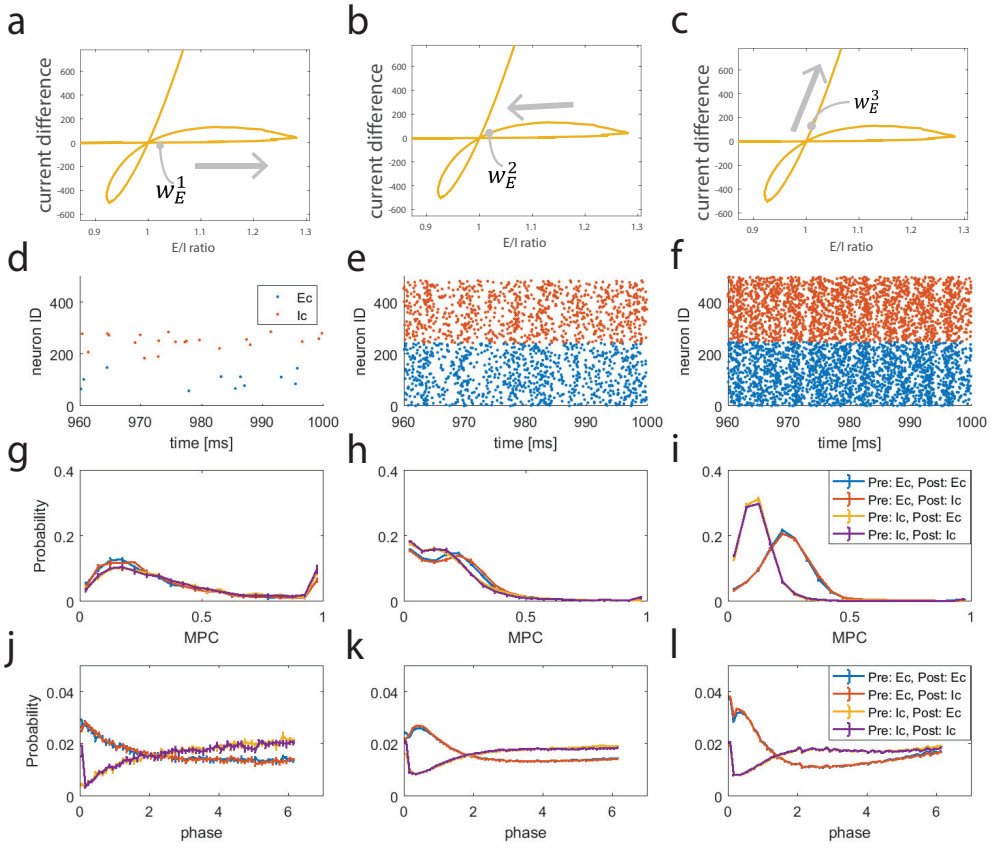

Figure 3.3: Firing patterns near three E=I balanced states for a network with $w_I = 0.7$ mS/cm^2. WE is chosen near the balanced state as marked on panels (a-c). (d-f) spike raster plot; (g-i) distribution of pairwise Mean Phase Coherences (MPCs) and (j-l) distribution of pairwise relative phases of neuronal firing computed near each balanced state. Mean Phase Coherences (MPC) (g-i) and relative phases (j-l) are computed only for pairs of synaptically connected neurons. The pairs are separated into four groups depending on the synaptic connections between them: excitatory to excitatory (E-E), excitatory to inhibitory (E-I), inhibitory to excitatory (I-E), inhibitory to inhibitory (I-I).

parameters), and 3) the driving force of synaptic current (dictated by the difference between the mean membrane voltage of the post-synaptic cells and the current's reversal potential). Thus, we can represent the E/I ratio by the following expression:

$$\frac{E}{I} = \frac{total\ I_E^{syn}}{total\ I_I^{syn}} \cong \frac{excitatory\ population\ firing\ frequency}{inhibitory\ population\ firing\ frequency} \times \frac{w_E}{w_I} \times \frac{\sum_i \bar{V}_i - E_E^{syn}}{\sum_i \bar{V}_i - E_I^{syn}} \tag{3.11}$$

where $\bar{V}_i$ is mean membrane potential of the i-th cell and i sums over all cells in the network. In our results in Figure 3.1 and Figure 3.3, we varied synaptic weights w_E and w_I, which induced changes in the other factors, altered the level of firing activity, and changed membrane potential. In an attempt to disentangle the interactions among these factors, we implemented a different method to manipulate E/I ratio in the network. To do this, w_E and w_I are fixed at specific values near an E=I balanced state, and E/I ratio is varied by changing the frequency of external stimuli (random, pulse like events) to E cells in the network. The frequency of these events was varied between 5 and 75 Hz, while noise event frequency to I cells was maintained at 40Hz (Figure 3.4a). Since here the synaptic weights are fixed, crossing through the E=I balanced state is caused by changes in the other two factors (i.e. spike frequency and mean voltage difference between cell membrane potential and reversal potential in above equation). Therefore, we monitored mean synaptic currents, firing rates, and the mean membrane potential of cells in the network to further characterize the three balanced states displayed in the network with moderate inhibition (w_I = 0.7 mS/cm^2) from Figure 3.3. We start with a detailed analysis of the first crossing of the E=I balanced state.

We set w_E to a value such that the network sits just below the first E=I balanced state. Figure 3.4b shows the relationship between the E/I ratio and the mean firing

rates of the E and I cells as the noise event frequency to the E cells was increased from 5 to 75 Hz. At the lowest noise frequency, E/I ratio was low (0.2) and E cells (blue curve) fired less than I cells (red curve). As the noise frequency was increased, E/I ratio increased, with the firing rate of E cells (blue curve) increasing more than that of I cells (red curve), which were also increased as a result of greater excitatory synaptic activity in the network. As the E=I balanced state was approached (i.e. with increasing noise frequency), E cell firing rates surpassed I cell firing rates and the difference in firing rates (Figure 3.4c) between E and I cells moved from negative values to positive values.

To track the efficacy of the synaptic currents due to increased firing in the network, we computed the mean membrane potential of E and I cell populations, $\bar{V}_E$ and $\bar{V}_I$, respectively during simulations with increasing noise frequency. Figure 3.4d shows the difference between mean membrane potentials and the reversal potentials (i.e. distance to RP) of E (blue curves, left vertical axis) and I (red curves, right vertical axis) synaptic currents, E_E^{syn} and E_I^{syn}, respectively. Due to increasing firing activity in the network, mean membrane potentials of both E and I cell populations were depolarized, resulting in their voltage values closer to E_E^{syn} and farther from E_I^{syn} for both populations. The E cell population depolarized at a higher rate (as a function of increasing noise frequency) than the I cell population with increasing noise frequency (as shown in Figure 3.4d and e). The difference between mean voltages and E_E^{syn}, $|\bar{V}_E - E_E^{syn}| - |\bar{V}_I - E_E^{syn}|$, transitioned from positive values to negative values as noise frequency increased (blue curve). The difference between mean voltages and E_I^{syn} showed opposite behavior (red curve). Based on these data, we conclude that the first balanced state is achieved in the network by increased firing rates of the excitatory cell population relative to the inhibitory cell population. However, this difference in firing rates is partially compensated by a decrease in the efficacy of excitatory synaptic currents in the network, due to decreased voltage difference between

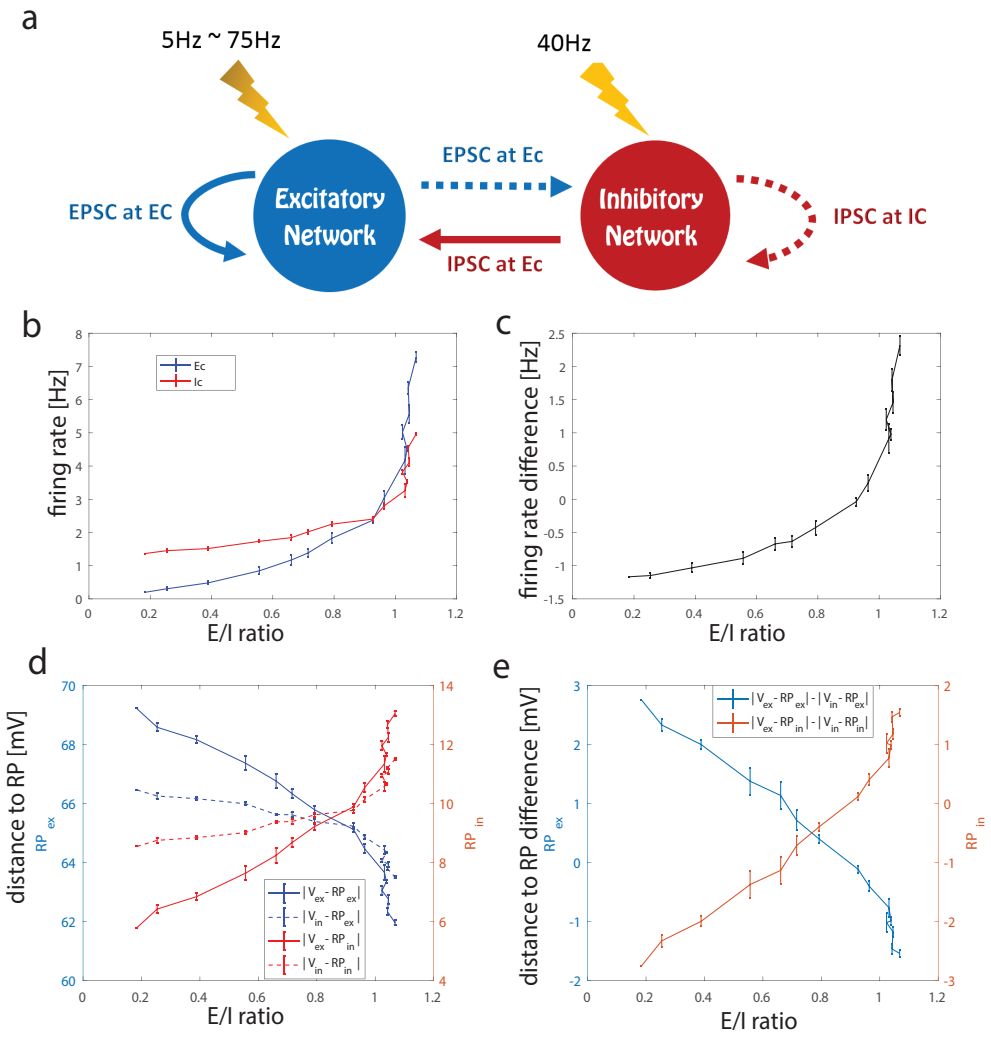

Figure 3.4: Analysis of network factors contributing to E/I balance at the first crossing of the E=I balanced state. (a) Schematic of alternate method to change E/I ratio. Synaptic weights are fixed near the E=I balanced state and frequency of noisy external stimuli to the excitatory (E) cells is varied (see text for details). (b) Relationship between E/I ratio values and mean firing rates of the excitatory (E, blue curve) and inhibitory (I, red curve) cell populations as noise event frequency to the E cells is increased. (c) Difference between blue and red curves in (b). (d) Relationship between E/I ratio values and the difference between the mean membrane potentials of the excitatory ($\bar{V}_E$) and inhibitory ($\bar{V}_I$) cell populations, and the reversal potentials of the excitatory (E_E^{syn}) and inhibitory (E_I^{syn}) synaptic currents as noisy event frequency to the E cells is increased. Blue (red) curves show distances from E_E^{syn} (E_I^{syn}). (e) Difference of distance curves shown in (d).

membrane potential and reversal potential. The results shown in Figure 3.4d suggest that EPSCs and IPSCs are differentially distributed to E and I cell populations. We next took a closer look at this.

In the E=I balanced state, mean total EPSC and mean total IPSC are equal in the network. However, excitatory and inhibitory synaptic currents are not necessarily uniformly distributed among E and I cell populations. Here we analyze the relative magnitudes of the four types of post-synaptic currents: excitatory current to E cells (EPSC at E cells), excitatory current to I cells (EPSC at I cells), inhibitory currents to E cells (IPSC at E cells), inhibitory currents to I cells (IPSC at I cells), where "EPSC" and "IPSC" refer to mean total synaptic current arriving at the post-synaptic population (Figure 3.5a). As the noise frequency in E cells was increased and the E/I ratio passed through the E=I balanced state, all four types of synaptic current increased. At the E=I balanced state, the difference between total EPSC and total IPSC (values of blue curves – values of red curves when E/I ratio is 1) is zero. To identify the relative distribution of synaptic currents in the network, we next considered what we call the "net current difference" which we defined in two different ways, as follows.

First, we computed the net synaptic current received by E cells and I cells separately (Figure 3.5b, c). To do this we separately calculated the net synaptic current received by E-cells as (EPSC at E cells) − (IPSC at E cells) (Figure 3.5b), and the net synaptic current received by I-cells as (EPSC at I cells) − (IPSC at I cells) (Figure 3.5c). As the noise frequency in excitatory cells increased and E/I ratio crossed through the E=I balanced state, net synaptic current to both cell populations increased from negative values to positive values reflecting a greater increase in the excitatory synaptic current received by both populations compared to inhibitory synaptic current. We then compute a "net current difference" by subtracting the net synaptic current curves in Figure 3.5b and 5c (Figure 3.5f). This net current differ-

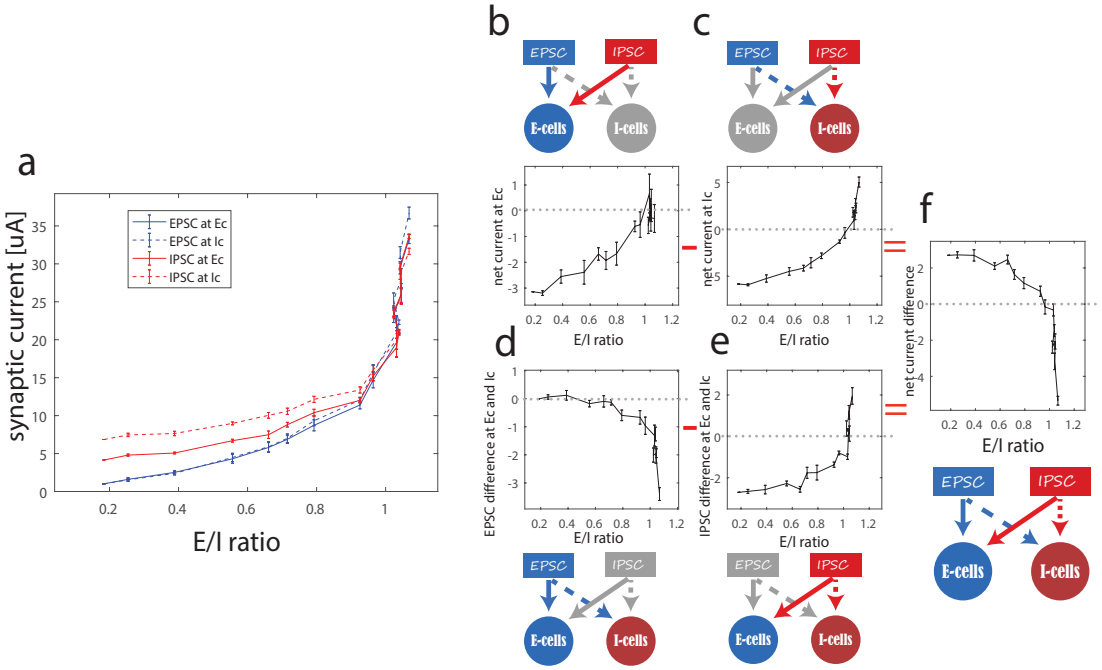

Figure 3.5: Distribution of synaptic current in the network at the first crossing of the balanced state. (a) Trajectories of the four different types of mean total synaptic currents, Excitatory Post Synaptic Current (EPSC) at excitatory cells (blue solid), EPSC at inhibitory cells (blue dash), Inhibitory Post Synaptic Current (IPSC) at excitatory cells (red solid) and IPSC at inhibitory cells (red dash) as E/I ratio is varied by increasing the frequency of noise events to the excitatory cell population. The relative distribution of excitatory and inhibitory currents to the excitatory and inhibitory cell populations is displayed in two different ways (b and c, or d and e). The color and pattern of the arrows in the diagrams are consistent with the curves in panel a. (b) Net synaptic current received by E cells, which is the difference of EPSC and IPSC at E cells (difference between blue and red solid curves in panel a). (c) Net synaptic current received by I cells, which is difference between EPSC and IPSC at I cells (difference between blue and red dashed curves in panel a). (d) Difference of EPSC received by the E cells and the I cells (difference between blue solid and blue dashed curves in panel a). (e) Difference of IPSC received by E cells and I cells (difference between red solid and red dashed curves in panel a). (f) Difference of the net currents shown in (b) and (c) indicating which population received more net current, or equivalently difference of currents shown in (d) and (e) indicating which type of current is more distributed in E cells compared to I cells.

ence shows that the synaptic currents to the inhibitory cell population dominate at this crossing of the E=I balanced state: below the E=I balanced state, IPSC at I cells is greater than IPSC at E cells. As the E=I balanced state is crossed, EPSC at I cells is greater than EPSC at E cells.

Second, we compared the relative magnitudes of EPSCs and IPSCs received by the two cell populations (Figure 3.5d, e). This alternate way takes the point of view of the synaptic current in the network. We computed the difference between EPSC received by E cells and I cells: (EPSC at E cells) − (EPSC at I cells) (Figure 3.5d), and the difference between the amount of inhibitory synaptic current received by E and I cells (IPSC at E cells) − (IPSC at I cells) (Figure 3.5e). Below the E=I balanced state, the I cells receive more inhibitory current while the excitatory current is roughly evenly distributed, but as the noise frequency to E cells increases, EPSC at I cells exceeds that at E cells. The difference of the curves in these two panels yields the "net current difference" in Figure 3.5f.

Thus, a characteristic of this E=I balanced state is that increased activity of E cells drives the network into an excitation-dominant regime, in which E cells increase their firing rates relative to I cells. While the efficacy of EPSC in the network decreases due to reductions in driving force (i.e., due to overall depolarized membrane potentials), as the E=I balanced state is crossed, EPSC dominates over IPSC (Figure 3.5b and c). At the E=I balanced state, I cells receive more EPSC than E cells (Figure 3.5d) and beyond the E=I balanced state, in the excitation-dominant regime, E cells receive more IPSC than I cells (Figure 3.5e).

3.3.4 Detailed dynamics at the E=I balanced states: comparison of dynamics at the three balanced states

We next extended this analysis to compare network dynamics at all three crossings of the E=I balanced states (Figure 3.6). Near each, we chose a value of w_E (blue,

black and yellow data in Figure 3.6) and increased E cells' noise frequency to vary the E/I ratio. For each w_E value, we examined the trajectory of the E/I ratio and the difference in firing rates between E and I cells (first column, similar to Figure 3.4c), and the difference between the absolute value of the mean membrane potentials of E and I cells (second column). This latter value directly affects the relative voltage distance of the two cell populations to EPSC and IPSC reversal potentials. We also assessed the trajectory of the E/I ratio vs. net current difference (as in Figure 3.5f; third column; arrows indicate the direction of change as noise frequency increases) and vs. total current (E-I) in the network (as in Figure 3.1a; fourth column). Changes due to increasing noise frequency follow the same path as those due to increasing w_E.

The trajectories shown in Figure 3.6 illustrate the effects on these measures of network activity for three different values of excitatory synaptic weight (yellow, black, and blue) in response to increasing frequency of external noise events to E cells at E=I balance crossings (dashed arrows indicate change direction with increasing noise frequency). At the first crossing (top row), trajectories for different w_E values almost overlap, suggesting that the state of the network is determined by the relative frequency of cell population firing. At the 2nd crossing (middle row), trajectories for different synaptic weights occupy different intervals of E/I ratio values, but all show the same trends as noise frequency increases. This suggests that noise and internal synaptic interactions together control network dynamics. Finally, at the 3rd crossing (bottom row), synaptic weight has a much greater effect on E/I ratio as trajectories remain essentially at fixed E/I values as noise frequency increases. In this case, external drive does not strongly affect network dynamics due to strong synaptic interactions (caused by high w_E values) in this regime. At each of the three crossings of the E=I balanced state, the trajectories for different w_E values (blue, black and yellow) are similar with increasing noise frequency, indicating a qualitative consistency

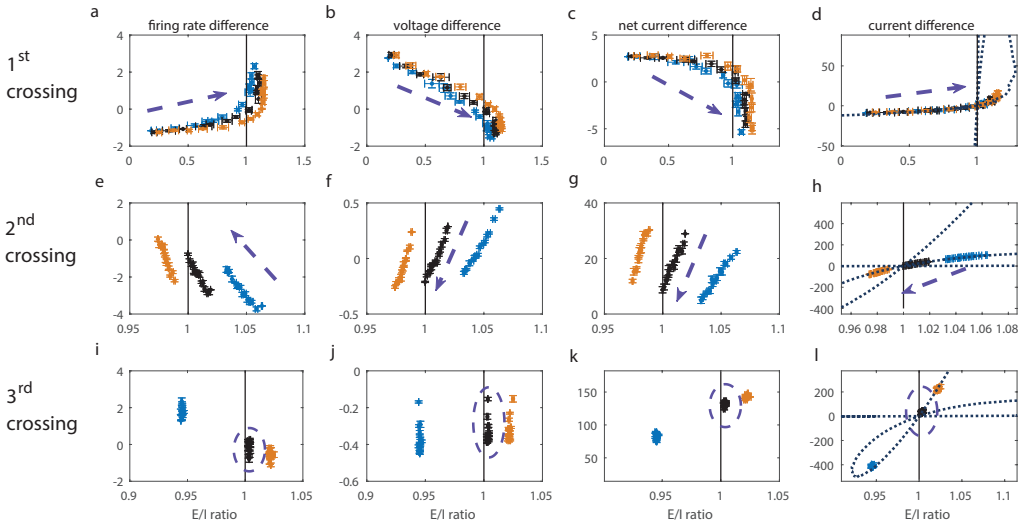

Figure 3.6: Comparison of network dynamics at the first (top row), second (middle row) and third (bottom row) crossings of the E=I balanced state. Near each E=I balanced state, three different values of w_E are chosen representing low (blue data points), medium (black data points) and high (yellow data points) values of w_E. For each value of w_E, the frequency of noise events to the E cells is varied between 5 and 75Hz while the noise event frequency to the I cells is kept at 40Hz (dashed arrows indicate direction of change with increasing noise frequency). Trajectories of E/I ratio values and (a, e, i) firing frequency difference between the E and I cells; (b, f, j) absolute value of mean voltage difference between the E and I cells; (c, g, k) "net current difference" (see text for description) between the E and I cells; and (d, h, l) total current (E-I).

of effects. Due to this consistency, we focused on properties of one trajectory (black) for each crossing. The trajectory through the first crossing of the E=I balanced state (Figure 3.6, top row) replicates the results shown in Figure 3.4c, 4e (blue curve), and 5f, respectively. Near the second crossing (middle row), initially the frequency of I cells is higher than that of E cells. As E cells' noise frequency increases, their firing frequency increases relative to that of I cells, resulting in smaller firing rate differences (Figure 3.6e). This results in depolarization of both cell types in the network, evidenced by smaller differences in mean voltage between E and I populations (Figure 3.6f). Depolarization causes the EPSC driving force to decrease and consequently, the IPSC driving force to increase, overall decreasing EPSCs and increasing IPSCs. This change is not uniform, however, as E cells depolarize more than I cells (i.e. $|\bar{V}_E| - |\bar{V}_I|$ becomes negative). These two effects result in overall decrease of net current difference (Figure 3.6g), due to a) increased depolarization of E cells vs. I cells, and b) the non-intuitive increase in inhibitory current in the network resulting from depolarization of both cell types (Figure 3.6h). These same trends are observed for all three w_E values (blue, black and yellow points). Hence, at the second crossing of the E=I balanced state, either increased spiking of E cells or increases in excitatory synaptic weight act to push total network inhibition to be dominant. As we show below, membrane potential depolarization means that decreased EPSC driving force and increased IPSC driving force may be responsible for an overall decrease in EPSC efficacy in the network at the crossing of this balanced state.

At the third crossing of the E=I balanced state (third row), increasing noise frequency to E cells has smaller effects on E/I ratio than changes in w_E (blue to black to yellow data points). At this balanced state (black points), E cells and I cells have similar firing rates (Figure 3.6i) with I cells only slightly more depolarized than E cells (Figure 3.6j). However, the w_E/w_I ratio skews the current significantly towards EPSC domination within the network. Moreover, as shown below (Figure

3.8), greater synchrony of firing patterns emerges in this state, driving the network toward balanced firing rates. Thus, similar to the first crossing of the E=I balanced state, increases in excitatory synaptic activity (due to weight increases) act to push the network from the inhibition dominant regime into the excitation dominant regime.

3.3.5 Detailed dynamics at the E=I balanced states: Competition between the firing rate ratio and the depolarization ratio

The primary distinction between the first and second crossings of the E=I balanced state is illustrated by relating the changes in total current (E-I, Figure 3.6, last column) with changes in firing rate differences (first column) and membrane potential differences (second column) between E and I populations. At both crossings, increases in firing rate difference occur with decreases of voltage difference. However, at the first crossing total current increases mirroring the change in firing rate difference; in contrast, at the second crossing total current decreases in response to the change in voltage difference. This suggests that E/I ratio actually depends on competition between two opposing constraints: the ratio of firing rates of E and I cells (which we refer to as Nratio), and the ratio of driving forces for EPSCs and IPSCs (which we refer to as Vratio). Figure 3.7 displays the trajectories of Nratio (x-axis) and Vratio (y-axis) for the three crossings, with E/I ratio values indicated by color. Here, as in Figure 3.6, w_E is constant and trajectories show changes in response to systematically increasing the frequency of noise events to E cells.

At the first crossing (Figure 3.7a), E/I ratio increases mirror Nratio increases. At the same time, Vratio decreases, meaning that the change in E/I ratio is driven by Nratio in this regime. However, this relationship is reversed at the second crossing (Figure 3.7b), with increasing E/I ratio mirroring increasing Vratio (while Nratio decreases). On the other hand, at the third crossing (Figure 3.7c) there is no clear relationship between E/I ratio and either Nratio or Vratio. In this case E/I ratio is

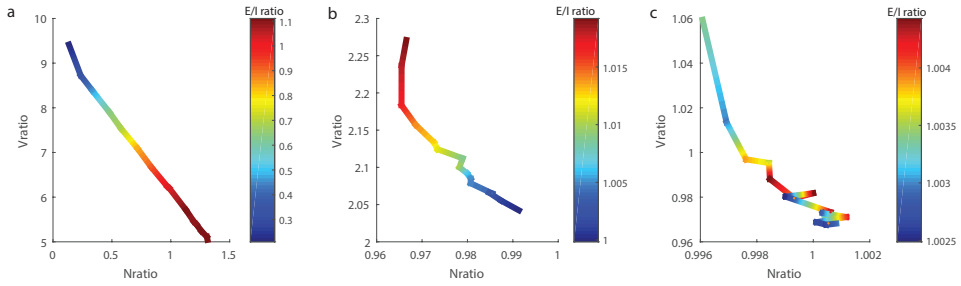

Figure 3.7: The contribution of changes in E and I firing rates (Nratio) and excitatory and inhibitory synaptic current driving forces (Vratio) to changes in E/I ratio. Values for w_E are fixed near each balanced state (a: first crossing, b: second crossing, c: third crossing) and frequency of noise events to E cells is increased to vary E/I ratio (color of curves). Curves show relationships between values of the ratio of E to I cell average firing rates (Nratio, x-axis) and values of the ratio of differences between average membrane potentials and reversal potentials of the excitatory and inhibitory synaptic currents (Vratio, y-axis) at each value of E/I ratio. At the first crossing (a), increasing E/I ratio mirrors increasing Nratio while at the 2nd crossing it mirrors increasing Vratio.

minimally affected by external noise frequency, and oscillates near 1 (note the change in color scale). Taken together, these findings show that the change of E/I ratio in the network can result from different mechanisms, depending on the relative change of firing rates and depolarization levels of E and I populations.

3.3.6 Detailed dynamics at the E=I balanced states: Quantification of tightness of E/I balance

The E/I ratio measures the relative amounts of total EPSC and IPSC in the network across a period of time, but it does not indicate the temporal relationship between variations in these currents. To analyze differences in the temporal occurrence of EPSC and IPSC at the three balanced states, we calculated the cross-correlation of the time traces of total EPSC and total IPSC for a range of w_E values in a network with moderate inhibition (w_I = 0.7 mS/cm^2) (Figure 3.8). As w_E increased driving the network across all three balanced states (Figure 3.8a), stronger correlations and

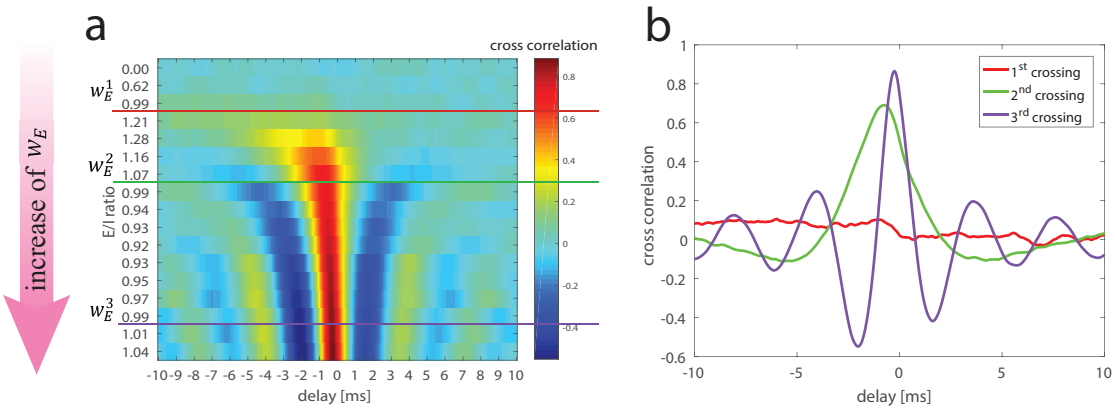

Figure 3.8: Temporal relationship of total excitatory and inhibitory synaptic currents. Cross-correlation (a, color) of the time traces of the total excitatory and inhibitory synaptic currents as w_E is varied (direction of arrow) driving the network across the three balanced states indicated by w_E^1 (red curve), w_E^2 (green curves) and w_E^3 (violet curves). b) Cross correlation traces between the E and I currents at the three crossings of the balanced state. Negative delay indicates excitation leads inhibition.

multiple peaks emerged, and the temporal delay between EPSC and subsequent IPSC decreased.

Cross-correlations at the three balanced states are shown in Figure 3.8b. The first balanced state (red curve) displays a loose temporal relationship (corresponding to 'loose E/I balance') (*Denève and Machens*, 2016), with no significant correlations between the two currents. In contrast, the second balanced state (green curve) shows "tight E/I balance" with a single peak in the correlation offset at a negative value indicating EPSC leading IPSC on a millisecond timescale. The third balanced state (violet curve) shows even tighter correlation, with a shorter delay and stronger correlation between the currents. Additionally, the appearance of multiple peaks in the correlation indicate that global oscillatory dynamics have emerged in the network.

3.3.7 Network topology affects the E/I ratio trajectory when changing synaptic weights

Finally, to test how robust these different E/I balanced states are, we vary the network connectivity structure (Figure 3.9). We construct a two-layer network, one E cell layer and one I cell layer, with synaptic connections both between and within layers. We start with nearest neighbor connections and a 2.5% connectivity density. We then systematically vary inter-layer and intra-layer connectivity structure by defining synapse rewiring probabilities (rp_E and rp_I) which dictate the degree in randomness in re-wiring of E and I synapses, respectively. In Figure 3.9 we consider nine different connectivity combinations: local excitation (rp_E=0, first column), small-world excitation (rp_E=0.2, middle column) and random excitation (rp_E=1, last column) with local inhibition (rp_I=0, blue curves), small-world inhibition (rp_I=0.2, red curves) and random inhibition (rp_I=1, yellow curves).

As in Figure 3.1, as w_E increases (with moderate inhibition $w_I = 0.7$ mS/cm^2), the trajectories of E/I ratio values (x-axis) and total current (E-I) values (top row, y-axis) cross through the E=I balanced state up to three times as network firing rates (bottom row, y-axis) show non-monotonic changes. When E connections are local (first column), the connectivity pattern of I synapses can have a large effect. For local or small-world inhibitory synaptic connectivity (blue and red curves), the E/I ratio trajectories are similar as with completely random connectivity - with three crossings of the E=I balanced state as w_E is increased. However, with random inhibitory synaptic connectivity (yellow curves), resulting in global inhibition in the network, only two crossings of the E=I balanced state occurred. Furthermore, the network remained in the inhibition dominant regime for high w_E. This is due to the fact that EPSCs excite the I cell population only locally, while the global IPSCs can suppress firing effectively, evidenced by the flat portion of the firing rate trajectory (Figure 3.9d, yellow curve). When E synapses have small-world (middle column) and random (right column) con-

nectivity structure, three crossings of the E=I balanced state occur regardless of the inhibitory synaptic structure. Here the global component of excitation, generated by random excitatory connections, offsets the effects of inhibitory synaptic connectivity. For random excitatory connectivity (c), the trajectory curves almost overlap for all inhibitory connectivity structures, while with small-world excitatory connectivity (b), the trajectory curves are modulated by inhibitory connectivity structure.

3.4 Discussion

We have provided a schematic picture of the cellular and network mechanisms that determine changes of E/I ratio in a biophysical neural network model. Our results show that neurons and networks have a homeostatic capability to regulate the balance for excitation and inhibition via the competitive contribution between firing rates and the voltage difference between membrane potential and the respective reversal potentials across a relatively wide range of network excitation levels. This homeostatic effect is particularly evident at the second E=I balanced state, where increased activity of E cells invokes increased IPSC in the network. On the other hand, we show that the dynamical mechanisms regulating a network toward balanced excitation and inhibition can change depending on the relative amount of excitation in the network, placing the system in diverse dynamical regimes. Specifically, at the first crossing of the E=I balanced state (when excitation in the network is low), firing rates of E cells drive changes in the E/I ratio, while at the second crossing (with higher excitation), E/I ratio is influenced by the efficacy of postsynaptic currents, which is determined by the voltage difference between membrane potential and the respective reversal potentials. Thus, our present data suggest that there is no universal E=I balanced state determined by a single mechanism. Rather, our results show that the dynamics towards a balanced state is driven by the interaction of both network activity and cellular depolarization levels. Further, our results show that experimental measurement

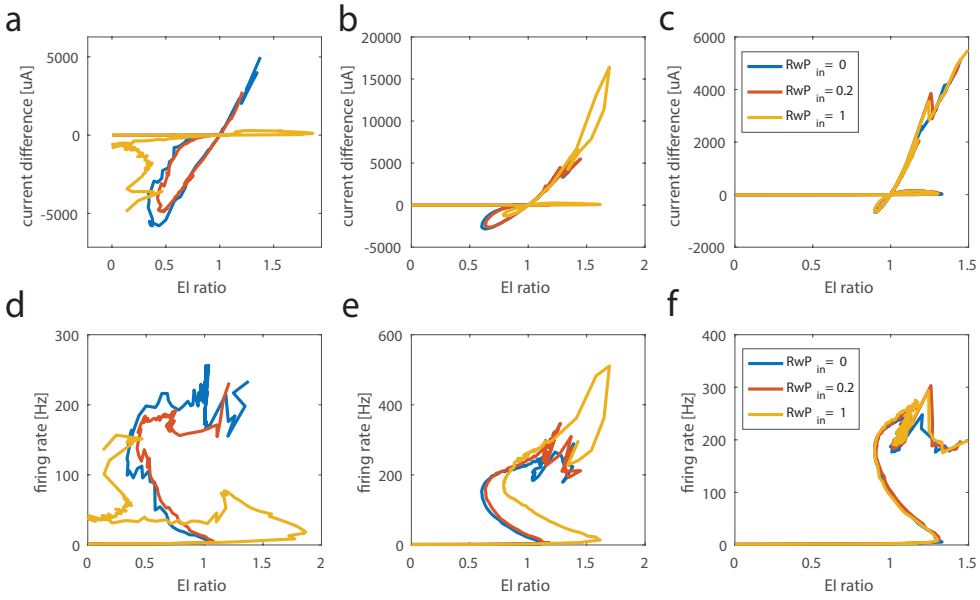

Figure 3.9: Trajectory curves of E/I ratio values and total current (E-I) values (top row), and network firing rate values (bottom row) as excitatory synaptic strength increases for networks with different connectivity structures. Networks are composed of one layer of excitatory cells and one layer of inhibitory cells, which are connected within and between layers with 2.5% connectivity probability. The synapse rewiring parameter for excitatory (rp_E) and inhibitory (rp_I) synapses are changed separately, resulting in different network topologies. Excitatory synaptic strength, w_E , increases from 0 while inhibitory synaptic strength w_I =0.7mS/cm^2 stays constant. In all panels, different curves show results for different inhibitory connectivity structures (blue: local inhibition, rp_I=0; red: small world inhibition, rp_I=0.2; yellow: global inhibition, rp_I=1). Columns show results for different excitatory connectivity structures: (a, d) local excitation (rp_E=0); (b, e) small world excitation (rp_E=0.2); (c, f) global excitation (rp_E=1).

of single specific cellular or network property, such as ratio of conductances (*Monier et al.*, 2008) or amplitudes of PSCs (*Wehr and Zador*, 2003; *Xue et al.*, 2014), may not provide adequate information about the E/I ratio in the system, as the E/I ratio is an outcome of the combined effects of firing rates, membrane depolarization and synaptic weights, which also affect each other recurrently.

Tightness of temporal correlation between excitation and inhibition (Figure 3.8) is another important and experimentally measurable dynamical property providing information about the system's activity regime. In our model, only the first crossing of E=I balance point has low correlation between excitation and inhibition (i.e. loose balance) while the other two are tightly correlated (i.e. tight balance). This observation may provide an explanation for the emergence of the two types of balance. Loose balance emerges in a relatively low coupling regime and the variation in the relative strength of excitation and inhibition is driven predominantly by external input. This, in turn, results in a similar average level of E and I currents but no correlation. On the other hand, tight balance is due to recurrent interaction between excitatory and inhibitory synapses, which results in significant temporal correlation between the two currents. As depicted in Figure 3.8, as excitatory synaptic weight w_E increased, the correlation between the two currents developed and the temporal delay between them decreased.

Finally, network connection topology additionally may affect the dynamics of E/I ratio and the pattern of E/I regulation. This is most clearly observed when excitation is kept local in the network (Figure 3.9a): increasing randomness of inhibitory connections significantly alters how E/I ratio changes with increasing excitatory synaptic weight, resulting in the network remaining in the inhibition dominant regime when inhibition is globally distributed in the network. However, the general mechanism of the regulation stays the same as our framework, i.e. E/I ratio depends on the relative contribution between firing rates and depolarization level. Our results potentially

reconcile a number of discrepant experimental observations. For example, one recent study suggested that E/I ratios are pushed towards an inhibition dominant regime during wakefulness, when compared with the same brain network under anesthesia (*Haider et al.*, 2013). However, other experimenters have found that excitation and inhibition are at similar levels when comparing sleep states and wakefulness (*Chellappa et al.*, 2016; *Ly et al.*, 2016; *Niell and MP.*, 2010). These discrepancies may have profound implications for how the brain processes information. For example, the reported features of tuning curves for excitation and inhibition (i.e., in response to variations in external sensory stimuli) vary across studies. Similar tuning curves are observed in some experiments (*Wehr and Zador*, 2003; *Zhou et al.*, 2014; *Runyan et al.*, 2010) while others have found either wider tuning (*Niell and MP.*, 2010; *Kerlin et al.*, 2010) or narrower tuning (*Sun et al.*, 2013) for inhibition, as compared to excitation. We speculate that the discrepancies in experimental findings may result from differing contributions of firing rate and membrane depolarization between experiments, which push the networks under study into different balanced state realizations.

Together, our results point to complex interactions between excitatory and inhibitory currents in the balanced network regime. The above characterization of the repertoire of diverse balanced states provides a theoretical framework for experimental studies quantifying E/I balance and characterizing network interactions in various brain states and modalities.

CHAPTER IV

Heterogeneous Mechanisms for Network Synchronization Under Different Excitatory/Inhibitory Balance Regimes

4.1 Introduction

Synchronization has been observed in a wide variety of brain processes within different brain regions (*Diesmann et al.*, 1999; *Steriade*, 2001; *Buzsáki*, 2004a; *Brovelli et al.*, 2004; *Lakatos et al.*, 2005; *Buzsáki*, 2006; *Kumar et al.*, 2010; *Fell and Axmacher*, 2011; *Babapoor-Farrokhran et al.*, 2017; *Zhou et al.*, 2019). Coherent firing patterns are thought to be essential in multiple cognitive functions such as multimodal information integration, memory consolidation as well as information transfer, and may be a fundamental mechanism for large-scale integration of distributed neuronal organizations (*Varela et al.*, 2001; *Fell and Axmacher*, 2011; *Buzsáki and Watson*, 2012). On the other hand, abnormal neuronal synchronization is thought to underlie cognitive dysfunctions, such as epilepsy, schizophrenia etc. (*Spencer et al.*, 2003; *Lewis et al.*, 2005; *Ferrarelli et al.*, 2010; *Uhlhaas and Singer*, 2006). Oscillatory network-wide patterning being a direct consequence of synchronization of periodic activation is thought at the same time to mediate information transfer throughout disparate brain regions (*Fell and Axmacher*, 2011; *Buzsáki and Watson*, 2012;

Hahn et al., 2018). Thus, both synchronization and population level oscillations, are proposed to provide an efficient mechanism for communication between distributed "sender" and "receiver" brain regions (*Buzsáki and Watson*, 2012). While both phenomena are closely related they can be distinct and happening on different time-scales, mediate binding of different signal features (*Hahn et al.*, 2018). Furthermore, cross frequency coupling of nested synchronous and oscillatory dynamics at diverse temporal and spatial scales support the hierarchical organization of the information transfer in top-down and bottom-up functions (*Fell and Axmacher*, 2011; *Aru et al.*, 2015; *Axmacher et al.*, 2010; *Naze et al.*, 2018; *Palva and Palva*, 2017).

A lot of theoretical studies identified diverse mechanisms of emergence of synchronous and oscillatory dynamics (*Ermentrout and Kopell*, 1998; *Börgers and Kopell*, 2003; *Brunel and Wang*, 2003; *Geisler et al.*, 2005). For example, in hippocampus alone, different types of GABAergic interneurons are demonstrated to drive the emergence of synchrony by either excitatory (somatostatin) or inhibitory (*Hilscher et al.*, 2017) synaptic connections (*Wester and McBain*, 2016). In general, the mechanisms generating synchronous oscillations can be divided into two groups: 1) network mediated and 2) those driven by properties of neuronal excitability. The prominent example of the first is so called pyramidal-interneuron gamma (PING) (*Traub et al.*, 1996) mechanism and its derivatives. Here the oscillation emerges as a close interaction of excitation and inhibition in the network. Strong excitation triggers inhibitory burst which feeds back onto the excitatory cells effectively shutting them down for a period of time. Decrease of this inhibition leads to another burst of excitatory activity repeating the process. In this case the synchronous patterning is based on the recurrent interactions of excitatory and inhibitory sub-networks rather than excitability properties of individual neurons. The second group depends on intrinsic membrane properties of individual neurons. These properties include subthreshold oscillations and/or so called type II excitability that promotes synchronization of neuronal spik-

ing patterns (*Ermentrout*, 1996; *Gutkin and GB.*, 1998; *Prescott et al.*, 2008). These resonator-type neurons are able to be recruited effectively by the oscillatory local field potential (LFP) and fire coherently, which mediates synchronous activities throughout distant brain regions and generate an interplay between the brain rhythms of different frequency bands (*Varela et al.*, 2001). Coherent subthreshold membrane potential oscillations are thought to play an important role in functional selection and grouping (*Engel et al.*, 2001).

However, some questions still remain unresolved. To what degree these two classes of mechanisms can coexist within the same network? What promotes emergence of one mechanism over another in context of structural network properties? And how emergence of these oscillations regulates temporally the excitatory/inhibitory balance within a network in presence and absence of external oscillatory drive? In addition, how the interaction between excitation and inhibition contribute to the generation synchronous activities at different balance states is not fully understood.

Here we provide a framework demonstrating how the external oscillations interact with the intrinsic network dynamics and generate synchronization in the networks composed of neurons having type 2 excitability, at different global levels of excitation and inhibition. By systematically varying the synaptic strengths, we demonstrate multiple regimes displaying the heterogeneous network firing patterns and identify two distinct synchronization mechanisms emerging as a function of interplay between excitation and inhibition. Our results show that when the excitatory synaptic strength is relatively low, the resonant oscillations are able to generate the ordered spiking, increase the synchronization and constrain the E/I ratio to be balanced. On the other hand, when the network is strongly connected by higher excitatory synaptic strength values, the global synchronization is generated by the interaction between the internal excitation and inhibition. In addition, although external oscillations modulate the network dynamics at the corresponding parameter range, the effects can be vary-

ing from generating detailed firing pattern within each bursting to modulating the inter-bursting intervals. Our results show that the two synchronous regime emerge at different structural network regimes, and counterintuitively, that the synchrony at low excitatory coupling (w_E) range is dominated by excitation while is dominated by inhibition at high w_E range.

4.2 Methods

4.2.1 Neuron model

The neuron is modeled using modified Hodgkin-Huxley Model with a slow, low-threshold K+ channel. This neuron model displays Type II phase response dynamics, where neurons show phase delay to the input arriving at a relative early phase during spike cycle, and show phase advance when the input arrives at a later phase (*Stiefel et al.*, 2009). The voltage of each neuron changes in the following manner:

$$C\frac{dV_i}{dt} = -g_{Na}m_{\infty}^{3}(V_i)\,h\,(V_i - V_{Na}) - g_{Kdr}n^{4}\,(V_i - V_K) - g_L\,(V_i - V_L) - g_{Ks}z\,(V_i - V_K) + I_i^{drive} - I_i^{syn} \quad (4.1)$$

Each neurons receives a sub-threshold constant current input, which is sampled from a uniform distribution from I_{DC} =[-0.8, 0.8] A/cm^2. In addition, the whole network is fed with a global sine wave with amplitude A=0.3A/cm^2. Thus, the external drive is defined as:

$$I_i^{drive} = I_i^{DC} + Asin\,(\omega t) \quad (4.2)$$

The value is chosen so that all the neurons receive only sub-threshold oscillation even at the top of each cycle. Then each neuron gets Poisson random noise input. Each

ion channels are simulated as below. For Na+ channels:

$$m_{\infty}(V) = \left\{1 + exp\left[\frac{-V - 30.0}{9.5}\right]\right\}^{-1} \tag{4.3}$$

$$\frac{dh}{dt} = \frac{h_{\infty}(V) - h}{\tau_h(V)} \tag{4.4}$$

Where $h_{\infty}(V) = \left\{1 + exp\left[\frac{V+53.0}{7.0}\right]\right\}^{-1}$, and$\tau_h(V) = 0.37+2.78\left\{1 + exp\left[\frac{V+40.5}{6.0}\right]\right\}^{-1}$. The kinetics regular K+ channels are governed by:

$$\frac{dn}{dt} = \frac{n_{\infty}(V) - n}{\tau_n(V)} \tag{4.5}$$

with $n_{\infty}(V) = \left\{1 + exp\left[\frac{-V-30.0}{10.0}\right]\right\}^{-1}$, and $\tau_n(V) = 0.37+1.85\left\{1 + exp\left[\frac{V+27.0}{15.0}\right]\right\}^{-1}$. The slow, low-threshold K+ channels evolve in:

$$\frac{dz}{dt} = \frac{z_{\infty}(V) - z}{75.0} \tag{4.6}$$

With $z_{\infty}(V) = \left\{1 + exp\left[\frac{-V-39.0}{5.0}\right]\right\}^{-1}$.

The leak conductance is given by g_L=0.02mS/cm^2. Other parameters are set to g_{Na}=24.0 mS/cm^2, g_{Kdr}=3.0 mS/cm^2, V_{Na}=55.0mV, V_K=-90.0mV, and V_L=-60.0mV.

4.2.2 Network simulation

The network is composed of 500 cells in a random connectivity, with half neurons being excitatory and the other half inhibitory. The connectivity density is 3% . Although the excitatory to inhibitory cell ratio of excitatory neurons may not be physiological in some brain areas, we have test that this percentage does not affect our results. Therefore, in order to study the relative relationship and contribution

of excitation and inhibition, we choose to keep the symmetry between the excitatory and inhibitory population. The synaptic current transmitted from neuron j to neuron i is modeled as:

$$I_{ij}^{syn} = w * exp\left(-\frac{t - t_j}{\tau}\right)(V_i - E_{syn}) \tag{4.7}$$

w represents the synaptic strength for either excitatory or inhibitory w_I synapses. The values will be changed systematically. t_j refers to the last spiking time of neuron j, and τ is the synaptic constant time with value of 0.5ms, simulating fast AMPA-like excitatory synapses or fast GABA-A-like inhibitory synapses. Reversal potential E_{syn} is set as 0mV for excitatory presynaptic connections and -75ms postsynaptic connections. Eventually the total synaptic input into one neuron is the summation of all the connected presynaptic neurons in Γ_i , $I_i^{syn} = \sum_{j\in\Gamma_i} I_{ij}^{syn}$.

The dynamics of the network evolved for 3 seconds at the time step of 0.05ms, integrated by fourth-order Runge-Kutta method. The results shown are averaged over 3 simulations.

4.2.3 Synchrony measurement

The synchronization of the firing pattern in the network is calculated the averaged fluctuation over all the neurons normalized by the fluctuations of each neuron (*Golomb and Rinzel*, 1994), defined as

$$S_N = \sqrt{\frac{\sigma_V^2}{\frac{1}{N}\sum_{i=1}^{N}\sigma_{V_i}^2}} \tag{4.8}$$

Each spike train is convolved with a Gaussian. We chose to use a small width, the width we chose is about 1/10 of the mean inter-spike interval, intending to capture single spikes more precisely, but the width does not affect the results. Then σ_V^2 is calculated as the variance of the averaged neuronal voltage, while $\sigma_{V_i}^2$ indicates the

variance of the voltage trace for i-th neuron. The values of synchrony lies between 0 and 1, for random firing and perfect synchrony respectively.

4.2.4 Quantification of input dependent spike ordering

When the network displays bursting activity, the timestamps of spikes within each burst are extracted and are offset by the first spiking time in the burst. Neurons with higher driving constant current, I_i^{DC} , are expected to fire earlier in burst, and the relationship turns out to be linear . Then a straight line is fitted in least-squares regression for the relationship between the spike times and the corresponding input current amplitude. The slope with a negative value represents the general temporal difference when neurons having various intrinsic firing properties are recruited. Slope at 0 means that all the neurons are perfectly synchronized with no phase lag. The coefficient of determination R is calculated as

$$R^2 = 1 - \frac{\sum_i (y_i - y)^2}{\sum_i (y_i - f_i)^2} \tag{4.9}$$

where y_i indicates each spiking time with offset, and f_i refers to the corresponding prediction of the fitted line. y is the mean value of the spike data points. R^2 is used as the index of 'cleanness' of the ordered-spiking, with value indicating the perfect linear relationship. The values of the slopes and R values are averaged over all the bursts over the whole simulation time period.

4.3 Results

Here we investigate how changes in relative coupling strength between excitatory and inhibitory sub networks, in presence or absence of external oscillatory drive, affects mechanisms of formation of synchronous oscillations in the network and how does these activity states effect dynamic formation of excitatory/inhibitory balance

in the network.

To study systematically different regimes of connectivity strength, we set the inhibitory synaptic weights (w_I) constant at $0.3mS/cm^2$ while keeping increasing excitatory weights (w_E) from 0 to about 5 times of w_I. We define total excitatory current as sum of all excitatory postsynaptic potentials (EPSP, as defined by equation 4.7) arriving at excitatory and inhibitory cells, and conversely total inhibitory current as sum of inhibitory postsynaptic potentials (IPSP) arriving at both cell populations. We subsequently calculate ratio and difference of these two values. All cells in the network.

4.3.1 Input-dependent resonance property of single neurons

First, the activity of a single neuron in response to sub-threshold oscillatory driving is displayed in Figure 4.1. The response firing rate of the neuron gets much higher when the input frequency is between 3Hz and 12Hz. In particular, the firing frequency and input frequency shows a 1:1 linear relationship between 4Hz-8Hz, indicating that the natural frequency of the neuron shifts depending on the external driving frequency. This property provides the cellular basis for the interaction between the network and the external oscillations.

4.3.2 Total synaptic current and E/I ratio trajectory under different oscillatory driving conditions

We universally observed that the ratio of excitation and inhibition plotted against the difference between the two, as a function of linear increase of w_E, forms a non-monotonic loop (Figure 4.2a). Initially for weak w_E the E/I ratio rapidly increases with the total current difference increasing at a much slower rate. At the intermediate values of w_E the E/ratio typically decrease while the current difference show shows significant increase. Finally, for high w_E regime the E/I ratio and the current

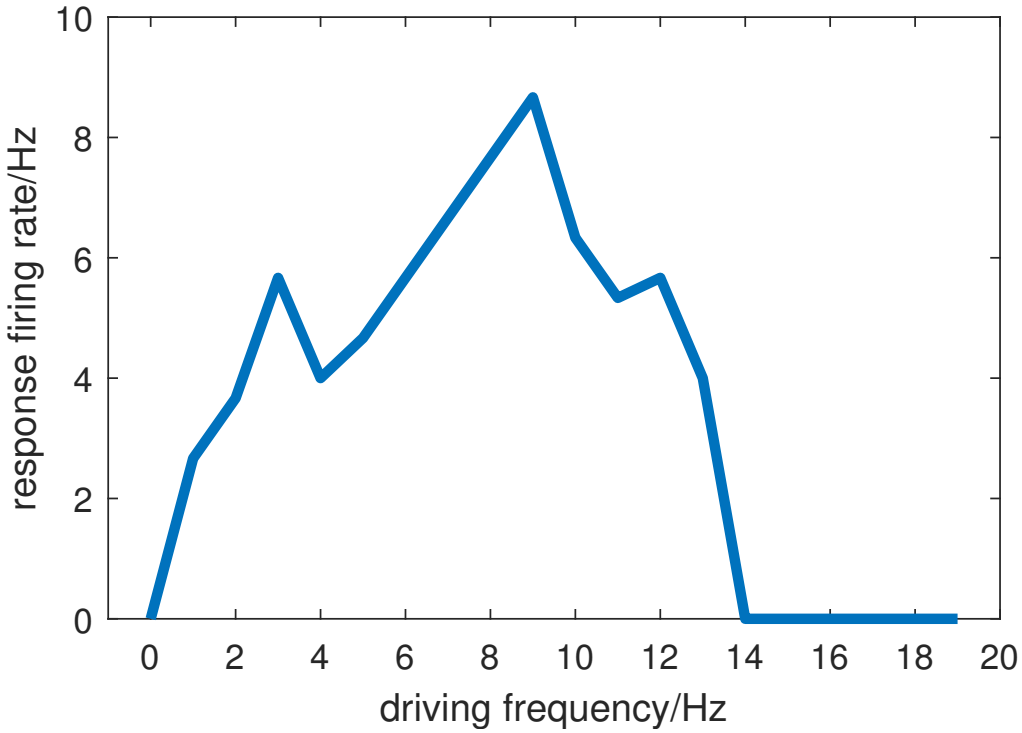

Figure 4.1: Input-dependent resonance property of type II neurons. The firing rate of one single modified Hodgkin-Huxley neuron under sub-threshold oscillatory current driving at different frequencies. I^{DC}=0.5μA , driving amplitude=1μA.

difference rapidly decreases.

Further, the detailed shape of the loop depends on the presence of external oscillatory drive and its frequency (Figure 4.2b). If the driving frequency is between 5-10Hz which is the natural frequency of subthreshold membrane oscillations in that neuronal model be observe a sharp decline in the maximal E/I ratio observed. If the driving oscillations are out of this frequency range the loop converges in shape to the one when no driving oscillation is present. In contrast we observed the that the part of the loop corresponding to high w_E values does not change as a function of frequency of the external oscillatory drive. Thus, in summary, for weak w_E, the emergence of the network oscillatory response is highly dependent on the frequency of oscillatory drive, as are the properties of these network states. In contrast for

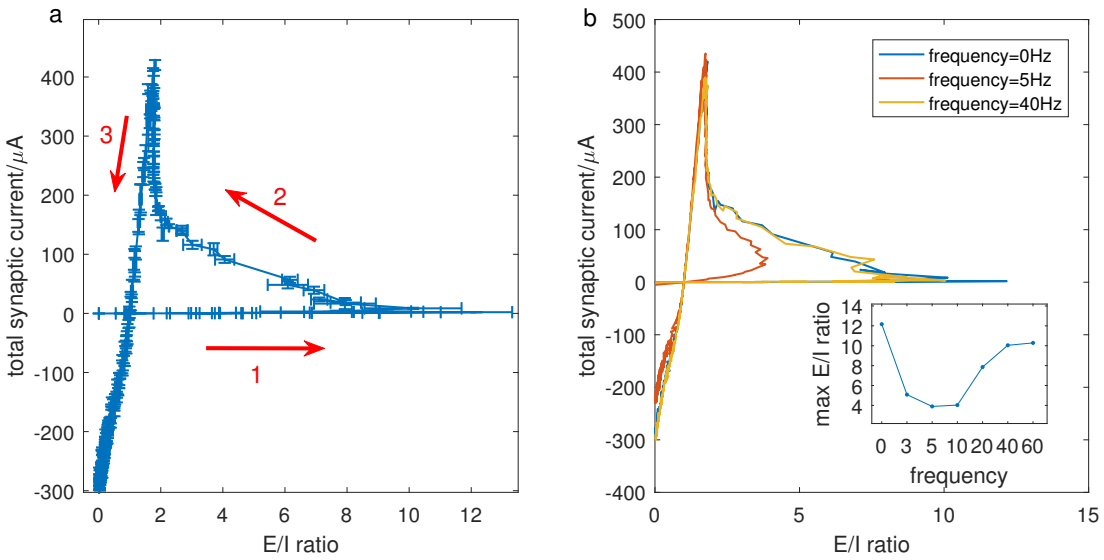

Figure 4.2: Total synaptic current and E/I ratio trajectory when w_E keeps increasing. The inhibitory synaptic strength w_I is fixed as 0.3 mS/cm^2 while the excitatory synaptic strength w_E is increased from 0 up to 2mS/cm^2. (a) E/I ratio trajectory for no oscillatory stimulation. The arrows represent the direction of the evolvement of the curve when w_E increases, in the order of the labeled numbers. (b) E/I ratio trajectories when external oscillations at resonant frequency 5Hz and non-resonant frequency 40Hz are applied to the network. (Inset) The maximum E/I ratio on each trajectory curve under oscillatory stimulation at different frequencies. The results are averaged over 3 simulations.

higher w_E the emergent synchronous oscillations are independent of the oscillatory drive. This suggests that cellular resonance with oscillatory drive plays an important role for week w_E coupling while other mechanism synchronizes the network for high w_E. Therefore, we divide the dynamics into two regimes: resonance regime before the second turning point, and network driven regime after the second turning point. Next we will show the detailed dynamics and mechanisms for the two regimes.

4.3.3 Cellular resonance in weak excitatory coupling regime

We first investigated the dynamical E/I ratio and spatio-temporal activity patterns for weak w_E, at different external driving frequencies. We measured the level of

synchrony in the network, and depicted it as a color of the curve. The frequency of the driving oscillation was varied between 0Hz (no oscillation) and 40Hz. When no oscillation was present and at 40Hz driving, the horizontal extent of the loop is the largest (i.e. maximal E/I ratio is achieved) and the synchrony starts appearing on the return phase of the loop. On the other hand, when the driving signal is a 5Hz oscillation the network fires at a intermediate synchrony level (0.6) and the horizontal extend (i.e. the maximal E/I ratio, see inset Figure 4.3b) of loop is significantly reduced. Being highly frequency dependent (see inset Figure 4.2b), we identify this region as a resonant regime.

We next investigated network-wide pattern formation as a function of the parametric position on the loop. To better depict the spatio-temporal patterning within the network, we display raster plots and calculate the burst triggered averages of excitatory and inhibitory currents in the network, for two w_E values, and for three oscillation frequencies (0Hz, 5Hz, 40Hz). When the w_E is weak, (w_E =0.08mS/cm^2; Figure 4.3 panels b, c, d show the raster plots and panels e, f, g show the current traces, with blue indicating excitatory and red indicating inhibitory cells/traces respectively), the spiking at 0Hz (no oscillatory driving) and 40Hz is sparse and random. At the same time, 5Hz oscillation has an evident effect on increasing the firing rates of the neurons and the network synchrony by regulating the phase locking of spikes to the specific oscillatory phase. Moreover, specifically in this regime, the phase of the locking systematically varies from cell to cell and depends on the constant current, I_i^{DC}, that is fed to the cell (see methods). We adjust the y-axis of the raster plots so that the cell order is a monotonic function of the I_i^{DC}. This potentially provides additional information about the relative magnitude individual cell input and may underlie network structural reorganization if spike timing dependent plasticity is present. The analysis of burst triggered current averages (Figure 4.3d,e,f) reveal that within this regime the dynamics is driven by resonant activation of excitatory

cells with inhibitory activation being significantly weaker. As we move along the loop to region having higher excitatory weight, w_E=0.24mS/cm^2 (Figure 4.3 panels b-d raster plots and panels e-g burst trigger current averages), the resonance mechanism gives way as spontaneous bursting pattern starts to form for no oscillation (panel g) and 40Hz driving (panel i). In this case however, the w_E is still relatively weak, and the current trace show that the inhibitory current is still relatively weak as compared to the excitatory one. This indicates that the synchrony emerges via intrinsic cellular mechanisms rather than PING like effect where it is mediated via inhibition-mediated brief global shut down of cell activity. Here however still the spiking pattern of individual cells are phase-locked to the 5Hz oscillatory driving. In this regime, the network dynamics is still dominated by excitatory activity with the magnitude of the total excitatory current being significantly higher than the inhibitory one.

4.3.4 Highly synchronized dynamics generated by PING-like mechanism

As we keep increasing w_E the network enters second regime: network-driven synchrony mediated via strongly activated inhibition. Here the role of the oscillatory drive diminishes as the three curves merge around the second turning point, except for the phase locking of spiking activity to the oscillator drive at 5Hz. This indicates that at high w_E values, resonance effect of individual cells with the oscillatory drive becomes less important as the network internal interactions dominate the dynamics. While the degree of synchrony is remains high in this regime, the network-wide firing pattern is different. The representative raster plots and current traces are demonstrated on Figure 4.4, panels b-g. When excitatory weight, w_E =0.66mS/cm^2, the system is around the second turning point, the magnitude of inhibition start to catch up with that of the excitation. While it still cannot rapidly shut down the excitation allowing for wide, multi-spike bursts to persist, one can observe that the tight correlation between inhibitory and excitatory currents emerge.

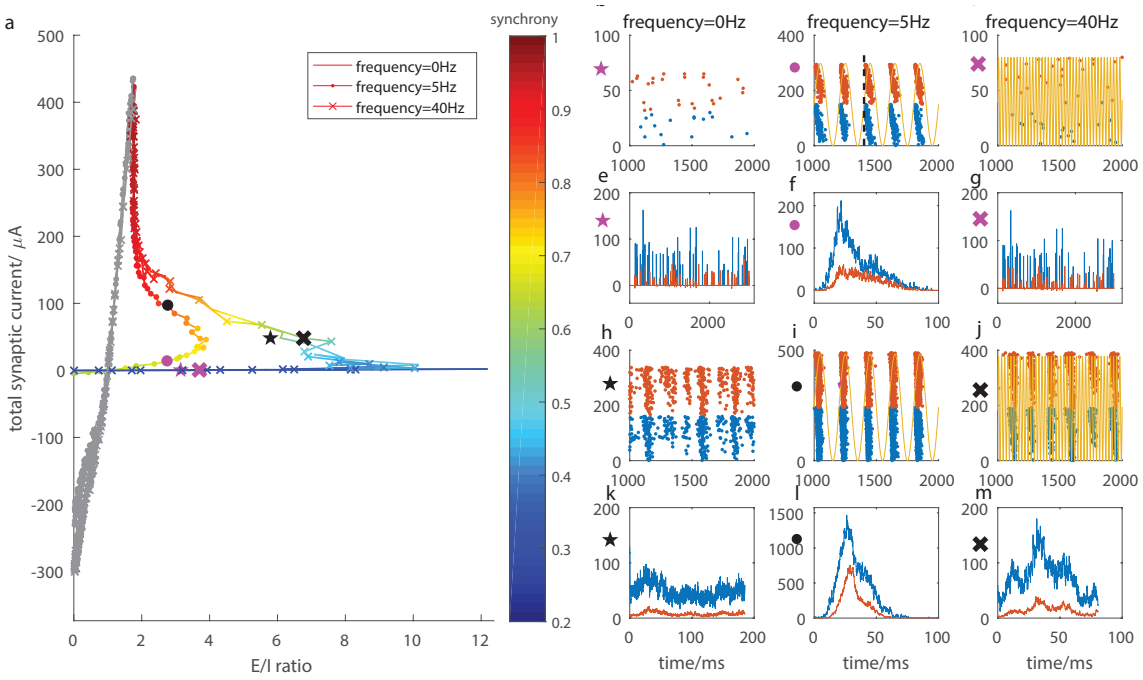

Figure 4.3: Network dynamics in resonance regime. (a) E/I ratio trajectories under no oscillation (plain curve), natural frequency oscillation at 5Hz (with dot marker), and out of resonance frequency at 40Hz (with cross marker), with the color indicating the network synchrony. (b-m) Representative raster plots and averaged current traces over bursts for the representative data points labeled on the curves in panel (a). Blue represents excitatory cells or excitatory currents, and red represents the inhibitory ones. Two representative data points are chosen for each driving condition, with a weaker w_E =0.08mS/cm^2 (b-g) and a stronger w_E =0.24mS/cm^2 (h-m). (b, e) No oscillation driving with weaker w_E (pink star marker); (c, f) Driving at 5Hz with weaker w_E (pink dot marker). The dashed black vertical line is at the first spiking time of the burst. (d, g) Driving at 40Hz with weaker w_E (pink cross marker); (h, k) No oscillation driving with stronger w_E (black star marker); (i, l) Driving at 5Hz with stronger w_E (black dot marker); (j, m) Driving at 40Hz with stronger w_E (black cross marker). Note: (e) and (g) are the excitatory and inhibitory current traces over the whole simulation period since no bursting activity emerges.

For higher values of excitatory coupling, w_E =0.84mS/cm^2, the network goes furthermore towards the inhibition-dominant regime. Here, not only the firing pattern is highly synchronous, but also each burst is composed of multiple single bursts. The interaction between excitatory and inhibitory currents is demonstrated on panel k, l, m explains the mechanism for synchrony. At the beginning of each burst, excitatory current increases first. This burst of excitation leads to strong burst of inhibition (at the peaks, the inhibitory current has typically higher magnitude than the excitatory one) that momentarily hyperpolarizes the excitatory cells, as the excitatory cell recover another excitatory burst is generated which again is followed by the inhibitory activation. Thus here the synchrony is mediated by inhibition burst rather than by individual cell resonance. This fits the PING-mechanism.

4.3.5 Patterns of the temporal relationship between excitatory and inhibitory currents is modulated by oscillation under different E/I regime

Next we focus on evolution of the temporal relationship between the excitatory and inhibitory currents as w_E is monotonically increasing (Figure 4.5), in presence and absence of oscillatory drive. Namely, we calculate cross-correlation between the two first in 1s window (Figure 4.5a, b and c), then we investigate more closely tight temporal locking within 60ms window (Figure 4.5d,e,f). From top to bottom of the correlation maps, w_E monotonically increases, resulting in the different E/I ratios within the network. The horizontal lines on the correlation map mark the corresponding locations on the excitation/inhibition trajectory as marked with star markers on Figure 4.5g,h,I moving counter-clock wise.

At the weakest w_E coupling strength range (i.e. the area above the first separation line which also corresponds to the initial part of the E/I ratio trajectory), no correlation patterns are observed when no external oscillation is present (Figure 4.5

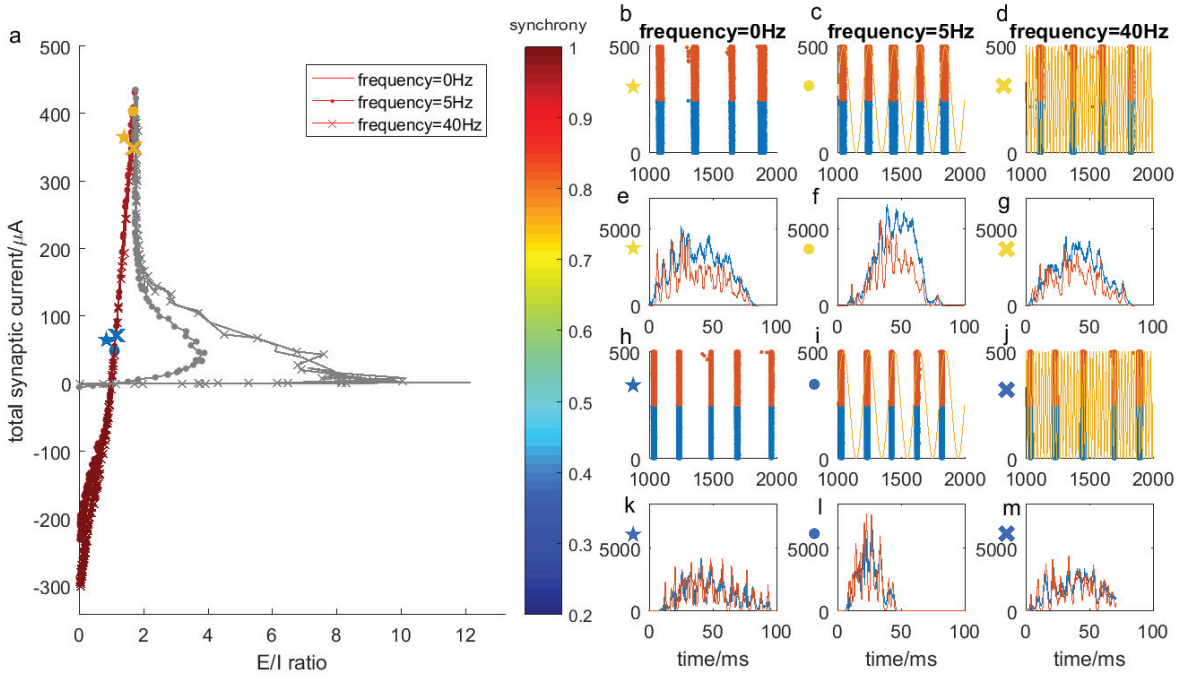

Figure 4.4: Network dynamics of synchrony regime driven by PING mechanism. Similar arrangement of representative raster plots and current trace plots as in Figure 4.3. (a) E/I ratio trajectories, focusing on the second part (colored). Similarly, two representative data points are chosen for each driving condition, with a weaker w_E =0.66mS/ cm^2 and a stronger w_E =0.84mS/cm^2. (b, e) No oscillation driving with weaker w_E (yellow star marker); (c, f) Driving at 5Hz with weaker w_E (yellow dot marker); (d, g) Driving at 40Hz with weaker w_E (yellow cross marker); (h, k) No oscillation driving with stronger w_E (blue star marker); (i, l) Driving at 5Hz with stronger w_E (blue dot marker); (j, m) Driving at 40Hz with stronger w_E (blue cross marker).

a,d) nor at 40Hz oscillatory driving (Figure 4.5 c, f) Due to low excitatory input the network exhibits sparse random spiking. At the same time, under 5Hz driving, the network activity is locked to the external oscillation and periodic temporal correlations emerge. As before, the current fed into each neuron is controlled to be subthreshold indicating that, in this regime, the resonant driving effectively recruits the firing at the during each cycle of the sinusoidal wave. The correlation peak is broad indicating slow activation without detailed spatio-temporal features.

When w_E is increased, the excitation is strong enough to activate the inhibition, thus bring the E/I ratio to decrease causing the E/I trajectory to pass through the first turning point (Figure 4.5g). Between the first and second horizontal line, corresponding to first and second marker (Figure 4.5g-i), periodic correlation pattern spontaneously (i.e. without external oscillatory driving) appears (Figure 4.5a-f). In this regime, we observe dynamic interaction between resonance and spontaneous oscillatory bursting mode. When the network is driven by an oscillation at resonant frequency the inter-burst intervals are stabilized to 200ms corresponding the period of 5Hz oscillation (Figure 4.5b), while in the non-resonant regime (i.e. no oscillatory drive or 40Hz drive) the intervals change their length monotonically with the increase of w_E (Figure 4.5a, c). Furthermore, the correlation between two oscillatory cycles is higher indicating more robust and systematic network activation (Figure 4.5b, a, c). These two features indicate that the external oscillation at natural neuronal firing frequency is able to stabilize the firing pattern independently of changes of synaptic strength.

With further increase of w_E to values corresponding to regime around the third marker, the system enters the network-driven PING regime and the trajectory undergoes the second turning point. Here, while we continue to observe stabilization of inter-burst frequency during the resonant driving, the detailed temporal intra-burst pattern emerges with a cross-frequency phase coupling between the theta band (about

5Hz) and fast gamma band (about 160Hz). This indicates large degree of synchrony within and between the excitatory and inhibitory populations. Furthermore, this pattern in now independent of the oscillatory drive.

4.3.6 Resonance effects of oscillatory driving at various balance states

To better identify the E/I mediated interaction between resonant regime and spontaneous PING-mediated bursting, we quantify dynamic network properties as a function of forcing frequencies. We choose five representative w_E values at which we quantify the firing patterns (Figure 4.6a). These points correspond to: 1) no excitatory connections (blue), 2) a weak w_E when the oscillation has significant impact on the network firing (red), 3) around the first turning point where inhibition gets activated (yellow), 4) around the second turning point where the system transitions from resonant to PING regime (violet), and finally, 5) the network is strongly connected (high w_E , green). Figure 4.6b, c, d depict changes in the network firing rate, the degree of spiking phase ordering within the burst, as a function of constant input I_i^{DC} (see Methods) and its average coefficient of determination R^2 (see Methods), respectively. We observe, that for weak coupling regime (i.e. small w_E), when the network is driven by the oscillations around the natural frequency (3Hz, 5Hz, 10Hz) it displays not only increased firing (Figure 4.6b) but also highly ordered neuronal recruitment, based on the intrinsic cell excitability (i.e. I_i^{DC} magnitude) (Figure 4.6c, 6d). This input dependent recruitment indicates the emergence of temporal code that carries network-wide information about relative magnitude of cell excitability and may subsequently drive structural network reorganization if spike timing dependent plasticity (STDP) is present. For non-resonant frequencies (40Hz, 60Hz) this effect is absent. The oscillation mediated ordered-spiking is particularly prominent at the weakest w_E (blue line), indicating that this effect is gradually weakened by stronger network excitatory/inhibitory interactions. Around the first turning point

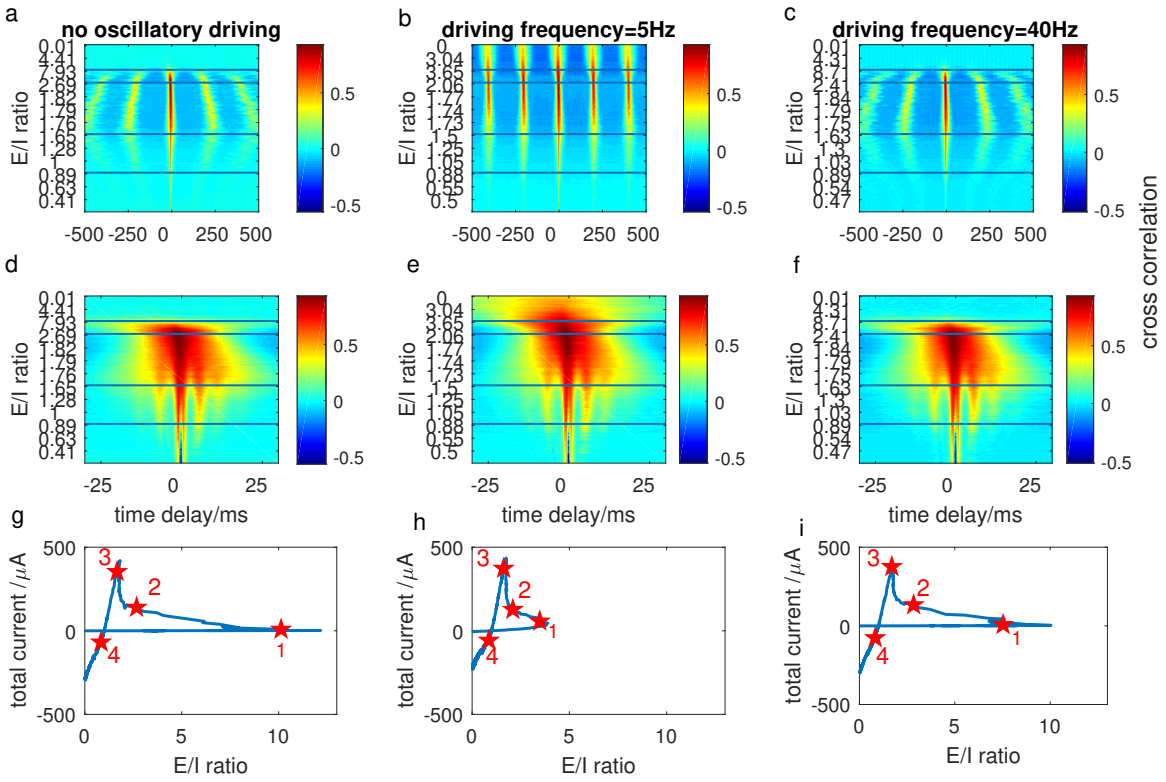

Figure 4.5: Excitatory and inhibitory synaptic currents temporal correlation. Panel a, b, c display the cross correlation map between network excitatory and inhibitory currents for no oscillation, 5Hz, 40Hz driving respectively, with panel d, e, f showing the details in the time delay range of [-30, 30]ms. X-axis represents the time delay between the two currents, where negative values represent the excitation leading the inhibition. w_E increases in the direction from top to bottom, with the E/I ratio indicated on Y-axis. Horizontal lines split the map into 5 parts with different correlation patterns. The E/I ratio trajectories for the three driving conditions are shown in panel g, h, i, plotted in the same way as in Figure 4.2. Each horizontal line corresponds to a star marker with labeled number on the curve.

(yellow), firing rate also displays noticeable resonance effect (Figure 4.6b), but the spike ordering is diminished significantly (Figure 4.6c). At the same time, we observe that the resonance still mediates tight phase locking to oscillation indicated by the peak value of R^2 (Figure 4.6d). For stronger magnitude of w_E, when PING bursting regime emerges (violet and green), changing frequencies of external oscillatory driving do not make affect intra-burst spike dynamics (Figure 4.6b, c, d). The much higher firing rate at w_E around the second turning point (Figure 4.6b violet) is resulting from the wide bursts which contain random firing, in comparison to the lower firing rate of single spike bursting (Figure 4.6b green).

4.4 Discussion

Here we use a biophysical model with recurrently-connected excitatory and inhibitory neurons and investigate the co-existence of synchronization regimes as a function of changing levels of excitatory/inhibitory balance. By systematically varying synaptic strength, the network excitation/inhibition level forms a non-monotonic trajectory in the current-vs-ratio 2D map (Figure 4.2). The obtained results provide insight on possible network transitions between the dynamic states through neuromodulatory regulation, providing a mechanistic understanding for the coexistence of multiple communication schemes in the hierarchical organization of the brain (*Hahn et al.*, 2018). Specifically we investigate the effects of oscillatory driving on the recurrent connectivity network composed of cells that exhibit subthreshold 5Hz membrane oscillation. With increasing strength of synaptic coupling, the system gradually transitions through distinct communication regimes (listed in order of increasing w_E): 1) ordered, input dependent spiking resonantly driven by external oscillatory drive, 2) synchronous phase locked network firing modulated via resonant external oscillatory drive, 3) PING mediated gamma/theta cross frequency coupling, 4) highly-synchronous single bursting oscillation. The first two regimes are driven and/or

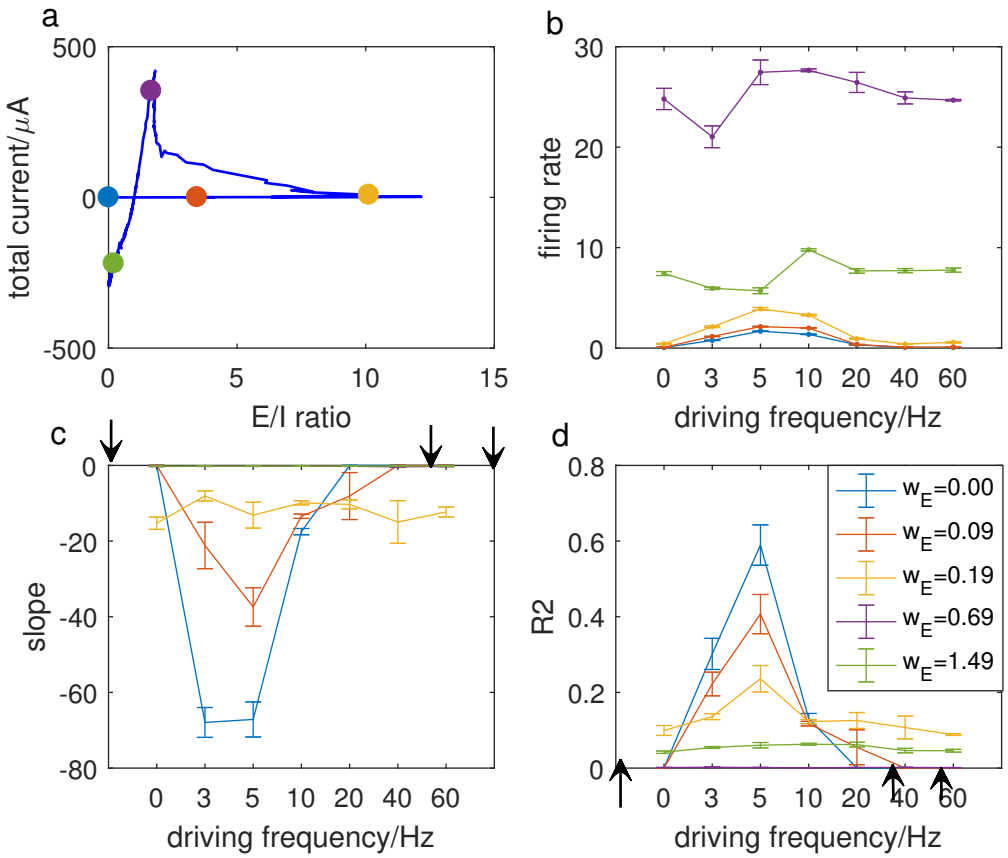

Figure 4.6: Resonance effects in network dynamics at various balance states. (a) E/I ratio trajectory under no oscillatory driving with the locations of 5 representative data points. 5 data points are chosen with w_E increases in the order of blue, red, yellow, violet, green. (b) The firing rates under different driving frequencies are quantified at each w_E value. The index of ordered spiking is quantified by the slope (panel c) and R2 (panel d) of the fitted line of bursting spikes described in the Methods section. Black arrows indicate no data for the slope and R2 when w_E =0 (blue) and 0.09mS/cm^2 (red) at no oscillation, 40Hz and 60Hz driving due to no emergent bursting activity.

mediated by oscillatory resonance of the internal cell subthreshold oscillations and external oscillatory drive and happen for weak w_E. Here, even though the excitatory connectivity is weak, the synchronization is dominated by excitation. The synchrony in last two regimes (high w_E) are mediated by PING mechanism and are dominated by the periodic shunting effect of inhibition.

These results indicate that the system gradually switches from resonance-regime to PING-regime when the network coupling gets stronger. The two turning points on the 2D trajectory correspond to the activation of inhibition and the transition between the two synchronization regimes respectively. In resonance regime the oscillation provides a global readout mechanism for network states represented by individual cells. The activity of cells receiving different magnitude of input is mapped onto their relative spike times. The spontaneous ordered-spiking during sleep or sequential firing of place cells was found in rats hippocampus after spatial learning (*Foster and Wilson*, 2006; *Wikenheiser and Redish*, 2012). Our model predicts that a combination of weak synaptic coupling and resonant activation is necessary for this firing pattern to emerge (Figure 4.6c, d).

When w_E gets stronger, loose oscillatory firing starts to form spontaneously in the network. Here, the external oscillation stabilizes the network oscillatory activity by controlling the inter-bursting interval (Figure 4.5b), which potentially builds a dependable mechanism of precise temporal coding without being affected by the fluctuations in synaptic strengths or other mechanisms influencing instantaneous excitatory/inhibitory balance (Figure 4.5a). Generally in this regime, the oscillation recruits excitation more effectively than inhibition due to the fact that cells are hyperpolarized, resulting in larger distance between mean membrane voltage and excitatory reversal potential that in turn promotes stronger EPSP.

In the other regime characterized by high w_E values, PING emerges with inhibition fully dominating the network synchronization by periodic of the excitatory

activity (Figure 4.4). The random firing within bursts turns into synchronous bursting at a much faster time scale, generating a nested, phasic-coupled theta band and fast gamma band (Figure 4.5d, e). The effect that intrinsically generated gamma band appears within theta band, is proposed to be essential in precise neuronal communication (*Fries*, 2015). Gamma oscillation is thought to play the role of discrete "packets of information" in the inter-regional communication (*Buzsáki and Watson*, 2012; *Akam and Kullmann*, 2014; *Bastos et al.*, 2015). This fast gamma band may be able to carry local information and deliver sequentially via different cycles of the global theta oscillation. The entrainment and modulation of localized gamma band in neocortex of the hippocampus theta oscillation has been largely discovered to contribute to the reciprocal information transfer via temporal coordination (Sirota 2008), item-context associative learning (*Tort et al.*, 2009), or working memory in rat medial prefrontal cortex (*Li et al.*, 2012). With even stronger excitatory coupling, a highly seizure-like bursting appears due to the overwhelming inhibition, implying that the abnormal potentiated excitatory synapses may result in abnormal neural states, which is demonstrated to result from phase coherent currents in neocortex (*Breton et al.*, 2019).

Thus, in summary, our model provides an insight on a dynamical mechanism coordinating various communication schemes, which are mediated by changing relative excitation/inhibition level in the network. We propose that a successful communication process may happen in the following way. When an resonant oscillatory signal arrives to a given local network (or brain modality) which is weakly active and fires randomly, the oscillation provides a readout mechanism of its state by recruiting neurons to fire with stable relative timing. This essentially provides a network wide temporal code of excitation levels of individual cells. The neurons with intrinsically higher excitability fire first, and are able to excite those with lower excitability, strengthening the common synaptic connections via STDP. The increased excitation

mediated via increased structural connectivity drives the system to pass the first turning point on our 2dimesional excitation/inhibition map when enough inhibitory neurons are activated with fast tightly synchronous oscillations starting to emerge - the system starts to generate coherent fast gamma oscillation as well as slow theta band stabilized by external oscillatory drive. The specific cell populations activated by intrinsically emerging gamma oscillation provide detailed informational content that is being transferred to other brain regions via the cross frequency coupling. Finally, if the excitatory synaptic coupling gets even stronger, the system might enter a pathological state with highly synchronized activity.

We thus believe that our results are a good starting point to provide guidance for experimental studies focused on investigating dynamic transitions in a network as a function of changes of relative levels of excitation and inhibition that may happen during memory formation and consolidation.

CHAPTER V

Conclusion

5.1 Summary

This dissertation has focused on understanding the mechanisms underlying functional activity patterns in the context of network structural connectivity and emerging excitatory/inhibitory balance. Presented work has taken on two directions: 1) I participated in the tool development to capture and characterize functional network connectivity patterns (Chapter II) and, 2) I conducted computational modeling to identify the network-level mechanisms for multiple dynamical regimes at different E/I balance states in the context of structural connectivity (Chapter III and IV).

First, in Chapter II the AMD-FuNS framework is extended to quantify the functional connectivity, which outperforms the traditional analysis techniques such as cross-correlation in multiple ways. The AMD algorithm is able to detect the functional relationship between neuron pairs at a more significant level, which is tested on surrogate datasets with various distributions of inter-spike intervals, spiking data generated from network models, as well as in vivo data during memory consolidation. The computation time can reach up to 4 orders of magnitudes shorter than cross correlation for large-scale networks with 10^4 neurons. Bidirectional AMD and unidirectional AMD provide correlation and causality relationship respectively, whereas most traditional metrics are either bidirectional or unidirectional. At the same time

functional network stability (FuNS) reliably assesses the stability of the functional patterns in the network over extended time periods, which bridges the gap between the timescales of neuron activity, at the scale of seconds, and the cognitive behaviors, at the scale of hours. Moreover, FuNS detects the global stability, which is not constrained by the activities of a specific set of neurons, and is capable of alleviating the under-sampling problem in experimental data. This framework provides an efficient and effective approach to detect functional dynamics in the following work.

In the second part of my thesis I develop computational models to investigate the detailed mechanisms for the generation of the diverse functional patterns identified by AMD-FuNS from in vivo data. In Chapter III, the complex interaction between excitation and inhibition is characterized thoroughly in a biophysical neural network where the synaptic strength is varied systematically. I develop a comprehensive picture of the non-monotonic relationship between the total synaptic current and E/I ratio, called E/I ratio trajectory and map it on a 2-dimensional phase space. This relationship shows emergence of three E/I balance regimes that are governed by different mechanisms and display heterogeneous activity patterns. Two competing factors, population firing rate and mean magnitude of postsynaptic potentials, are demonstrated to dominate the network dynamics alternatively in each regime. The framework turns out to be universal, independent of factors including connectivity density, network size, noise input frequency etc. This work potentially explains the diverse or sometimes contradictory experimental results where various types of balance states are observed.

Chapter IV extends upon the work in Chapter III, which focused on a locally connected network composed of neurons having type I membrane excitability, to the mechanisms of the synchronous pattern formation when the network interacts with external oscillatory input and consists of neurons having type 2 membrane excitability. When the synaptic coupling increases, the network gradually shifts from resonance-

based to PING-based synchronization regime. Here the two turning points on the E/I ratio trajectory represent the activation of inhibition and the transition between the two synchronization regimes respectively. Counter-intuitively, the synchronous dynamics is dominated by excitation when excitatory synaptic strength is low, while dominated by inhibition at high excitatory synaptic coupling, further revealing the complex interaction between excitation and inhibition. Thus, the model suggests a potential scheme for efficient information communication between brain regions, where one region transitions from passively receiving rhythmic signals at resonance to actively transferring information with another region when the local coupling is gradually strengthened.

In summary, the work presented here emphasizes the quantification and the mechanisms of the functional dynamics at various E/I states in neural networks. By untangling the complex relationship between the excitation and inhibition, the proposed frameworks provide guidance for future experimental work to identify heterogeneous balance states and synchronization regimes during different cognitive states.

5.2 Future directions

In Chapter III and Chapter IV, the synaptic strength was systematically varied to provide a comprehensive map of the complete relationship. The possible next step would be to add spike-timing-dependent plasticity (STDP) to have the synaptic strength in the network evolve depending on the temporal relationships between the presynaptic and postsynaptic neurons. This would potentially shed light onto modes of network structural reorganization driven by the identified dynamical regimes of their function. The answers to these questions are promising to further extend the insights provided within this work. The question to high importance are: 1) whether the neural plasticity or neuromodulation associated with different cognitive states are able to drive the neural system to transition between different regimes indicated by

the E/I ratio trajectory, specifically, the balance regimes in Type I network (Figure 3.1) and/or the synchronization regimes in Type II network (Figure 4.2)? Whether is it possible for a system, through homeostatic mechanisms, for example during sleep, to return back to the same balance state after experiencing the learning via STDP mechanisms? Previous work has shown that LTP is promoted during wakefulness while LTD is favored during sleep via different levels of neuromodulators such as acetylcholine (*Seol et al.*, 2007). Thus, this will potentially shed light on which E/I balance regime the network sits at during different cognitive states, such as sleep vs wakefulness, and memory formation vs memory retrieval.

In experiments, the excitability types of excitatory and inhibitory neurons are difficult to determine (*Skinner*, 2013). The biological networks are thus likely to contain both types of neurons. Another direction for the future work is to study how the profile of E/I ratio in the network with neurons having mixed types of excitability. The dynamical patterns and the profile of the E/I ratio trajectory for networks composed of excitatory integrators and inhibitory resonators (or excitatory resonators and inhibitory integrators) may further the understanding of the generation mechanisms of cognitively functional network representations.

BIBLIOGRAPHY

BIBLIOGRAPHY

Aertsen, A. M., G. L. Gerstein, M. K. Habib, and G. Palm (1989), Dynamics of neuronal firing correlation: modulation of "effective connectivity", *Journal of Neurophysiology*, *61*(5), 900–917, doi:10.1152/jn.1989.61.5.900.

Akam, T., and D. M. Kullmann (2014), Oscillatory multiplexing of population codes for selective communication in the mammalian brain, *Nature Reviews Neuroscience*, *15*(2), 111–122, doi:10.1038/nrn3668.

Anderson, J. A. (1988), *Neurocomputing: Foundations of Research (v. 1)*, Bradford Books.

Ardid, S., X.-J. Wang, D. Gomez-Cabrero, and A. Compte (2010), Reconciling coherent oscillation with modulationof irregular spiking activity in selective attention:gamma-range synchronization between sensoryand executive cortical areas, *Journal of Neuroscience*, *30*(8), 2856–2870, doi:10.1523/jneurosci.4222-09.2010.

Aru, J., J. Aru, V. Priesemann, M. Wibral, L. Lana, G. Pipa, W. Singer, and R. Vicente (2015), Untangling cross-frequency coupling in neuroscience, *Current Opinion in Neurobiology*, *31*, 51–61, doi:10.1016/j.conb.2014.08.002.

Atallah, B. V., and M. Scanziani (2009), Instantaneous modulation of gamma oscillation frequency by balancing excitation with inhibition, *Neuron*, *62*(4), 566–577, doi:10.1016/j.neuron.2009.04.027.

Axmacher, N., F. Mormann, G. Fernández, C. E. Elger, and J. Fell (2006), Memory formation by neuronal synchronization, *Brain Research Reviews*, *52*(1), 170–182, doi:10.1016/j.brainresrev.2006.01.007.

Axmacher, N., et al. (2010), Cross-frequency coupling supports multi-item working memory in the human hippocampus, *Proc. Natl Acad. Sci USA*, *107*, 3228–3233.

Babapoor-Farrokhran, S., M. Vinck, T. Womelsdorf, and S. Everling (2017), Theta and beta synchrony coordinate frontal eye fields and anterior cingulate cortex during sensorimotor mapping, *Nat Commun*, *8*, 13,967.

Barral, J., and A. D. Reyes (2016), Synaptic scaling rule preserves excitatory-inhibitory balance and salient neuronal network dynamics, *Nat Neurosci*, *19*(12), 1690–1696.

Bassett, D. S., D. L. Greenfield, A. Meyer-Lindenberg, D. R. Weinberger, S. W. Moore, and E. T. Bullmore (2010), Efficient physical embedding of topologically complex information processing networks in brains and computer circuits, *PLoS Comput. Biol*, *6*.

Bassett, D. S., N. F. Wymbs, M. A. Porter, P. J. Mucha, J. M. Carlson, and S. T. Grafton (2011), Dynamic reconfiguration of human brain networks during learning, *Proc Natl Acad Sci U S A.*, *108*(18), 7641–6.

Bastos, A. M., and J.-M. Schoffelen (2016), A tutorial review of functional connectivity analysis methods and their interpretational pitfalls, *Frontiers in Systems Neuroscience*, *9*, doi:10.3389/fnsys.2015.00175.

Bastos, A. M., J. Vezoli, and P. Fries (2015), Communication through coherence with inter-areal delays, *Current Opinion in Neurobiology*, *31*, 173–180, doi:10.1016/j.conb.2014.11.001.

Berg, R. W., A. Alaburda, and J. Hounsgaard (2007), Balanced inhibition and excitation drive spike activity in spinal half-centers, *Science*, *315*(5810), 390–393.

Bhatia, A., S. Moza, and U. S. Bhalla (2019), Precise excitation-inhibition balance controls gain and timing in the hippocampus, *eLife*, *8*, doi:10.7554/elife.43415.

Boccaletti, S., V. Latora, Y. Moreno, M. Chavez, and D. Hwang (2006), Complex networks: Structure and dynamics, *Physics Reports*, *424*(4-5), 175–308, doi:10.1016/j.physrep.2005.10.009.

Bota, M., H.-W. Dong, and L. W. Swanson (2003), From gene networks to brain networks, *Nature Neuroscience*, *6*(8), 795–799, doi:10.1038/nn1096.

Braitenberg, V., and A. Schüz (1991), *Anatomy of the cortex: Statistics and geometry*, Springer-Verlag Publishing, New York, NY, US.

Bressler, S. L., and J. Kelso (2001), Cortical coordination dynamics and cognition, *Trends in Cognitive Sciences*, *5*(1), 26–36, doi:10.1016/s1364-6613(00)01564-3.

Breton, V., B. Bardakjian, and P. Carlen (2019), Phase coherent currents underlying neocortical seizure-like state transitions, *eneuro*, *6*(2), ENEURO.0426–18.2019, doi:10.1523/eneuro.0426-18.2019.

Brovelli, A., et al. (2004), Beta oscillations in a large-scale sensorimotor cortical network: directional influences revealed by granger causality, Proc. Natl Acad. Sci. USA 101, 9849-9854.

Brunel, N. (2000), Dynamics of sparsely connected networks of excitatory and inhibitory spiking neurons, *J Comput Neurosci*, *8*(3), 183–208.

Brunel, N., and X.-J. Wang (2003), What determines the frequency of fast network oscillations with irregular neural discharges? i. synaptic dynamics and excitation-inhibition balance, *Journal of Neurophysiology*, *90*(1), 415–430, doi:10.1152/jn.01095.2002.

Buia, C., and P. Tiesinga (2006), Attentional modulation of firing rate and synchrony in a model cortical network, *Journal of Computational Neuroscience*, *20*(3), 247–264, doi:10.1007/s10827-006-6358-0.

Burns, G. A. P. C., and M. P. Young (2000), Analysis of the connectional organization of neural systems associated with the hippocampus in rats, *Philosophical Transactions of the Royal Society of London. Series B: Biological Sciences*, *355*(1393), 55–70, doi:10.1098/rstb.2000.0549.

Buzsáki, G. (2004a), Neuronal oscillations in cortical networks, *Science*, *304*(5679), 1926–1929, doi:10.1126/science.1099745.

Buzsáki, G. (2004b), Large-scale recording of neuronal ensembles, *Nat Neurosci.*, *7*, 446–451.

Buzsáki, G. (2006), *Rhythms of the Brain*, Oxford University Press.

Buzsáki, G., and X.-J. Wang (2012), Mechanisms of gamma oscillations, *Annual Review of Neuroscience*, *35*(1), 203–225, doi:10.1146/annurev-neuro-062111-150444.

Buzsáki, G., and B. O. Watson (2012), Brain rhythms and neural syntax: implications for efficient coding of cognitive content and neuropsychiatric disease, *Dialogues Clin Neurosci.*, *14*(4), 345—-367.

Buzsáki, G., L. L.-W. S., and C. H. Vanderwolf (1983), Cellular bases of hippocampal EEG in the behaving rat, *Brain Research Reviews*, *6*(2), 139–171, doi:10.1016/0165-0173(83)90037-1.

Börgers, C., and N. Kopell (2003), Synchronization in networks of excitatory and inhibitory neurons with sparse, random connectivity, *Neural Computation*, *15*(3), 509–538, doi:10.1162/089976603321192059.

Caplan, J. B., J. R. Madsen, A. Schulze-Bonhage, R. Aschenbrenner-Scheibe, E. L. Newman, and M. J. Kahana (2003), Human ϑ oscillations related to sensorimotor integration and spatial learning, *The Journal of Neuroscience*, *23*(11), 4726–4736, doi:10.1523/jneurosci.23-11-04726.2003.

Caporale, N., and Y. Dan (2008), Spike timing–dependent plasticity: A hebbian learning rule, *Annual Review of Neuroscience*, *31*(1), 25–46, doi:10.1146/annurev.neuro.31.060407.125639.

Cardin, J. A., L. A. Palmer, and D. Contreras (2007), Stimulus feature selectivity in excitatory and inhibitory neurons in primary visual cortex, *Journal of Neuroscience*, *27*(39), 10,333–10,344, doi:10.1523/jneurosci.1692-07.2007.

Catts, V. S., Y. L. Lai, C. S. Weickert, T. W. Weickert, and S. V. Catts (2016), A quantitative review of the postmortem evidence for decreased cortical n-methyl-d-aspartate receptor expression levels in schizophrenia: How can we link molecular abnormalities to mismatch negativity deficits?, *Biological Psychology*, *116*, 57–67, doi:10.1016/j.biopsycho.2015.10.013.

Cestnik, R., and M. Rosenblum (2017), Reconstructing networks of pulse-coupled oscillators from spike trains, *Physical Review E*, *96*(1), doi: 10.1103/physreve.96.012209.

Chellappa, S. L., G. Gaggioni, J. Q. Ly, S. Papachilleos, C. Borsu, A. Brzozowski, et al. (2016), Circadian dynamics in measures of cortical excitation and inhibition balance, *Sci Rep*, *6*, 33,661.

Cherniak, C., Z. Mokhtarzada, R. Rodriguez-Esteban, and K. Changizi (2004), Global optimization of cerebral cortex layout, *Proceedings of the National Academy of Sciences*, *101*(4), 1081–1086, doi:10.1073/pnas.0305212101.

Chklovskii, D. B., and A. A. Koulakov (2004), MAPS IN THE BRAIN: What can we learn from them?, *Annual Review of Neuroscience*, *27*(1), 369–392, doi: 10.1146/annurev.neuro.27.070203.144226.

Chorev, E., J. Epsztein, A. R. Houweling, A. K. Lee, and M. Brecht (2009), Electrophysiological recordings from behaving animals-going beyond spikes, *Curr. Opin. Neurobiol.*, *19*, 513–519.

Cimenser, A., P. L. Purdon, E. T. Pierce, J. L. Walsh, A. F. Salazar-Gomez, P. G. Harrell, C. Tavares-Stoeckel, K. Habeeb, and E. N. Brown (2011), Tracking brain states under general anesthesia by using global coherence analysis, *Proc Natl Acad Sci U S A*, *108*(21), 8832–7.

Cohen, M. R., and K. A. (2011), Measuring and interpreting neuronal correlations, *Nat Neurosci*, *14*(7), 811–9.

Csicsvari, J., B. Jamieson, K. D. Wise, and G. Buzsáki (2003), Mechanisms of gamma oscillations in the hippocampus of the behaving rat, *Neuron*, *37*(2), 311–322, doi: 10.1016/s0896-6273(02)01169-8.

D'Amour, J. A., and F. RC. (2015), Inhibitory and excitatory spike-timing-dependent plasticity in the auditory cortex, *Neuron*, *86*(2), 514–28.

Daoudal, G. (2003), Long-term plasticity of intrinsic excitability: Learning rules and mechanisms, *Learning & Memory*, *10*(6), 456–465, doi:10.1101/lm.64103.

Daumas, S., a. B. F. Hélène Halley, and J.-M. Lassalle (2005), Encoding, consolidation, and retrieval of contextual memory: differential involvement of dorsal ca3 and ca1 hippocampal subregions, *Learn Mem*, *12*(4), 375–82.

Davison, E. N., K. J. Schlesinger, D. S. Bassett, M. E. Lynall, M. B. Miller, S. T. Grafton, and J. M. Carlson (2015), Brain network adaptability across task states, *PLoS Comput Biol*, *11*, 1.

De Vico Fallani, F., J. Richiardi, M. Chavez, and S. Achard (2014), Graph analysis of functional brain networks: practical issues in translational neuroscience, *Philosophical Transactions of the Royal Society B: Biological Sciences*, *369*(1653), 20130,521–20130,521, doi:10.1098/rstb.2013.0521.

Denève, S., and C. K. Machens (2016), Efficient codes and balanced networks, *Nature Neuroscience*, *19*(3), 375–382, doi:10.1038/nn.4243.

Destexhe, A., and E. Marder (2004), Plasticity in single neuron and circuit computations, *Nature*, *431*(7010), 789–795, doi:10.1038/nature03011.

Diesmann, M., M.-O. Gewaltig, and A. Aertsen (1999), Stable propagation of synchronous spiking in cortical neural networks, *Nature*, *402*, 529–533.

Durkin, J., A. K. Suresh, J. Colbath, C. Broussard, J. Wu, M. Zochowski, and S. J. Aton (2017), Cortically coordinated NREM thalamocortical oscillations play an essential, instructive role in visual system plasticity, *Proceedings of the National Academy of Sciences*, *114*(39), 10,485–10,490, doi:10.1073/pnas.1710613114.

Eguíluz, V. M., D. R. Chialvo, G. A. Cecchi, M. Baliki, and A. V. Apkarian (2005), Scale-free brain functional networks, *Physical Review Letters*, *94*(1), doi:10.1103/physrevlett.94.018102.

Ekstrom, A. D., J. B. Caplan, E. Ho, K. Shattuck, I. Fried, and M. J. Kahana (2005), Human hippocampal theta activity during virtual navigation, *Hippocampus*, *15*(7), 881–889, doi:10.1002/hipo.20109.

Engel, A. K., P. Fries, and W. Singer (2001), Dynamic predictions: Oscillations and synchrony in top–down processing, *Nature Reviews Neuroscience*, *2*(10), 704–716, doi:10.1038/35094565.

Ermentrout, B. (1996), Type i membranes, phase resetting curves, and synchrony, *Neural Computation*, *8*(5), 979–1001, doi:10.1162/neco.1996.8.5.979.

Ermentrout, G. B., and N. Kopell (1998), Fine structure of neural spiking and synchronization in the presence of conduction delays, *Proceedings of the National Academy of Sciences*, *95*(3), 1259–1264, doi:10.1073/pnas.95.3.1259.

Feldman, D. E. (2012), The spike-timing dependence of plasticity, *Neuron*, *75*(4), 556–71.

Feldt, S., J. Waddell, V. L. Hetrick, J. D. Berke, and M. Zochowski (2009), Functional clustering algorithm for the analysis of dynamic network data, *Phys Rev E Stat Nonlin Soft Matter Phys*, *79*, 056,104.

Fell, J., and N. Axmacher (2011), The role of phase synchronization in memory processes, *Nature Reviews Neuroscience*, *12*(2), 105–118, doi:10.1038/nrn2979.

Felleman, D. J., and D. C. V. Essen (1991), Distributed hierarchical processing in the primate cerebral cortex, *Cerebral Cortex*, *1*(1), 1–47, doi:10.1093/cercor/1.1.1.

Ferrarelli, F., M. J. Peterson, S. Sarasso, B. A. Riedner, M. J. Murphy, R. M. Benca, P. Bria, N. H. Kalin, and G. Tononi (2010), Thalamic dysfunction in schizophrenia suggested by whole-night deficits in slow and fast spindles, *American Journal of Psychiatry*, *167*(11), 1339–1348, doi:10.1176/appi.ajp.2010.09121731.

Foster, D. J., and M. A. Wilson (2006), Reverse replay of behavioural sequences in hippocampal place cells during the awake state, *Nature*, *440*(7084), 680–683, doi:10.1038/nature04587.

Fries, P. (2005), A mechanism for cognitive dynamics: neuronal communication through neuronal coherence, *Trends in Cognitive Sciences*, *9*(10), 474–480, doi:10.1016/j.tics.2005.08.011.

Fries, P. (2015), Rhythms for cognition: Communication through coherence, *Neuron*, *88*(1), 220–235, doi:10.1016/j.neuron.2015.09.034.

Fries, P., S. Neuenschwander, A. K. Engel, R. Goebel, and W. Singer (2001), Rapid feature selective neuronal synchronization through correlated latency shifting, *Nature Neuroscience*, *4*(2), 194–200, doi:10.1038/84032.

Friston, K., R. Moran, and A. K. Seth (2013), Analysing connectivity with granger causality and dynamic causal modelling, *Current Opinion in Neurobiology*, *23*(2), 172–178.

Friston, K. J., C. D. Frith, P. F. Liddle, and R. S. J. Frackowiak (1993), Functional connectivity: The principal-component analysis of large (PET) data sets, *Journal of Cerebral Blood Flow & Metabolism*, *13*(1), 5–14, doi:10.1038/jcbfm.1993.4.

Froemke, R. C. (2015), Plasticity of cortical excitatory-inhibitory balance, *Annual Review of Neuroscience*, *38*, 195–219.

Fuchs, E. C., et al. (2007), Recruitment of parvalbumin-positive interneurons determines hippocampal function and associated behavior, *Neuron*, *53*(4), 591–604, doi:10.1016/j.neuron.2007.01.031.

Gautam, S. H., T. T. Hoang, K. McClanahan, S. K. Grady, and W. L. Shew (2015), Maximizing sensory dynamic range by tuning the cortical state to criticality, *PLoS Comput Biol*, *11*, 12.

Geisler, C., N. Brunel, and X.-J. Wang (2005), Contributions of intrinsic membrane dynamics to fast network oscillations with irregular neuronal discharges, *Journal of Neurophysiology*, *94*(6), 4344–4361, doi:10.1152/jn.00510.2004.

Gentet, L. J., M. Avermann, F. Matyas, J. F. Staiger, and P. CC. (2010), Membrane potential dynamics of gabaergic neurons in the barrel cortex of behaving mice, *Neuron*, *65*(3), 422–35.

Ghiani, C. A., et al. (2007), Genetic program of neuronal differentiation and growth induced by specific activation of nmda receptors, *Neurochem Res*, *32*(2), 363–76.

Girard, P., J. M. Hupé, and J. Bullier (2001), Feedforward and feedback connections between areas v1 and v2 of the monkey have similar rapid conduction velocities, *Journal of Neurophysiology*, *85*(3), 1328–1331, doi:10.1152/jn.2001.85.3.1328.

Gloveli, T., T. Dugladze, S. Saha, H. Monyer, U. Heinemann, R. D. Traub, M. A. Whittington, and E. H. Buhl (2004), Differential involvement of oriens/pyramidale interneurones in hippocampal network oscillationsin vitro, *The Journal of Physiology*, *562*(1), 131–147, doi:10.1113/jphysiol.2004.073007.

Golomb, D., and J. Rinzel (1994), Clustering in globally coupled inhibitory neurons, *Physica D: Nonlinear Phenomena*, *72*(3), 259–282, doi:10.1016/0167-2789(94)90214-3.

Graupner, M., and R. AD. (2013), Synaptic input correlations leading to membrane potential decorrelation of spontaneous activity in cortex, *J Neurosci*, *33*(38), 15,075–85.

Gray, C. M. (1999), The temporal correlation hypothesis of visual feature integration, *Neuron*, *24*(1), 31–47, doi:10.1016/s0896-6273(00)80820-x.

Gruber, T. (2004), Oscillatory brain activity dissociates between associative stimulus content in a repetition priming task in the human EEG, *Cerebral Cortex*, *15*(1), 109–116, doi:10.1093/cercor/bhh113.

Gu, S., et al. (2015), Controllability of structural brain networks, *Nat Commun*, *6*, 8414.

Gutkin, B. S., and E. GB. (1998), Dynamics of membrane excitability determine interspike interval variability: a link between spike generation mechanisms and cortical spike train statistics, *Neural Comput*, *10*(5), 1047–65.

Hahn, G., A. F. Bujan, Y. Frégnac, A. Aertsen, and A. Kumar (2014), Communication through resonance in spiking neuronal networks, *PLoS Computational Biology*, *10*(8), e1003,811, doi:10.1371/journal.pcbi.1003811.

Hahn, G., A. Ponce-Alvarez, G. Deco, A. Aertsen, and A. Kumar (2018), Portraits of communication in neuronal networks, *Nature Reviews Neuroscience*, *20*(2), 117–127, doi:10.1038/s41583-018-0094-0.

Haider, B., A. Duque, A. R. Hasenstaub, and M. DA. (2006), Neocortical network activity in vivo is generated through a dynamic balance of excitation and inhibition, *J Neurosci*, *26*(17), 4535–45.

Haider, B., M. Hausser, and M. Carandini (2013), Inhibition dominates sensory responses in the awake cortex, *Nature*, *493*(7430), 97–100.

Hasenstaub, A., Y. Shu, B. Haider, U. Kraushaar, A. Duque, and D. A. McCormick (2005), Inhibitory postsynaptic potentials carry synchronized frequency information in active cortical networks, *Neuron*, *47*(3), 423–435, doi: 10.1016/j.neuron.2005.06.016.

Hebb, D. O. (1939), Intelligence in man after large removals of cerebral tissue: Report of four left frontal lobe cases, *J. Gen. Psychol*, *21*, 73–87.

Hebb, D. O. (1949), *The Organization of Behavior: A NEUROPSYCHOLOGICAL THEORY*, John Wiley & Sons, New York, USA.

Hennequin, G., E. J. Agnes, and T. P. Vogels (2017), Inhibitory plasticity: Balance, control, and codependence, *Annual Review of Neuroscience*, *40*(1), 557–579, doi: 10.1146/annurev-neuro-072116-031005.

Hermundstad, A. M., K. S. Brown, D. S. Bassett, and J. M. Carlson (2011), Learning, memory, and the role of neural network architecture, *PLoS Comput Biol*, *7*, 6.

Heron, W. (1957), The pathology of boredom, *Sci. Am.*, *196*(1), 52–56.

Hilscher, M. M., R. N. Leão, S. J. Edwards, K. E. Leão, and K. Kullander (2017), Chrna2-martinotti cells synchronize layer 5 type a pyramidal cells via rebound excitation, *PLOS Biology*, *15*(2), e2001,392, doi:10.1371/journal.pbio.2001392.

Hopfield, J. J. (1982), Neural networks and physical systems with emergent collective computational abilities., *Proceedings of the National Academy of Sciences*, *79*(8), 2554–2558, doi:10.1073/pnas.79.8.2554.

Howard, M. W. (2003), Gamma oscillations correlate with working memory load in humans, *Cerebral Cortex*, *13*(12), 1369–1374, doi:10.1093/cercor/bhg084.

Hu, H., K. Vervaeke, and J. F. Storm (2002), Two forms of electrical resonance at theta frequencies, generated by m-current, h-current and persistent nacurrent in rat hippocampal pyramidal cells, *The Journal of Physiology*, *545*(3), 783–805, doi: 10.1113/jphysiol.2002.029249.

Hutcheon, B., R. M. Miura, and E. Puil (1996), Subthreshold membrane resonance in neocortical neurons, *Journal of Neurophysiology*, *76*(2), 683–697, doi: 10.1152/jn.1996.76.2.683.

Hájos, N., and O. Paulsen (2009), Network mechanisms of gamma oscillations in the CA3 region of the hippocampus, *Neural Networks*, *22*(8), 1113–1119, doi: 10.1016/j.neunet.2009.07.024.

Izhikevich, E. M., N. S. Desai, E. C. Walcott, and F. C. Hoppensteadt (2003), Bursts as a unit of neural information: selective communication via resonance, *Trends in Neurosciences*, *26*(3), 161–167, doi:10.1016/s0166-2236(03)00034-1.

Jacobs, J., M. J. Kahana, A. D. Ekstrom, and I. Fried (2007), Brain oscillations control timing of single-neuron activity in humans, *Journal of Neuroscience*, *27*(14), 3839–3844, doi:10.1523/jneurosci.4636-06.2007.

Jensen, O., and C. D. Tesche (2002), Frontal theta activity in humans increases with memory load in a working memory task, *European Journal of Neuroscience*, *15*(8), 1395–1399, doi:10.1046/j.1460-9568.2002.01975.x.

Jensen, O., B. Gips, T. O. Bergmann, and M. Bonnefond (2014), Temporal coding organized by coupled alpha and gamma oscillations prioritize visual processing, *Trends in Neurosciences*, *37*(7), 357–369, doi:10.1016/j.tins.2014.04.001.

Joglekar, M. R., J. F. Mejias, G. R. Yang, and X.-J. Wang (2018), Inter-areal balanced amplification enhances signal propagation in a large-scale circuit model of the primate cortex, *Neuron*, *98*(1), 222–234.e8, doi:10.1016/j.neuron.2018.02.031.

Jouve, B. (1998), A mathematical approach to the connectivity between the cortical visual areas of the macaque monkey, *Cerebral Cortex*, *8*(1), 28–39, doi:10.1093/cercor/8.1.28.

Kahana, M. J. (2006), The cognitive correlates of human brain oscillations, *Journal of Neuroscience*, *26*(6), 1669–1672, doi:10.1523/jneurosci.3737-05c.2006.

Kandel, E., J. Schwartz, T. Jessell, S. Siegelbaum, and A. Hudspeth (2012), *Principles of Neural Science, Fifth Edition*, McGraw-Hill Education.

Kehrer, C. (2008), Altered excitatory-inhibitory balance in the NMDA-hypofunction model of schizophrenia, *Frontiers in Molecular Neuroscience*, *1*, doi:10.3389/neuro.02.006.2008.

Kerlin, A. M., M. L. Andermann, V. K. Berezovskii, and R. C. Reid (2010), Broadly tuned response properties of diverse inhibitory neuron subtypes in mouse visual cortex, *Neuron*, *67*(5), 858–871, doi:10.1016/j.neuron.2010.08.002.

Klimesch, W., S. Hanslmayr, P. Sauseng, W. Gruber, C. Brozinsky, N. Kroll, A. Yonelinas, and M. Doppelmayr (2005), Oscillatory EEG correlates of episodic trace decay, *Cerebral Cortex*, *16*(2), 280–290, doi:10.1093/cercor/bhi107.

Koch, M. A., D. G. Norris, and M. Hund-Georgiadis (2002), An investigation of functional and anatomical connectivity using magnetic resonance imaging, *NeuroImage*, *16*(1), 241–250, doi:10.1006/nimg.2001.1052.

Kopell, N., G. B. Ermentrout, M. A. Whittington, and R. D. Traub (2000), Gamma rhythms and beta rhythms have different synchronization properties, *Proceedings of the National Academy of Sciences*, *97*(4), 1867–1872, doi:10.1073/pnas.97.4.1867.

Kötter, R., and K. E. Stephan (2003), Network participation indices: characterizing component roles for information processing in neural networks, *Neural Networks*, *16*(9), 1261–1275, doi:10.1016/j.neunet.2003.06.002.

Kumar, A., S. Rotter, and A. Aertsen (2010), Spiking activity propagation in neuronal networks: reconciling different perspectives on neural coding, *Nat Rev. Neurosci.*, *11*, 615–627.

Lakatos, P., et al. (2005), An oscillatory hierarchy controlling neuronal excitability and stimulus processing in the auditory cortex, *J. Neurophysiol.*, *94*, 1904–1911.

Landau, I. D., R. Egger, V. J. Dercksen, M. Oberlaender, and H. Sompolinsky (2016), The impact of structural heterogeneity on excitation-inhibition balance in cortical networks, *Neuron*, *92*(5), 1106–21.

Lau, T., and M. Zochowski (2011), The resonance frequency shift, pattern formation, and dynamical network reorganization via sub-threshold input, *PLoS ONE*, *6*(4), e18,983, doi:10.1371/journal.pone.0018983.

Letzkus, J. J., S. B. Wolff, and L. A. Disinhibition (2015), a circuit mechanism for associative learning and memory, *Neuron*, *88*(2), 264–76.

Leung, L. S., and H.-W. Yu (1998), Theta-frequency resonance in hippocampal CA1 neurons in vitro demonstrated by sinusoidal current injection, *Journal of Neurophysiology*, *79*(3), 1592–1596, doi:10.1152/jn.1998.79.3.1592.

Lewis, D. A., T. Hashimoto, and D. W. Volk (2005), Cortical inhibitory neurons and schizophrenia, *Nature Reviews Neuroscience*, *6*(4), 312–324, doi:10.1038/nrn1648.

Li, S., W. Bai, T. Liu, H. Yi, and X. Tian (2012), Increases of theta-low gamma coupling in rat medial prefrontal cortex during working memory task, *Brain Research Bulletin*, *89*(3-4), 115–123, doi:10.1016/j.brainresbull.2012.07.012.

Lichtman, J. W., J. Livet, and J. R. Sanes (2008), A technicolour approach to the connectome, *Nat Rev. Neurosci.*, *9*, 417–422.

Liu, B., P. Li, Y. Li, Y. J. Sun, Y. Yanagawa, K. Obata, L. I. Zhang, and H. W. Tao (2009), Visual receptive field structure of cortical inhibitory neurons revealed by two-photon imaging guided recording, *Journal of Neuroscience*, *29*(34), 10,520–10,532, doi:10.1523/jneurosci.1915-09.2009.

Llinás, R., U. Ribary, D. Contreras, and C. Pedroarena (1998), The neuronal basis for consciousness, *Philosophical Transactions of the Royal Society of London. Series B: Biological Sciences*, *353*(1377), 1841–1849, doi:10.1098/rstb.1998.0336.

Lorente De No, R. (1938), ANALYSIS OF THE ACTIVITY OF THE CHAINS OF INTERNUNCIAL NEURONS, *Journal of Neurophysiology*, *1*(3), 207–244, doi:10.1152/jn.1938.1.3.207.

Luo, L., E. M. Callaway, and K. Svoboda (2008), Genetic dissection of neural circuits, *Neuron*, *57*, 634–660.

Ly, J. Q., G. Gaggioni, S. L. Chellappa, S. Papachilleos, A. Brzozowski, C. Borsu, et al. (2016), Circadian regulation of human cortical excitability, *Nat Commun*, *7*, 11,828.

Lytton, W. W., and T. J. Sejnowski (1991), Simulations of cortical pyramidal neurons synchronized by inhibitory interneurons, *Journal of Neurophysiology*, *66*(3), 1059–1079, doi:10.1152/jn.1991.66.3.1059.

Mann, E. O., J. M. Suckling, N. Hajos, S. A. Greenfield, and O. Paulsen (2005), Perisomatic feedback inhibition underlies cholinergically induced fast network oscillations in the rat hippocampus in vitro, *Neuron*, *45*(1), 105–117, doi:10.1016/j.neuron.2004.12.016.

McCulloch, W., and W. Pitts (1943), A logical calculus of the ideas immanent in nervous activity, *Bull. Math. Biophys.*, *5*, 115–143.

Medaglia, J. D., F. Pasqualetti, R. H. Hamilton, S. L. Thompson-Schill, and D. S. Bassett (2017), Brain and cognitive reserve: Translation via network control theory, *Neurosci Biobehav Rev*, *75*, 53–64.

Milner, P. M. (1993), The mind and Donald O. Hebb, *Sci. Am.*, *268*(1), 124–129.

Misic, B., and O. Sporns (2016), From regions to connections and networks: new bridges between brain and behavior, *Current Opinion in Neurobiology*, *40*, 1–7.

Monier, C., J. Fournier, and F. Y. (2008), In vitro and in vivo measures of evoked excitatory and inhibitory conductance dynamics in sensory cortices, *J Neurosci Methods*, *169*(2), 323–65.

Mormann, F., K. Lehnertz, P. David, and C. E. Elger (2000), Mean phase coherence as a measure for phase synchronization and its application to the EEG of epilepsy patients, *Physica D: Nonlinear Phenomena*, *144*(3-4), 358–369, doi:10.1016/s0167-2789(00)00087-7.

Murphy, B. K., and K. D. Miller (2009), Balanced amplification: A new mechanism of selective amplification of neural activity patterns, *Neuron*, *61*(4), 635–648, doi:10.1016/j.neuron.2009.02.005.

Nakhnikian, A., G. V. Rebec, L. M. Grasse, L. L. Dwiel, M. Shimono, and J. M. Beggs (2014), Behavior modulates effective connectivity between cortex and striatum, *PLoS One*, *9*, 3.

Naze, S., J. Humble, P. Zheng, S. Barton, C. Rangel-Barajas, G. V. Rebec, and J. R. Kozloski (2018), Cortico-striatal cross-frequency coupling and gamma genesis disruptions in huntington's disease mouse and computational models, *eneuro*, *5*(6), ENEURO.0210–18.2018, doi:10.1523/eneuro.0210-18.2018.

Newman, M. (2010), *Networks: An Introduction*, Oxford University Press.

Newman, M. E. (2004), Fast algorithm for detecting community structure in networks, *Phys. Rev E: Stat. Nonlin. Soft Matter Phys.*, *69*, 066,133.

Newman, M. E. (2006), Finding community structure in networks using the eigenvectors of matrices, *Phys. Rev E: Stat. Nonlin. Soft Matter Phys.*, *74*, 036,104.

Newman, M. E. J. (2001a), Scientific collaboration networks. i. network construction and fundamental results, *Physical Review E*, *64*(1), doi: 10.1103/physreve.64.016131.

Newman, M. E. J. (2001b), Scientific collaboration networks. II. shortest paths, weighted networks, and centrality, *Physical Review E*, *64*(1), doi: 10.1103/physreve.64.016132.

Niell, C. M., and S. MP. (2010), Modulation of visual responses by behavioral state in mouse visual cortex, *Neuron*, *65*(4), 472–9.

Nigam, S., et al. (2016), Rich-club organization in effective connectivity among cortical neurons, *The Journal of Neuroscience*, *36*(3), 670–684, doi: 10.1523/jneurosci.2177-15.2016.

Ognjanovski, N., D. Maruyama, N. Lashner, M. Zochowski, and S. J. Aton (2014), Ca1 hippocampal network activity changes during sleep-dependent memory consolidation, *Front Syst Neurosci.*, *8*, 61.

Ognjanovski, N., S. Schaeffer, J. Wu, S. Mofakham, D. Maruyama, M. Zochowski, and S. J. Aton (2017), Parvalbumin-expressing interneurons coordinate hippocampal network dynamics required for memory consolidation, *Nature Communications*, *8*(1), doi:10.1038/ncomms15039.

Ognjanovski, N., C. Broussard, M. Zochowski, and S. J. Aton (2018), Hippocampal network oscillations rescue memory consolidation deficits caused by sleep loss, *Cerebral Cortex*, *28*(10), 3711–3723, doi:10.1093/cercor/bhy174.

Okun, M., and I. Lampl (2008), Instantaneous correlation of excitation and inhibition during ongoing and sensory-evoked activities, *Nature Neuroscience*, *11*(5), 535–537, doi:10.1038/nn.2105.

Pajevic, S., and D. Plenz (2009), Efficient network reconstruction from dynamical cascades identifies small-world topology of neuronal avalanches, *PLoS Comput Biol*, *5*(1), e1000,271.

Palva, J. M., and S. Palva (2017), Functional integration across oscillation frequencies by cross-frequency phase synchronization, *European Journal of Neuroscience*, *48*(7), 2399–2406, doi:10.1111/ejn.13767.

Park, H.-J., and K. Friston (2013), Structural and functional brain networks: From connections to cognition, *Science*, *342*(6158), 1238,411–1238,411, doi: 10.1126/science.1238411.

Passingham, R. E., K. E. Stephan, and R. Kötter (2002), The anatomical basis of functional localization in the cortex, *Nature Reviews Neuroscience*, *3*(8), 606–616, doi:10.1038/nrn893.

Patel, B., J. Patel, J.-H. Cho, S. Manne, S. Bonala, E. Henske, F. Roegiers, M. Markiewski, and M. Karbowniczek (2015), Exosomes mediate the acquisition of the disease phenotypes by cells with normal genome in tuberous sclerosis complex, *Oncogene*, *35*(23), 3027–3036, doi:10.1038/onc.2015.358.

Petersen, S. E., and O. Sporns (2015), Brain networks and cognitive architectures, *Neuron*, *88*(1), 207–219, doi:10.1016/j.neuron.2015.09.027.

Pike, F. G., R. S. Goddard, J. M. Suckling, P. Ganter, N. Kasthuri, and O. Paulsen (2000), Distinct frequency preferences of different types of rat hippocampal neurones in response to oscillatory input currents, *The Journal of Physiology*, *529*(1), 205–213, doi:10.1111/j.1469-7793.2000.00205.x.

Poil, S. S., R. Hardstone, H. D. Mansvelder, and K. Linkenkaer-Hansen (2012), Critical-state dynamics of avalanches and oscillations jointly emerge from balanced excitation/inhibition in neuronal networks, *Journal of Neuroscience*, *32*(29), 9817–23.

Poli, D., V. P. Pastore, S. Martinoia, and P. Massobrio (2016), From functional to structural connectivity using partial correlation in neuronal assemblies, *Journal of Neural Engineering*, *13*(2), 026,023, doi:10.1088/1741-2560/13/2/026023.

Ponten, S. C., A. Daffertshofer, A. Hillebrand, and C. J. Stam (2010), The relationship between structural and functional connectivity: Graph theoretical analysis of an eeg neural mass model, *NeuroImage*, *52*, 985–994.

Poo, C., and J. S. Isaacson (2009), Odor representations in olfactory cortex: "sparse" coding, global inhibition, and oscillations, *Neuron*, *62*(6), 850–861, doi:10.1016/j.neuron.2009.05.022.

Prescott, S. A., S. Ratté, Y. D. Koninck, and T. J. Sejnowski (2008), Pyramidal neurons switch from integrators in vitro to resonators under in vivo-like conditions, *Journal of Neurophysiology*, *100*(6), 3030–3042, doi:10.1152/jn.90634.2008.

Puentes-Mestril, C., J. Roach, N. Niethard, M. Zochowski, and S. J. Aton (2019), How rhythms of the sleeping brain tune memory and synaptic plasticity, *Sleep*, doi:10.1093/sleep/zsz095.

Puil, E., H. Meiri, and Y. Yarom (1994), Resonant behavior and frequency preferences of thalamic neurons, *Journal of Neurophysiology*, *71*(2), 575–582, doi:10.1152/jn.1994.71.2.575.

Rabinovitch, M. S., and H. E. Rosvold (1951), A closed-field intelligence test for rats., *Canadian Journal of Psychology/Revue canadienne de psychologie*, *5*(3), 122–128, doi:10.1037/h0083542.

Raghavachari, S., M. J. Kahana, D. S. Rizzuto, J. B. Caplan, M. P. Kirschen, B. Bourgeois, J. R. Madsen, and J. E. Lisman (2001), Gating of human theta oscillations by a working memory task, *The Journal of Neuroscience*, *21*(9), 3175–3183, doi: 10.1523/jneurosci.21-09-03175.2001.

Renart, B. P. H. L. P. N. R. A. e. a., A. de la Rocha J (2010), The asynchronous state in cortical circuits, *Science*, *327*(5965), 587–90.

Rizzuto, D. S., J. R. Madsen, E. B. Bromfield, A. Schulze-Bonhage, D. Seelig, R. Aschenbrenner-Scheibe, and M. J. Kahana (2003), Reset of human neocortical oscillations during a working memory task, *Proceedings of the National Academy of Sciences*, *100*(13), 7931–7936, doi:10.1073/pnas.0732061100.

Roach, J. P., A. Pidde, E. Katz, J. Wu, N. Ognjanovski, S. J. Aton, and M. R. Zochowski (2018), Resonance with subthreshold oscillatory drive organizes activity and optimizes learning in neural networks, *Proceedings of the National Academy of Sciences*, *115*(13), E3017–E3025, doi:10.1073/pnas.1716933115.

Rosenblatt, F. (1958), The perceptron: A probabilistic model for information storage and organization in the brain., *Psychological Review*, *65*(6), 386–408, doi: 10.1037/h0042519.

Rubin, R., L. F. Abbott, and H. Sompolinsky (2017), *Balanced Excitation and Inhibition are required for High-Capacity*, Noise-Robust Neuronal Selectivity. arXiv q-bio.

Rubinov, M., and O. Sporns (2010), Complex network measures of brain connectivity: Uses and interpretations, *NeuroImage*, *52*, 1059–1069.

Rudolph, M., M. Pospischil, I. Timofeev, and A. Destexhe (2007), Inhibition determines membrane potential dynamics and controls action potential generation in awake and sleeping cat cortex, *J Neurosci*, *27*(20), 5280–90.

Runyan, C. A., J. Schummers, A. Van Wart, S. J. Kuhlman, N. R. Wilson, Z. J. Huang, et al. (2010), Response features of parvalbumin-expressing interneurons suggest precise roles for subtypes of inhibition in visual cortex, *Neuron*, *67*(5), 847–57.

Rupprecht, P., and R. W. Friedrich (2018), Precise synaptic balance in the zebrafish homolog of olfactory cortex, *Neuron*, *100*(3), 669–683.e5, doi: 10.1016/j.neuron.2018.09.013.

Salinas, E., and T. P. (2000), Gain modulation a major computational principle of the central nervous system, *Neuron*, *27*(1), 15–21.

Sanhueza, M., and J. Bacigalupo (2005), Intrinsic subthreshold oscillations of the membrane potential in pyramidal neurons of the olfactory amygdala, *European Journal of Neuroscience*, *22*(7), 1618–1626, doi:10.1111/j.1460-9568.2005.04341.x.

Scannell, J. (1999), The connectional organization of the cortico-thalamic system of the cat, *Cerebral Cortex*, *9*(3), 277–299, doi:10.1093/cercor/9.3.277.

Scannell, J. W., S. Grant, B. R. Payne, and R. Baddeley (2000), On variability in the density of corticocortical and thalamocortical connections, *Philosophical Transactions of the Royal Society of London. Series B: Biological Sciences*, *355*(1393), 21–35, doi:10.1098/rstb.2000.0547.

Schnitzler, A., and J. Gross (2005), Normal and pathological oscillatory communication in the brain, *Nature Reviews Neuroscience*, *6*(4), 285–296, doi:10.1038/nrn1650.

Scholl, D. A. (1956), *The Organization of the Cerebral Cortex*, John Wiley, Oxford, England.

Scott, A. (2002), *Neuroscience: A Mathematical Primer*, Springer New York, doi:10.1007/b98897.

Sederberg, P. B., M. J. Kahana, M. W. Howard, E. J. Donner, and J. R. Madsen (2003), Theta and gamma oscillations during encoding predict subsequent recall, *The Journal of Neuroscience*, *23*(34), 10,809–10,814, doi:10.1523/jneurosci.23-34-10809.2003.

Senden, M., G. Deco, M. A. de Reus, R. Goebel, and M. P. van den Heuvel (2014), Rich club organization supports a diverse set of functional network configurations, *NeuroImage*, *96*, 174–182, doi:10.1016/j.neuroimage.2014.03.066.

Seol, G. H., J. Ziburkus, S. Huang, L. Song, I. T. Kim, K. Takamiya, R. L. Huganir, H.-K. Lee, and A. Kirkwood (2007), Neuromodulators control the polarity of spike-timing-dependent synaptic plasticity, *Neuron*, *55*(6), 919–929, doi:10.1016/j.neuron.2007.08.013.

Shen, K., R. M. Hutchison, G. Bezgin, S. Everling, and A. R. McIntosh (2015), Network structure shapes spontaneous functional connectivity dynamics, *Journal of Neuroscience*, *35*(14), 5579–88.

Shepard, R. N. (1980), Multidimensional scaling, tree-fitting, and clustering, *Science*, *210*(4468), 390–398, doi:10.1126/science.210.4468.390.

Shimono, M., and J. M. Beggs (2015), Functional clusters, hubs, and communities in the cortical microconnectome, *Cereb Cortex*, *25*(10), 3743–57.

Shu, Y., A. Hasenstaub, and M. DA. (2003), Turning on and off recurrent balanced cortical activity, *Nature*, *423*(6937), 288–93.

Skilling, Q. M., D. Maruyama, N. Ognjanovski, S. Aton, and M. Zochowski (2017), Criticality, *stability, competition, and consolidation of new representations in brain networks.*

Skinner, F. K. (2013), Moving beyond type i and type II neuron types, *F1000Research*, *2*, 19, doi:10.12688/f1000research.2-19.v1.

Somogyi, P., G. Tamás, R. Lujan, and E. H. Buhl (1998), Salient features of synaptic organisation in the cerebral cortex1, *Brain Research Reviews*, *26*(2-3), 113–135, doi:10.1016/s0165-0173(97)00061-1.

Song, S., K. D. Miller, and L. F. Abbott (2000), Competitive hebbian learning through spike-timing-dependent synaptic plasticity, *Nature Neurosci*, *3*, 919–926.

Spencer, K. M., P. G. Nestor, M. A. Niznikiewicz, D. F. Salisbury, M. E. Shenton, and R. W. McCarley (2003), Abnormal neural synchrony in schizophrenia, *The Journal of Neuroscience*, *23*(19), 7407–7411, doi:10.1523/jneurosci.23-19-07407.2003.

Sporns, O., and R. Kötter (2004), Motifs in brain networks, *PLoS Biology*, *2*(11), e369, doi:10.1371/journal.pbio.0020369.

Sporns, O., G. Tononi, and G. M. Edelman (2000), Theoretical neuroanatomy: Relating anatomical and functional connectivity in graphs and cortical connection matrices, *Cerebral Cortex*, *10*(2), 127–141.

Sporns, O., D. Chialvo, M. Kaiser, and C. Hilgetag (2004), Organization, development and function of complex brain networks, *Trends in Cognitive Sciences*, *8*(9), 418–425, doi:10.1016/j.tics.2004.07.008.

Stafford, J. M., et al. (2014), Large-scale topology and the default mode network in the mouse connectome, *Proc. Natl Acad. Sci. U S A*, *111*(52), 18,745–50.

Stam, C. (2004), Functional connectivity patterns of human magnetoencephalographic recordings: a 'small-world' network?, *Neuroscience Letters*, *355*(1-2), 25–28, doi:10.1016/j.neulet.2003.10.063.

Stephan, K. E., L. Kamper, A. Bozkurt, G. A. P. C. Burns, M. P. Young, and R. Kötter (2001), Advanced database methodology for the collation of connectivity data on the macaque brain (CoCoMac), *Philosophical Transactions of the Royal Society of London. Series B: Biological Sciences*, *356*(1412), 1159–1186, doi:10.1098/rstb.2001.0908.

Steriade, M. (2001), Impact of network activities on neuronal properties in corticothalamic systems, *J. Neurophysiol.*, *86*, 1–39.

Stettler, D. D., and R. Axel (2009), Representations of odor in the piriform cortex, *Neuron*, *63*(6), 854–64.

Stiefel, K., B. Gutkin, and T. Sejnowski (2009), The effects of cholinergic neuromodulation on neuronal phase-response curves of modeled cortical neurons, *Journal of Computational Neuroscience*, *26*, 289–301.

Sugino, K., C. M. Hempel, M. N. Miller, A. M. Hattox, P. Shapiro, C. Wu, Z. J. Huang, and S. B. Nelson (2005), Molecular taxonomy of major neuronal classes in the adult mouse forebrain, *Nature Neuroscience*, *9*(1), 99–107, doi:10.1038/nn1618.

Sun, Y. J., Y. J. Kim, L. A. Ibrahim, T. Hzw, and Z. LI. (2013), Synaptic mechanisms underlying functional dichotomy between intrinsic-bursting and regular-spiking neurons in auditory cortical layer 5, *Journal of Neuroscience*, *33*(12), 5326–39.

Supekar, K., V. Menon, D. Rubin, M. Musen, and M. Greicius (2008), Network analysis of intrinsic functional brain connectivity in alzheimer's disease, *PlOS Comp Biology*, *4*(6), e1000,100.

Takada, Y., M. Hirano, S. Kiyonaka, Y. Ueda, K. Yamaguchi, K. Nakahara, M. X. Mori, and Y. Mori (2015), Rab3 interacting molecule 3 mutations associated with autism alter regulation of voltage-dependent ca2 channels, *Cell Calcium*, *58*(3), 296–306, doi:10.1016/j.ceca.2015.06.007.

Tan, A., S. Andoni, and N. Priebe (2013), A spontaneous state of weakly correlated synaptic excitation and inhibition in visual cortex, *Neuroscience*, *247*, 364–375, doi:10.1016/j.neuroscience.2013.05.037.

Tatti, R., M. S. Haley, O. K. Swanson, T. Tselha, and A. Maffei (2017), Neurophysiology and regulation of the balance between excitation and inhibition in neocortical circuits, *Biological Psychiatry*, *81*(10), 821–831, doi:10.1016/j.biopsych.2016.09.017.

Tervonen, T. A., V. Louhivuori, X. Sun, M.-E. Hokkanen, C. F. Kratochwil, P. Zebryk, E. Castrén, and M. L. Castrén (2009), Aberrant differentiation of glutamatergic cells in neocortex of mouse model for fragile x syndrome, *Neurobiology of Disease*, *33*(2), 250–259, doi:10.1016/j.nbd.2008.10.010.

Thompson, W. R., and W. Heron (1954), The effects of restricting early experience on the problem-solving capacity of dogs., *Canadian Journal of Psychology/Revue canadienne de psychologie*, *8*(1), 17–31, doi:10.1037/h0083595.

Tiesinga, P., and T. J. Sejnowski (2009), Cortical enlightenment: Are attentional gamma oscillations driven by ING or PING?, *Neuron*, *63*(6), 727–732, doi:10.1016/j.neuron.2009.09.009.

Tong, X.-J., Z. Hu, Y. Liu, D. Anderson, and J. M. Kaplan (2015), A network of autism linked genes stabilizes two pools of synaptic GABAA receptors, *eLife*, *4*, doi:10.7554/elife.09648.

Tort, A. B. L., R. W. Komorowski, J. R. Manns, N. J. Kopell, and H. Eichenbaum (2009), Theta-gamma coupling increases during the learning of item-context associations, *Proceedings of the National Academy of Sciences*, *106*(49), 20,942–20,947, doi:10.1073/pnas.0911331106.

Traub, R. D., M. A. Whittington, I. M. Stanford, and J. G. R. Jefferys (1996), A mechanism for generation of long-range synchronous fast oscillations in the cortex, *Nature*, *383*(6601), 621–624, doi:10.1038/383621a0.

Tronson, N. C., C. Schrick, K. H. Huh, D. P. Srivastava, P. Penzes, A. L. Guedea, C. Gao, and J. Radulovic (2009), Segregated populations of hippocampal principal ca1 neurons mediating conditioning and extinction of contextual fear, *J Neurosci*, *29*(11), 3387–94.

Troyer, T. W., and K. D. Miller (1997), Physiological gain leads to high ISI variability in a simple model of a cortical regular spiking cell, *Neural Computation*, *9*(5), 971–983, doi:10.1162/neco.1997.9.5.971.

Uhlhaas, P., and W. Singer (2006), Neural synchrony in brain disorders: relevance for cognitive dysfunctions and pathophysiology, *Neuron*, *52*, 155–168.

van Vreeswijk, C., and H. Sompolinsky (1996), Chaos in neuronal networks with balanced excitatory and inhibitory activity, *Science*, *274*(5293), 1724–1726, doi:10.1126/science.274.5293.1724.

van Vreeswijk, C., and H. Sompolinsky (1998), Chaotic balanced state in a model of cortical circuits, *Neural Computation*, *10*(6), 1321–1371, doi:10.1162/089976698300017214.

Vanderhaeghen, P., and H. J. Cheng (2010), Guidance molecules in axon pruning and cell death, *Cold Spring Harb Perspect Biol*, *2*(6), a001,859.

Varela, F., J.-P. Lachaux, E. Rodriguez, and J. Martinerie (2001), The brainweb: Phase synchronization and large-scale integration, *Nature Reviews Neuroscience*, *2*(4), 229–239, doi:10.1038/35067550.

Vogels, T. P., and L. F. Abbott (2009), Gating multiple signals through detailed balance of excitation and inhibition in spiking networks, *Nature Neuroscience*, *12*(4), 483–491, doi:10.1038/nn.2276.

von der Malsburg, C. (1999), The what and why of binding, *Neuron*, *24*(1), 95–104, doi:10.1016/s0896-6273(00)80825-9.

Wang, H. E., C. G. Bénar, P. P. Quilichini, K. J. Friston, V. K. Jirsa, and C. Bernard (2014), A systematic framework for functional connectivity measures, *Frontiers in Neuroscience*, *8*, doi:10.3389/fnins.2014.00405.

Wang, X.-J. (2008), Decision making in recurrent neuronal circuits, *Neuron*, *60*(2), 215–234, doi:10.1016/j.neuron.2008.09.034.

Wang, X.-J. (2010), Neurophysiological and computational principles of cortical rhythms in cognition, *Physiological Reviews*, *90*(3), 1195–1268, doi:10.1152/physrev.00035.2008.

Wang, X. J., and B. G. (1996), Gamma oscillation by synaptic inhibition in a hippocampal interneuronal network model, *Journal of Neuroscience*, *16*(20), 6402–6413.

Wang, X.-J., and J. Rinzel (1992), Alternating and synchronous rhythms in reciprocally inhibitory model neurons, *Neural Computation*, *4*(1), 84–97, doi: 10.1162/neco.1992.4.1.84.

Watts, D. J. (2003), *Small Worlds: The Dynamics of Networks between Order and Randomness (Princeton Studies in Complexity)*, Princeton University Press.

Watts, D. J., and S. H. Strogatz (1998), Collective dynamics of 'small-world' networks, *Nature*, *393*(6684), 440–442, doi:10.1038/30918.

Wehr, M., and A. M. Zador (2003), Balanced inhibition underlies tuning and sharpens spike timing in auditory cortex, *Nature*, *426*(6965), 442–446, doi: 10.1038/nature02116.

Weiss, S., and P. Rappelsberger (2000), Long-range EEG synchronization during word encoding correlates with successful memory performance, *Cognitive Brain Research*, *9*(3), 299–312, doi:10.1016/s0926-6410(00)00011-2.

Wester, J. C., and C. J. McBain (2016), Interneurons differentially contribute to spontaneous network activity in the developing hippocampus dependent on their embryonic lineage, *J. Neurosci.*, *36*, 2646–2662.

White, J. G., E. Southgate, J. N. Thomson, and S. Brenner (1986), The structure of the nervous system of the nematode caenorhabditis elegans, *Philosophical Transactions of the Royal Society B: Biological Sciences*, *314*(1165), 1–340, doi: 10.1098/rstb.1986.0056.

Whitt, J. L., E. Petrus, and H.-K. Lee (2014), Experience-dependent homeostatic synaptic plasticity in neocortex, *Neuropharmacology*, *78*, 45–54, doi: 10.1016/j.neuropharm.2013.02.016.

Whittington, M. A., R. D. Traub, and J. G. R. Jefferys (1995), Synchronized oscillations in interneuron networks driven by metabotropic glutamate receptor activation, *Nature*, *373*(6515), 612–615, doi:10.1038/373612a0.

Wikenheiser, A. M., and A. D. Redish (2012), The balance of forward and backward hippocampal sequences shifts across behavioral states, *Hippocampus*, *23*(1), 22–29, doi:10.1002/hipo.22049.

Wilent, W. B., and D. Contreras (2005), Dynamics of excitation and inhibition underlying stimulus selectivity in rat somatosensory cortex, *Nature Neuroscience*, *8*(10), 1364–1370, doi:10.1038/nn1545.

Wilson, H. R., and J. D. Cowan (1972), Excitatory and inhibitory interactions in localized populations of model neurons, *Biophysical Journal*, *12*(1), 1–24, doi: 10.1016/s0006-3495(72)86068-5.

Womelsdorf, T., J.-M. Schoffelen, R. Oostenveld, W. Singer, R. Desimone, A. K. Engel, and P. Fries (2007), Modulation of neuronal interactions through neuronal synchronization, *Science*, *316*(5831), 1609–1612, doi:10.1126/science.1139597.

Wu, G. K., R. Arbuckle, B. hua Liu, H. W. Tao, and L. I. Zhang (2008), Lateral sharpening of cortical frequency tuning by approximately balanced inhibition, *Neuron*, *58*(1), 132–143, doi:10.1016/j.neuron.2008.01.035.

Xue, M., B. V. Atallah, and M. Scanziani (2014), Equalizing excitation-inhibition ratios across visual cortical neurons, *Nature*, *511*(7511), 596–600.

Yan, Z.-Q., et al. (2012), Membrane resonance and its ionic mechanisms in rat subthalamic nucleus neurons, *Neuroscience Letters*, *506*(1), 160–165, doi: 10.1016/j.neulet.2011.10.072.

Young, M. P. (1992), Objective analysis of the topological organization of the primate cortical visual system, *Nature*, *358*(6382), 152–155, doi:10.1038/358152a0.

Yu, J., and D. Ferster (2010), Membrane potential synchrony in primary visual cortex during sensory stimulation, *Neuron*, *68*(6), 1187–201.

Zaytsev, Y. V., A. Morrison, and M. Deger (2015), Reconstruction of recurrent synaptic connectivity of thousands of neurons from simulated spiking activity, *Journal of Computational Neuroscience*, *39*(1), 77–103, doi:10.1007/s10827-015-0565-5.

Zhang, L. I., A. Y. Y. Tan, C. E. Schreiner, and M. M. Merzenich (2003), Topography and synaptic shaping of direction selectivity in primary auditory cortex, *Nature*, *424*(6945), 201–205, doi:10.1038/nature01796.

Zhou, F.-W., H.-X. Chen, and S. N. Roper (2009), Balance of inhibitory and excitatory synaptic activity is altered in fast-spiking interneurons in experimental cortical dysplasia, *Journal of Neurophysiology*, *102*(4), 2514–2525, doi: 10.1152/jn.00557.2009.

Zhou, G., et al. (2019), Human olfactory-auditory integration requires phase synchrony between sensory cortices, *Nature Communications*, *10*(1), doi: 10.1038/s41467-019-09091-3.

Zhou, M., F. Liang, X. R. Xiong, L. Li, H. Li, Z. Xiao, H. W. Tao, and L. I. Zhang (2014), Scaling down of balanced excitation and inhibition by active behavioral states in auditory cortex, *Nature Neuroscience*, *17*(6), 841–850, doi: 10.1038/nn.3701.